ISSN 2355-5058
e-ISSN 2622-4852

JURNAL ECOTIPE

Electronic, Control, Telecommunication, Information, and Power Engineering

https://ecotipe.ubb.ac.id/
Volume 11, Issue 1, April 2024

Accreditation by Kemdikbudristek
Decree. No.158/E/KPT/2021 **(rank. SINTA 3)**

Electrical Engineering Department
Bangka Belitung University

Volume 11, Issue 1, April 2024
DOI : 10.33019/jurnalecotipe.v11i1

JURNAL ECOTIPE

Electronic, Control, Telecommunication, Information, and Power Engineering

Accredited by Kemdikbudristek RI
Decree No.158/E/KPT/2021 **(rank. SINTA 3)**

ISSN 2355-5068 e-ISSN 2622-4852

Publisher Address:

Electrical Engineering Department
Faculty of Science and Engineering - Bangka Belitung University
Balunijuk, Bangka Regency, Bangka Belitung Islands Province, Indonesia
Phone (0717) 4260033 ext. 2125, 2128
Website : https://journal.ubb.ac.id/index.php/ecotipe
E-mail : jurnal.ecotipe@yahoo.com / jurnalecotipe@ubb.ac.id

Preface

Jurnal Ecotipe (Electronic, Control, Telecommunication, Information, and Power Engineering) published by the Electrical Engineering Department, Bangka Belitung University currently starting Volume 7 Number 2, October 2020 to Volume 12 Number 2, October 2025 has been accredited by the Ministry of Education, Culture, Research, and Technology of the Republic of Indonesia based on Decree No. 158/E/KPT/2021 with 3rd rank (SINTA 3).

Currently, Jurnal Ecotipe volume 11 issue 1, April 2024 has been published. In this edition of the journal, the journal articles are in full English. Starting from volume 9 issue 2 October 2022, for the next editions of the articles in Jurnal Ecotipe, articles will be published using English in their writing and presentation. The articles in this edition of the journal come from academics both from within and from outside the institution.

Our highest appreciation goes to the Reviewers, Editorial Board, Authors, and all parties involved in the preparation and publication of the Jurnal Ecotipe volume 11 issue 1 April 2024. Hopefully, this journal can provide benefits and add scientific insight into the field of Electrical Engineering in particular and engineering in general. Therefore, we still hope for suggestions and constructive criticism for improvements and improvements for the progress of this journal.

Editor-in-Chief

Indexed journal on:

Volume 11, Issue 1, April 2024
DOI : 10.33019/jurnalecotipe.v11i1

JURNAL ECOTIPE
Electronic, Control, Telecommunication, Information, and Power Engineering

Accredited by Kemdikbudristek RI
Decree No.158/E/KPT/2021 **(rank. SINTA 3)**

Table of Content

JURNAL ECOTIPE
Electronic, Control, Telecommunication, Information, and Power Engineering

Volume 11, Issue 1, April 2024, pp. 1-9
ISSN 2355-5068 ; e-ISSN 2622-4852
DOI: 10.33019/jurnalecotipe.v10i1.4143

Optimization of 4G LTE Network with Automatic Cell Planning and Carrier Aggregation Methods

Sutoyo[1], Aulia Ulhamdi[2], Teddy Purnamirza[3], Mulyono[4], Ahmad Faizal[5]
[1,2,3,4,5] Universitas Islam Negeri Sultan Syarif Kasim Riau, Jl. HR. Soebrantas No. Km 15, Riau, 28923

ARTICLE INFO

Article historys:

Received : 23/06/2023
Revised : 05/03/2024
Accepted : 01/04/2024

Keywords :
Automatic Cell Planning; Bad Spots; Carrier Aggregation; Coverage Area; Network Optimization.

ABSTRACT

The implementation of 4G Long-Term Evolution (LTE) in Indonesia still faces numerous challenges, particularly in terms of coverage areas that are less than optimal, causing many areas to be classified as bad spots. One of them is Koto Baru Payobasung area, Payakumbuh. Network optimization is one method for overcoming this problem. In this study, we will use optimization techniques such as *Automatic Cell Planning* (ACP) and *Carrier Aggregation* (CA) with Received Signal Reference Power (RSRP), Signal to Interference and Noise Ratio (SINR), and Throughput parameters. Through existing simulations, the results of the initial research revealed that two of the three parameters, namely RSRP and Throughput, were classified as very bad conditions. Based on the results of optimization using the ACP technique, it was discovered that there was an increase in the RSRP value of = -103 dBm, SINR of = 2 dB, and Throughput = 15 Mbps. The RSRP value for the CA technique is -90 dBm, the SINR is 7 dB, and the throughput is 50 Mbps. Because of the value of the optimization parameter results, the CA technique is better than the ACP technique in these two optimization techniques.

Corresponding Author:

Sutoyo
Universitas Islam Negeri Sultan Syarif Kasim Riau, 28129, Pekanbaru
Email: sutoyo@uin-suska.ac.id

1. INTRODUCTION

Human needs for telecommunications networks are increasing in this era, and these needs can now be said to be their daily basic needs, especially when combined with work-from-home (WFH) policies for office workers and online schools for students/students. Both professions prove how important telecommunications networks are for human life today. 4G LTE is a telecommunications network technology that is widely used and provided by today's operators. At the time of its initial release, this 4G technology was expected to have a downlink speed of 100 Mbps and an uplink speed of 50 Mbps. However, the implementation of this 4G technology still faces numerous challenges and flaws. As a result, the estimated speed by experts is not met, and there are still many bad spot problems for this technology [1, 2]. Many factors can contribute to this bad spot problem, but with the current pandemic situation, the WFH situation for office workers and online schools for students causes an increase in traffic load. Due to the increased traffic load, eNodeB is unable to respond to user service requests. As a result, the service provided by eNodeB becomes congested, lowering network quality.

In addition, the lockdown situation, combined with students returning to their respective villages, has overburdened eNodeB in this area, causing network quality to deteriorate. Furthermore, in rural/suburban areas, the distance between eNodeBs is quite long, so users will notice a decrease in signal quality right away. Parit Putus a bad spot area in the Koto Baru area of Payakumbuh, West Sumatra. And there are 4 ENodeBs near this area, with a distance of about 1.5 – 3 Km between ENodeB and this area. According to the current simulation, the Received Signal Reference Power (RSRP) value is -110 dBm, the SINR value is -1 dB, and the Throughput value is 2400 kbps. As a result, it is possible to conclude that the network conditions in this area are deplorable. Particularly concerning the RSRP parameters and throughput. RSRP is the signal range provided by the nearest ENodeB, meaning that by looking at the RSRP value we can find out the range of the ENodeB. besides that we can also indirectly infer the condition of network performance in the region.

Meanwhile, according to data obtained from the Payakumbuh Central Statistics Agency (BPS), the population in this region is 2,037 people. And the estimated age of the population actively using smartphones is 10-50 years old, with a percentage of 65 percent. Several previous researchers have conducted studies on performance analysis and network optimization, one of which is a study titled "Analysis of 4G Network Performance in the Malang area" conducted by [3] This study examines the quality of the RAN to determine how the LTE network performs in Jln. General Basuki and Malang City Station areas (Radio Access Network). The findings revealed that the network conditions and performance in these two locations were excellent.

Furthermore, the ACP scheme has been carried out by [4] with the research title "Application of the ACP Method for Optimizing Physical Tunning of Sectoral Antennas on the 4G LTE Network in Purwokerto City". From the results of the study, it was found that the use of the ACP method was quite effective in increasing eNodeB coverage. The difference between this research and previous studies, such as research [5], is in the features of the use of carrier aggregation (CA). Which in previous studies used the Inter-band Non-Contiguous Carrier Aggregation feature, meaning that the frequencies used for the 2 carrier components have different frequencies. As for the research that the author himself did in this study using the Intra-band Continuous Carrier Aggregation feature, it means that the frequency used for the 2 carrier components has a continuous and adjacent frequency value. Meanwhile, the CA scheme that was conducted by [6] with the research title "Comparative Analysis of LTE-Advanced Carrier Aggregation Deployment Scenario 2 and 5 in Central Semarang" found that the use of the CADS5 scenario was more effective than the CADS2 scenario and the scenario without CA. From the problems identified in the existing simulation, researchers will try to overcome these problems by optimizing the network. For the optimization scheme itself, the researcher will apply 2 optimization schemes from previous studies that have been previously mentioned, among others The Automatic Cell Planning (ACP) and Carrier Aggregation (CA). The use of these two methods is intended to determine the most effective method for dealing with problems that arise.

2. RESEARCH METHOD

2.1. Research Design

This research was carried out computerized using the software network simulator Atoll.

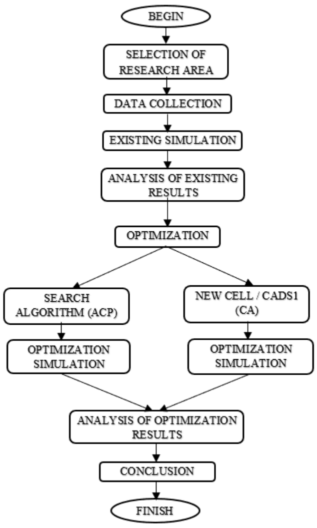

Figure 1. Research Flowchart

2.2. LTE-Advanced

LTE Release 10 allows for heterogeneous deployment of pico-cells, femtocells, relays, remote radio heads, and various macrocell settings on each low-power eNodeB. LTE Release 10 enhancements include carrier aggregation, advanced uplink (Ul) and downlink (Dl) spatial multiplexing, Multipoint coordinated DL transmission (CoMP), and heterogeneous networking with an emphasis on type 1 and type 2 relays [1, 6].

2.3. Automatic Cell Planning

Automatic Cell Planning (ACP) is a network optimization method that automates the calculation of each optimization parameter. This method will tune the parameters to improve the coverage and direction of the antenna beam. This optimization is accomplished by calculating the antenna height, azimuth, and antenna tilting. Calculations will be performed several times to obtain optimal conditions; this calculation/iteration will be performed automatically by the network simulator system [4,7].

This ACP optimization technique can be concluded as a method of increasing signal coverage and service quality without adding new ENodeBs. The range was extended as a result of changes in the antenna tilting parameters obtained through several iterations [4,8]. The image below depicts the iteration setting dialog for the ACP technique.

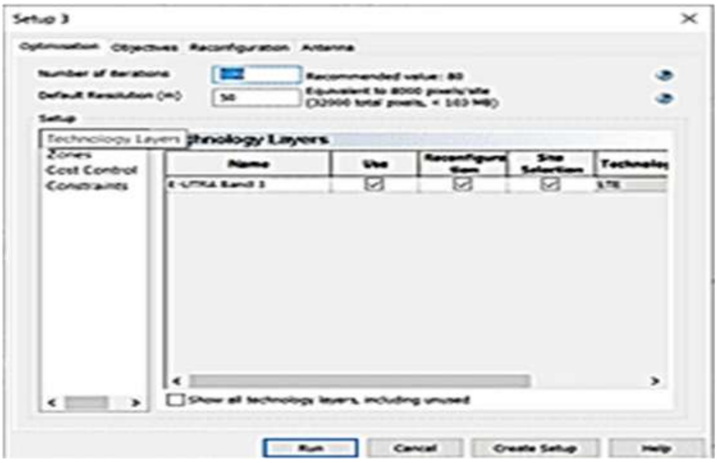

Figure 2. ACP iteration Settings

The results of the calculations will change the azimuth/direction of the antenna as well as its tilting. As a result, the mechanical tilt, electrical tilt, and antenna height values of each ENodeB will change. [9,10]. With this change, it is expected that ENodeB's performance will be more leveraged than the previous one, particularly in the given coverage area.

2.4. Carrier Aggregation (CA)

Carrier Aggregation is a method/technique of using two carrier frequencies simultaneously using the same or different frequencies to increase bandwidth. The maximum number of CC additions allowed is five (1 PCC and 4 SCC) [5]. There are several types of implemented scenarios, namely; [5, 6, 11].

1. Carrier aggregation deployment scenario 1 (CADS 1)

In the first scenario, both operator components are operating in the same frequency band, with the same antenna response and coverage area. As a result, carrier aggregation is feasible in all areas.

2. Carrier aggregation deployment scenario 2 (CADS 2)

The scopes of the scenarios for these two components differ. The coverage of the F2 component is less than that of the F1 component because it is derived from widely separated bands. They overlap each other in a small area for aggregation.

3. Carrier aggregation deployment scenario (CADS 3)

In this scenario, one carrier component's response is shifted to improve user performance at the cell's edge. Aggregation operators can also operate at the cell's edge.

The CADS1 scheme will be used by the researcher in this study. Based on the previous explanation in this scheme, the researcher introduces a new carrier signal in the same band, as well as a continuous working frequency from the previous frequency [5]. As a result, once this CA is implemented, it will be generated as shown in Figure 3.

Figure 3. CADS 1

As shown in Figure 3, the added carrier component signal has the same coverage and response as the main carrier component in the implementation of this CADS1 scheme. As a result, the possibility of aggregation that occurs between the main carrier signal and the additional carrier signal following the implementation of this optimization scheme will overlap in all eNodeB coverage areas. [12,13].

2.5. Network Design

This design is carried out by taking into account each technical parameter, such as path loss, acceptability sensitivity, and others [14,12].

1. Link Budget Calculation

Table 1. Link Budget Calculation and MAPL

MAPL & Link Budget calculation			
Morfologi			Formula
	UL	DL	
Frekuensi	1800 MHz		
Transmitter	UE	eNB	
Tx power	23	43	A
RB to distributed power	3	100	C
Subcarriers to distribute power	36	1200	D=12*C
Subcarriers power	7,44	12,2	E=A-10log(D)
Tx antenna gain	0	17	G
Tx cable loss	0	0.5	H
EIRP	7,44	28,7	J=E+G-H
Receiver	UE	eNB	
SINR	-1	-1	K
Rx niose figure	2	3	L
Receive Sensitifity	-131,3	-130,3	M=K+L-174+ 10*log(15000)
Rx antenna gain	17	0	N
Rx body loss	2	2	P
Interface margin	2	3.13	Q
Min signal reception strength	-127,3	-125,17	R=M+P+Q
Pathloss & Shadow fading margin			
Penetration loss	10	11	S
Shadow fading margin	4	5	T
MAPL	137,74	137,87	U=J+N-R-S-T

2. Propagation Model

This propagation model is a calculation that is used to determine how many path losses occur. [15, 5, 16]. The mathematical equations for this calculation are as follows:

$$PL = 46{,}3 + 33{,}9\log(fc) - 13{,}82\log(hte) - a(hre) + (44{,}9 - 6{,}55\log(hte))\log d + CM$$

Remark:
CM = 0 (suburban) and 3 (metropolitan)
F = working frequency
hte = 30 – 200 m
hre = 1 – 10 m
d = 1 – 20 Km

2.6. Parameter Engineer

1. RSRP (Reference Signal Received Power)

RSRP is a signal strength level parameter received by the user from a nearby eNodeB. [9, 4, 11].

Table 2. RSRP Mark

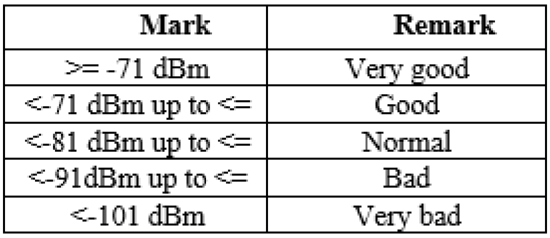

Mark	Remark
>= -71 dBm	Very good
<-71 dBm up to <=	Good
<-81 dBm up to <=	Normal
<-91dBm up to <=	Bad
<-101 dBm	Very bad

2. SINR (Signal Interference to Noice Ratio)

SINR is defined as the ratio of the main signal emitted by eNodeB to the *interference* and *noise* that occurs. [9, 17, 6].

Table 3. SINR Mark

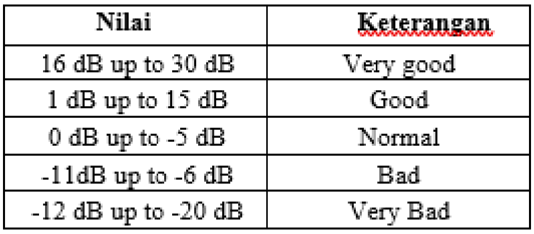

Nilai	Keterangan
16 dB up to 30 dB	Very good
1 dB up to 15 dB	Good
0 dB up to -5 dB	Normal
-11dB up to -6 dB	Bad
-12 dB up to -20 dB	Very Bad

3. Throughput

Throughput is the actual data rate of a transmitted carrier signal [18, 9, 6].

Table 4. Throughput Mark

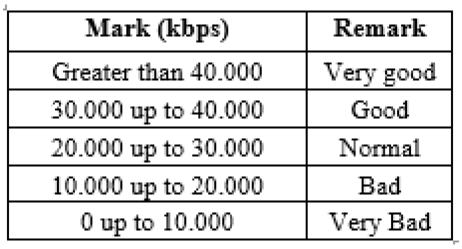

Mark (kbps)	Remark
Greater than 40.000	Very good
30.000 up to 40.000	Good
20.000 up to 30.000	Normal
10.000 up to 20.000	Bad
0 up to 10.000	Very Bad

3. RESULTS AND DISCUSSION

The ACP optimization technique is used to obtain changes in the condition of the sectoral antenna tilting at each site. Changes are obtained from this application, as shown in the Figure 4.

Figure 4. Reconfiguration improvement

Figure 4 shows the changes in several antenna parameters such as the tilt and direction of the antenna, these changes were made with the aim of finding the best combination of antenna parameters to be able to overcome the problem of bad spot areas that occur in the Ditto Ditch area. Changes in the slope of the antenna will affect the coverage area provided by an ENodeB, the smaller the slope value, the smaller the ENodeB coverage area and the greater the slope value, the farther the coverage area. However, this value change also affects the quality of the signal provided by ENodeB, the smaller the slope value and the smaller the ENodeB coverage area, the better the network quality, but the greater the slope value and the farther the coverage area provided by ENodeB, the signal quality will be better. decrease. Meanwhile, changing the value of the antenna direction will affect the direction of the emission from an ENodeB to the surrounding area.

The simulation results from these two scenarios can be seen in the Figure 5.

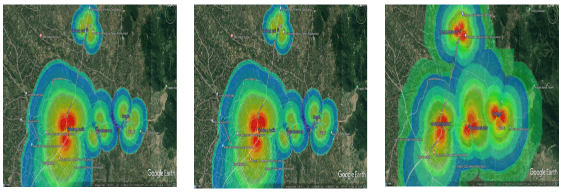

(a) Eksisting (b) ACP (c) CA

Figure 5. Optimization simulation results

Figure 5 shows the results of three optimization simulations: (a) for the existing simulation, (b) for the ACP technique, and (c) for the CA technique. The figure depicts all of the engineering parameters used in this study. We can also conclude from the image that there are differences between these two optimization technique schemes, particularly in terms of the *coverage area* they provide.

More information about the performance of each site on each parameter can be found in the figure and explanation below.

1. RSRP

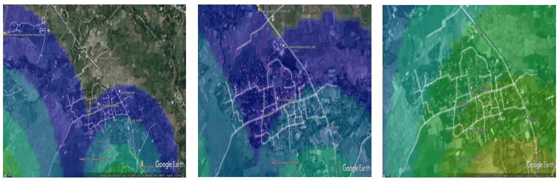

(a) Eksisting (b) ACP (c) CA

Figure 6. RSRP Parameters Result

The color of the visible zone in Figures 7(a) and 7(b) indicates differences in network quality. According to (a) the ACP optimization technique simulation results, the Koto Baru area is in the dark blue (very bad) and light blue (poor) zones. In terms of (b), the Koto Baru area is in the light blue (bad), green (normal), and yellowish green (normal) zones, according to the simulation results of CA optimization techniques. The table below provides a numerical representation of the network strength of dBm in the Koto Baru area.

Table 5. Analysis Points of Case Study Area

Cell	Distance (m)	Eksisting (dBm)	CA (dBm)	ACP (dBm)
PAYOBASUNG_1(0)	1.242	- 131,61	- 106,66	- 103,35
PAYOBASUNG_1(1)	1.242		-88,61	
KANIANGBUKIT_1(0)	2.726	- 135,3	- 112,85	- 109,54
TARAM_3(0)	2.715		- 139,04	- 122,97

Table 5 shows that the best RSRP value using the ACP optimization technique is -103.35 dBm, but this figure is still in the poor category. In terms of the CA optimization technique, the best RSRP value is -88.61 dBm, which is already in the normal range. The results of the two optimization schemes used for the RSRP parameters show that for the ACP technique, the RSRP condition is still in the bad category, whereas for the CA technique, the RSRP condition is already in the normal category.

2. SINR

(a) eksisting (b) ACP (c) CA

Figure 8. SINR Parameters Result

Figure 8(a) depicts the outcome of the optimization simulation using the ACP optimization technique, while Figure 8(b) depicts the outcome of the optimization simulation using the CA technique. At a glance, it is clear that the two optimization schemes used have different zones. The Koto Baru area is in the green zone in the ACP optimization simulation (normal). In the CA optimization simulation, Koto Baru area is in the slightly greenish-yellow zone (good). The numerical version of the SINR parameter value is shown in the Table 6.

Table 6. Analysis Point of SINR

Cell	Distance (m)	Eksisting (dB)	ACP (dB)	CA (dB)
PAYOBASUNG_1(1)	1.242			7,84
PAYOBASUNG_1(0)	1.242	-3	4,32	
KANIANGBUKIT_1(0)	2.726		1	1

The table shows that the best SINR value for using the optimization method with the ACP technique is 2.64 dB, which is generated or provided by the PAYOBASUNG coverage site cell 1. Meanwhile, the best SINR value for the application of the CA optimization technique is found to be 7 dB, which is generated from the coverage area of the PAYOBASUNG site in cell 1. (1). The PAYOBASUNG 1(1) cell is an addition to the CA optimization technique's implementation. The SINR parameter simulation results show that the SINR value is already in the good category, but the SINR value with the CA scheme is better than the ACP scheme.

3. Throughput

This network throughput is also known as the network speed that the user receives and enjoys. As a result, this parameter is critical in determining the provider's level of service satisfaction (QoS).


(a) Eksisting (b)ACP (b) CA

Figure 9. Network Throughput

Figure 9 shows the current state of the network throughput value in the research case study area (Koto Baru). According to the graph, the network throughput conditions in the Koto Baru area after the CA optimization technique were at 15,000 kbps or 15 Mbps (bad). Meanwhile, the throughput value following the CA optimization technique is greater than 50,000 kbps or 50 Mbps (very good). Figures 9 (a) and 9 (b) show that the images are nearly identical; this is because the ACP technique used in this study has not resolved the network throughput value or is still in poor condition. And, as shown in Figure 9 (c), the throughput value is already in excellent condition as a result of the CA scheme.

4. CONCLUSION

In this study, two issues were discovered in the case study area based on the existing simulation, namely very low RSRP and Throughput values. ACP (Automatic Cell Planning) and CA are the optimization schemes proposed to solve this problem (Carrier Aggregation). The use of the ACP scheme this provides several changes in the values of several antenna parameters such as the slope value and direction of the sectoral antenna direction for several sites, after the simulation is run again to see the results of using this ACP scheme, the results are still in bad condition. And the results obtained from using this ACP scheme for network performance parameter values are RSRP = -103 dBm, SINR = 2 dB, and throughput = 15 Mbps. Meanwhile, the use of the CA scheme using the intra-band feature with the CADS1 scheme provides quite a good change, and all the problems that arose at the beginning in the case study area can be resolved by using this CA scheme. After the CA scheme is implemented and simulated, the results obtained for each network performance parameter are as follows; the RSRP value is -90 dBm, the SINR is 7 dB, and the throughput is 50 Mbps. From the simulation results for the two optimization schemes carried out, it can be concluded that the use of the Carrier Aggregation (CA) optimization scheme is better than the Automatic Cell Planning (ACP) scheme in the case study area in this research.

REFERENCES

[1] M. N. Mitava Ghosh, Rapeepat Ratasuk, Bishwarup Mondal, N Itin Mangalvedhe, Dan T Thomas, “Lte-A Dvanced: Next- Generasi Wireless Broadband Teknologi,” *Law Policy*, No. 10, Pp. 10–22, 2010.

[2] A. P. Almira, A. A. Muayyadi, and A. Fahmi, “Perbandingan Kinerja Sistem Lte-Advanced Dengan Fitur Carrier Aggregation Menggunakan Metode Sfr Dan Ffr Di Wilayah Jakarta Selatan,” pp. 491–501, 2020.

[3] A. Nidya Suroyya, Hudiono, “Analisa Performansi Jaringa 4G Di Wilayah Malang,” pp. 80–85, 2019.

[4] A. Purnama, E. K. A. S. Nugraha, and M. A. Amanaf, "Penerapan Metode ACP untuk Optimasi Physical Tuning Antena Sektoral pada Jaringan 4G LTE di Kota Purwokerto," vol. 8, no. 1, pp. 138–149, 2020.

[5] S. Pramono, M. D. Ariyanto, L. Alvionita, and M. E. Sulistyo, "Analysis and optimization of 4G long term evolution (LTE) network in urban area with carrier aggregation technique on 1800 MHz and 2100 MHz frequencies," *AIP Conf. Proc.*, vol. 2217, no. April, 2020, doi: 10.1063/5.0000731.

[6] E. S. Kurniawan, A. Wahyudin, and A. R. Danisya, "Analisis Perbandingan Lte-Advanced Carrier Aggregation Deployment Scenario 2 Dan 5 Di Semarang Tengah," *Techno (Jurnal Fak. Tek. Univ. Muhammadiyah Purwokerto)*, vol. 20, no. 2, p. 77, 2019, doi: 10.30595/techno.v20i2.3960.

[7] S. Rahmatia, Di. Martin, M. Ismail, O. Nur Samijayani, D. Astharini, and R. Safitri, "Automatic Cell Planning of LTE FDD 1800 MHz Network in Klaten, Central Java," *2nd Int. Conf. Electr. Commun. Comput. Eng. ICECCE 2020*, no. June, pp. 12–13, 2020, doi: 10.1109/ICECCE49384.2020.9179483.

[8] P. K. Sudiarta, G. Sukadarmika, and Studi, "Analisis Hasil Drive Test Menggunakan Software Genex Probe Dan Genex Assistant Pada Jaringan LTE," vol. 5, no. 1, pp. 116–122, 2018.

[9] A. N. Fajar and E. Devia, "Analisa dan optimalisasi jaringan 4g lte dengan metode electrical tilt menggunakan drivetest," *Jakarta Timur, J. Jiifor*, vol. 1, no. 1, pp. 78–87, 2017.

[10] D. Rai and A. Dwivedi, "LTE theory to practice-KPI optimization (A 4G wireless technology)," *Int. J. Innov. Technol. Explor. Eng.*, vol. 8, no. 2, pp. 1–20, 2018.

[11] M. D. Asri, "Analisa Perbandingan Performasi LTE FDD-1800 Mhz Dengan LTE TDD-2300 Mhz Telkomsel Di Cluster Bsd Comparison," 2020.

[12] R. R. Yusuf, I. Uke, K. Usman, and Y. S. Rohmah, "Analisa Perencanaan Perluasan Coverage Area Lte Di Kabupaten Garut," vol. 5, no. 1, pp. 124–131, 2018.

[13] R. Hamdah, Hafidudin, and L. Meylani, "Analisis Performansi Penerapan Carrier Aggregation Dengan Perbandingan Skenario Secondary Cell Pada Perancangan Jaringan Lte-Advanced Di Dki Jakarta," *e-Proceeding Eng.*, vol. 2, no. 2, pp. 2385–2392, 2015.

[14] M. Ulfah, "Perfomansi Parameter Carrier to Noise Interference Ratio (C/N+I) terhadap Penggunaan Metode Physical Cell Identitiy (PCI) Teknologi 4G LTE 1800 MHz," *JST (Jurnal Sains Ter.*, vol. 5, no. 1, pp. 1–5, 2019, doi: 10.32487/jst.v5i1.633.

[15] V. Kusumo, P. Sudiarta, and I. Ardana, "Analisis Performansi Dan Optimalisasi Coverage Layanan Lte Telkomsel Di Denpasar Bali," *J. Ilm. SPEKTRUM*, vol. 2, no. 3, pp. 12–18, 2015.

Optimization of 4G LTE Network with Automatic Cell Planning and Carrier Aggregation Methods (Sutoyoi, et al)

JURNAL ECOTIPE
Electronic, Control, Telecommunication, Information, and Power Engineering
Volume 11, Issue 1, April 2024, pp. 10-18
ISSN 2355-5068 ; e-ISSN 2622-4852
DOI: 10.33019/jurnalecotipe.v11i1.4361

Design of Automatic Power Factor Correction for Optimization of Electric Energy Consumption

Restu Mukti Utomo[1], Adi Pandu Wirawan[2], Wisnu Candra Margono[3], Nur Rani Alham[4]
[1,2,3,4] Department of Electrical Engineering, Universitas Mulawarman, Jl. Sambaliung, Sempaja Selatan, Samarinda, Indonesia

ARTICLE INFO

Article historys:

Received : 24/08/2023
Revised : 08/09/2023
Accepted : 01/04/2024

Keywords:

Power Factor; Capacitor; Optimization; Automatic

ABSTRACT

Electrical energy is a major human need which, when viewed from its main source, namely fossil energy, will be increasingly depleted. There needs to be an effort to utilize electrical energy more optimally. The problem discussed in this research is the decrease in power factor. The State Electricity Company (PLN) has a minimum power factor standard above 0.85 which is found in the SPLN 70-1 regulation and PERMEN ESDM No. 09 of 2011. If the power factor is below the minimum limit, it will result in losses, because consumers have to pay for excess Kilo Volt Ampere Reactive Hours (kVARh). Power factor drops are caused by the use of inductive loads. With automatic power factor correction, the poor power factor due to the use of inductive loads will be resolved and optimization of the use of electrical energy can be achieved. The author tests the tool with an experimental method. From the test results conducted using 3 cumulative loads, the worst power factor value before PF repair by the system is 0.38 and after PF repair by the best power factor system reaches 0.99 and the active power value and apparent power after PF repair is almost the same (comparable) and it can be said that there is an optimization of the use of electrical energy in this study.

Corresponding Author:

Wisnu Candra Margono
Department of Electrical Engineering, Universitas Mulawarman, Jl. Sambaliung, Sempaja Selatan, Samarinda, Indonesia
Email: wisnucandra03@gmail.com

1. INTRODUCTION

Electrical energy is an energy that cannot be separated in human life in this modern era. The need for electrical energy will continue to increase over time, while the current fossil energy will decrease and even run out. Efforts are needed to be able to utilize electrical energy more efficiently [17].

Power quality is the parameter of an electric power system performing its duties reliably as seen from the constant voltage, current and frequency in accordance with its nominal value. Electrical power quality is a very important thing to consider in an effort to save electrical energy. Non-linear electrical loads become a factor that can affect power quality. Non-linear loads are loads whose output waveforms are not comparable in each half cycle so that the output voltage and current waves are not the same as the input wave or distorted. Problems that occur in electrical power quality are voltage drops, voltage swells, transients, harmonics, voltage distortion, flicker, voltage imbalance, frequency deviation, outages and power factor drops [14].

In an electric power system, Power factor (PF) can cause losses if the PF value decreases. The disadvantage for consumers if PF decreases is that the system voltage drops, the supply of electric power cannot be maximized. The State Electricity Company (PLN) has a minimum standard of power factor value that is above 0.85 which is found in SPLN 70-1 regulations and PERMEN ESDM No. 09 of 2011. If the power factor is less than 0.85, consumers will bear the payment of excess usage of Kilo Volt Ampere Reactive Hours (kVARh) with a cost per kVARh of Rp 1,444.70. Many household activities to large industries that use inductive loads in the form of electrical machinery, such as motors that can cause inductive reactive power which causes a low or poor power factor below the standards set by PLN. By improving the power factor to more than 0.85, the excess kVARh does not need to be paid and also the consumption of electric power by the load will be reduced or the consumption of electrical energy will be more optimal [5].

Inductive load is a load that has an element of wire winding in it. With the increase in inductive load, reactive power will also increase its use and can affect the quality of electrical power, especially power factor. One way to be able to reduce reactive power caused by the use of inductive loads is to compensate for reactive power. Capacitors are capacitive loads that can reduce reactive power on inductive loads. It is necessary to use capacitors so that the use of electric power to load needs is more appropriate [3].

Many jobs cannot be done effectively and efficiently if using manual methods in doing their work. Technology is needed in achieving maximum work results, including in an effort to optimize the use of electrical energy. The use of technology to be able to optimize the use of electrical energy is to make it easier for people to obtain load data when running and in this case make an automatic system on the power factor repair tool so that it no longer uses the manual method to add capacitors needed in power factor repair. Microcontroller is one of the tools that can be used as a system controller automatically.
Based on the above problems, research was conducted to be able to help solve the problem with the title "Designing Automatic Power factor Correction Based on Microcontroller for Optimizing Electric Energy Consumption". By using this microcontroller capacitor bank as a power factor repair is expected to be able to work automatically to adjust the load used in achieving the desired power factor.

2. RESEARCH METHOD

System modeling begins with a design block diagram, power factor improvement process, schematic circuit of the tool and determination of the range of capacitor values for system improvement as follows:

2.1. Design Block Diagram

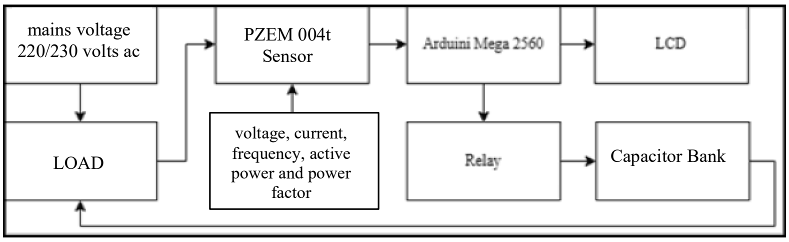

Figure 1. Design Block Diagram

The Design Block Diagram explains the location of the Input - Process - Output design. Starting from the input which is a 220/230 Volt AC voltage source and also the load that will be carried out to improve the power factor. Then in the process section is the arduino which is the core of the system that can run automatically or that regulates the work of the PZEM 004t sensor, relay and LCD, there is also a PZEM 004t sensor that detects current, voltage, active power, frequency, power factor on the load, relay as a component that can connect the capacitor bank to the system to improve the power factor. And at the output there is an LCD that displays the PZEM 004t sensor reading data before and after repairing the power factor, and there is also the load itself which experiences the impact of changes in power factor.

2.2. Power Factor Improvement Process Flowchart

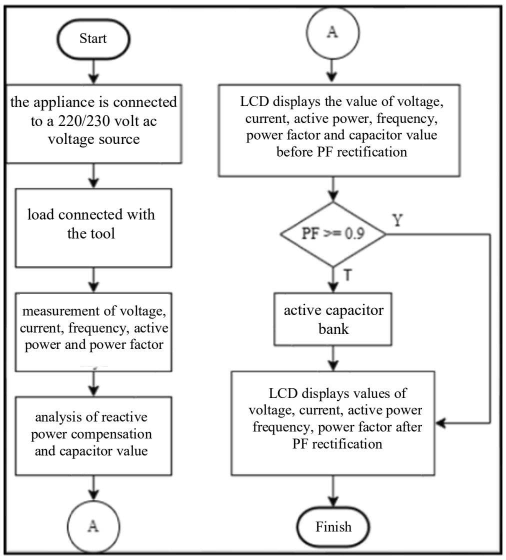

Figure 2. Power Factor Improvement Process Flowchart

The first stage is to connect the automatic power factor correction tool with an AC 220/230 Volt voltage source so that it can be activated, the second stage is to connect the load with the automatic power factor correction tool, the third stage is the system on the automatic power factor correction tool will take measurements of voltage, current, active power, frequency and power factor, the fourth stage is the system will analyze reactive power compensation and the value of capacitors used in power factor improvement, The fifth stage LCD 1 on the tool will display the value of voltage, current, active power, frequency, power factor and the value of capacitors needed for power factor correction with information before PF repair, The sixth stage if the power factor ≥ 0.9 then LCD 2 will immediately display the value of voltage, current, active power, frequency and power factor, but if the power factor < 0.9 then the capacitor bank will be activated, The seventh stage LCD 2 will display the value of voltage, current, active power, frequency and power factor that has been more than 0.9 after the capacitor bank is activated, Finish.

2.3. Schematic Circuit

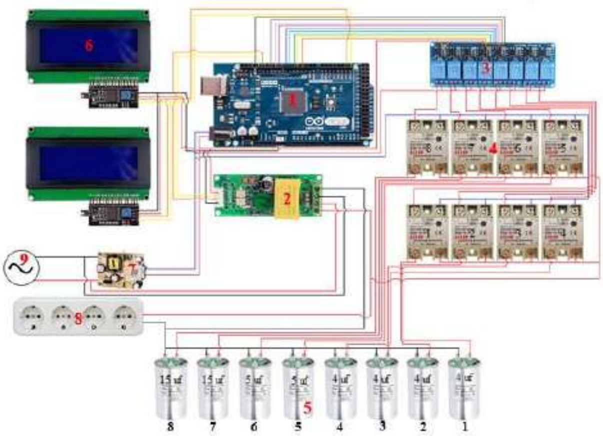

Figure 3. Schematic Circuit

Description: (1)Arduino Mega 2560, (2) PZEM 004T, (3) 8 Channel Electromagnetic Relay, (4) SSR Relay, (5) Capacitor, (6) LCD 20 x 4 with I2C, (7) Adapter, (8)Contact Stop, (9) Voltage Source 220/230 AC

Volume 11, Issue 1, April 2024, pp. 10-18
ISSN 2355-5068 ; e-ISSN 2622-4852
DOI: 10.33019/jurnalecotipe.v11i1.4361

2.4. Range Nof repair capacitor values

Table 3. Range Nof repair capacitor values

Desired Capacitor Value	System Capacitor Value
3 – 3.99 µF	4 µF
4 – 4.99 µF	5 µF
5 – 5.99 µF	8 µF
6 – 7.99 µF	8 µF
8 – 9.99 µF	10 µF
10 – 11.99 µF	12 µF
12 – 13.99 µF	14 µF
14 – 15.99 µF	15 µF
16 – 17.99 µF	18 µF
18 – 19.99 µF	20 µF
20 – 21.99 µF	22 µF
22 – 23.99 µF	23 µF
24 – 25.99 µF	25 µF
26 – 27.99 µF	27 µF
28 – 30.99 µF	30 µF
31 – 33.99 µF	33 µF
34 – 36.99 µF	36 µF
37 – 39.99 µF	39 µF
40 – 42.99 µF	42 µF
43 – 46.99 µF	46 µF
47 – 50.99 µF	51 µF
51 – 56 µF	56 µF

Table 3 above is the range of repair capacitor values that work on the system given input to the microcontroller as the brain of the system. The system capacitor value is the summation value of the parallel capacitors available in the system.

3. RESULTS AND DISCUSSION

3.1. Tool Description

Designing Automatic Power Factor Correction Based on Microcontroller to Optimize Electric Energy Consumption is a method applied to the form of a tool used to improve the power factor or power factor on inductive loads with the aim of increasing the effectiveness of the use of electrical energy. This power factor improvement tool will be active when the plug connected to the component circuit on the panel box is connected to a 220/230 Volt AC power source, the adapter contained in the tool will convert AC voltage to DC to activate electronic components that use DC voltage. The main brain of the system is arduino mega 2560 and the main data reading sensor is pzem 004t. When the load is connected to the terminal on the device, the system will read the data then LCD 1 will display the value of voltage, current, active power, frequency, power factor and the value of the capacitor needed to improve the power factor. The system will activate the relay according to the known and required capacitor value. LCD 2 will display the value of voltage, current, active power, frequency and power factor that has been improved.

Volume 11, Issue 1, April 2024, pp. 10-18
ISSN 2355-5068 ; e-ISSN 2622-4852
DOI: 10.33019/jurnalecotipe.v10i2.4361

3.2. Overall Tool Display

(a) (b) (c) (d)

Figure 4. Tool and LCD Display

Front view and (b) Inside view. On the inside view there are system components, namely (1) arduino mega 2560, (2) pzem004t sensor, (3) 8 channel electromagnetic relay, (4) solid state relay, (5) capacitor, (6) lcd 20 x 4 with I2C, (7) adapter.(c) LCD 1 reading results before power factor improvement (d) LCD 2 reading results after power factor improvement. On LCD 1 the range of power factor values that can be displayed is 0 - 0.9 while LCD 2 the range of power factor values that can be displayed is 0.9 - 1. On the LCD 1 display, the reading results before the power factor repair are displayed the value of voltage (V), current (I), active power (P), frequency (f), power factor (Pf) and the capacitor needed for repair (C). On the LCD display 2 the reading results after the power factor repair are displayed the value of voltage (V), current (I), active power (P), frequency (f), power factor (Pf). The automatic power factor correction tool can work well because LCD 1 and 2 can display the power factor value according to the range of power factor values and there is an improvement in the power factor displayed on LCD 2.

3.3. Data Collection

Table 4. System Test Results with Systematic Cumulative Load

No	Cumulative Load	Before PF Improvement					After PF Improvement					Capacitor	
		Power factor	Power (W)	Voltage (V)	Current (A)	Frequency (Hz)	*Power factor*	Power (W)	Voltage (V)	Current (A)	Frequency (Hz)	Measurable (µF)	Available (µF)
1	Electric Drill (550W) + Grinding (400W) + Ice Crusher (300W)	-	-	-	-	-	0.94	655.82	230.64	3	50	-	-
2	Grinding (400W) + Ice Crusher (300W) + Water Pump (200W)	0.86	620.7	230.6	3.13	50	0.94	630.22	230.43	2.91	50	14.5	15
3	Ice Crusher (300W) + Water Pump (200W) + Water Pump (125W)	0.66	528.7	230.7	3.45	50	0.96	538.04	231.15	2.42	50	29.32	30
4	Water Pump (200W) + Water Pump (125W) + Induction Motor (125W)	0.6	395.9	231.8	2.85	50	0.97	410.83	232.41	1.82	50	26.5	27
5	Water Pump (125W) + Induction Motor (125W) + Fan (55W)	0.67	311	230.2	2.01	50	0.98	310.39	230.33	1.37	50	16.81	18

No	Cumulative Load	Before PF Improvement					After PF Improvement					Capacitor	
		Power factor	Power (W)	Voltage (V)	Current (A)	Frequency (Hz)	*Power factor*	Power (W)	Voltage (V)	Current (A)	Frequency (Hz)	Measurable (µF)	Available (µF)
6	Induction Motor (125W) + Fan (55W) + Fan (45W)	-	-	-	-	-	0.96	242.11	228.78	1.1	50	-	-
7	Fan (55W) + Fan (45W) + TL Lamp Ballast (36W)	0.82	142	238.1	0.73	50	0.98	141.14	237.9	0.6	50	3.94	4
8	Fan (55W) + Fan (45W) + TL Light Ballast (18W)	0.84	131.9	228.3	0.69	50	0.99	130.84	227.7	0.58	50	3.59	4
9	Ice Crusher (300W) + Water Pump (125W) + TL Lamp Ballast (36)	0.69	393.8	223.1	2.56	50	0.98	397.58	223.7	1.82	50	21.33	22
10	Ice Crusher (300W) + Water Pump (125W) + TL Lamp Ballast (18)	0.6	381.5	228.6	2.79	50	0.97	391.28	228.96	1.76	50	26.41	27
Average		0.72	363.18	230.17	2.28	50	0.97	384.83	230.2	1.74	50	-	-

In systematic cumulative load testing, the range of power factor values obtained before PF improvement is carried out by the system is 0.6 - 0.86, after PF improvement the range of power factor becomes 0.94 - 0.99. The range of active power values obtained before PF improvement is performed by the system is 142.7 - 620.7 Watt, after PF improvement the range of active power values becomes 141.14 - 630.22 Watt. The voltage value range obtained before PF rectification is performed by the system is 223.1 - 238.1 Volts, after PF rectification the voltage value range becomes 223.7 - 237.9 Volts. The range of current values obtained before PF repair is performed by the system is 0.69 - 3.45 Amperes, after PF repair the range of current values becomes 0.58 - 2.91 Amperes. The range of capacitor values measured by the system for PF repair is 3.59 - 29.32 µF. From the cumulative load testing it can be systematically concluded that the greater the power required by the load, the greater the current, but the power factor also greatly affects the power and current generated.

Table 5. Percentage Increase in Power factor Efficiency Value of Cumulative Load Testing Systematically

Cumulative Load	Before improvement Power factor	After improvement Power factor	Increase in Power factor Efficiency Value
Electric Drill (550W) + Grinding (400W) + Ice Crusher (300W)	-	0.94	0
Grinding (400W) + Ice Crusher (300W) + Water Pump (200W)	0.86	0.94	8.51 %
Ice Crusher (300W) + Water Pump (200W) + Water Pump (125W)	0.66	0.96	31.25 %
Water Pump (200W) + + Water Pump (125W) + Induction Motor (125W)	0.6	0.97	38.14 %
Water Pump (125W) + Induction Motor (125W) + Fan (55W)	0.67	0.98	31.63 %
Induction Motor (125W) + Fan (55W) + Fan (45W)	-	0.96	0
Fan (55W) + Fan (45W) + TL Lamp Ballast (36W)	0.82	0.98	16.32 %
Fan (55W) + Fan (45W) + TL Light Ballast (18W)	0.84	0.99	15.15 %
Ice Crusher (300W) + Water Pump (125W) + TL Lamp Ballast (36)	0.69	0.98	29.59 %
Ice Crusher (300W) + Water Pump (125W) + TL Lamp Ballast (18)	0.6	0.97	38.14 %

JURNAL ECOTIPE
Electronic, Control, Telecommunication, Information, and Power Engineering
Volume 11, Issue 1, April 2024, pp. 10-18
ISSN 2355-5068 ; e-ISSN 2622-4852
DOI: 10.33019/jurnalecotipe.v10i2.4361

Table 6. Percentage Decrease in Electric Current Value of Systematic Cumulative Load Testing

Cumulative Load	Before repair Current (Ampere)	After repair Current (Ampere)	Electrical Current Impairment
Electric Drill (550W) + Grinding (400W) + Ice Crusher (300W)	-	3	0
Grinding (400W) + Ice Crusher (300W) + Water Pump (200W)	3.13	2.91	7.03 %
Ice Crusher (300W) + Water Pump (200W) + Water Pump (125W)	3.45	2.42	29.85 %
Water Pump (200W) + + Water Pump (125W) + Induction Motor (125W)	2.85	1.82	36.14 %
Water Pump (125W) + Induction Motor (125W) + Fan (55W)	2.01	1.37	31.84 %
Induction Motor (125W) + Fan (55W) + Fan (45W)	-	1.1	0
Fan (55W) + Fan (45W) + TL Lamp Ballast (36W)	0.73	0.6	17.8 %
Fan (55W) + Fan (45W) + TL Light Ballast (18W)	0.69	0.58	15.94 %
Ice Crusher (300W) + Water Pump (125W) + TL Lamp Ballast (36)	2.56	1.82	28.9 %
Ice Crusher (300W) + Water Pump (125W) + TL Lamp Ballast (18)	2.79	1.76	36.91 %

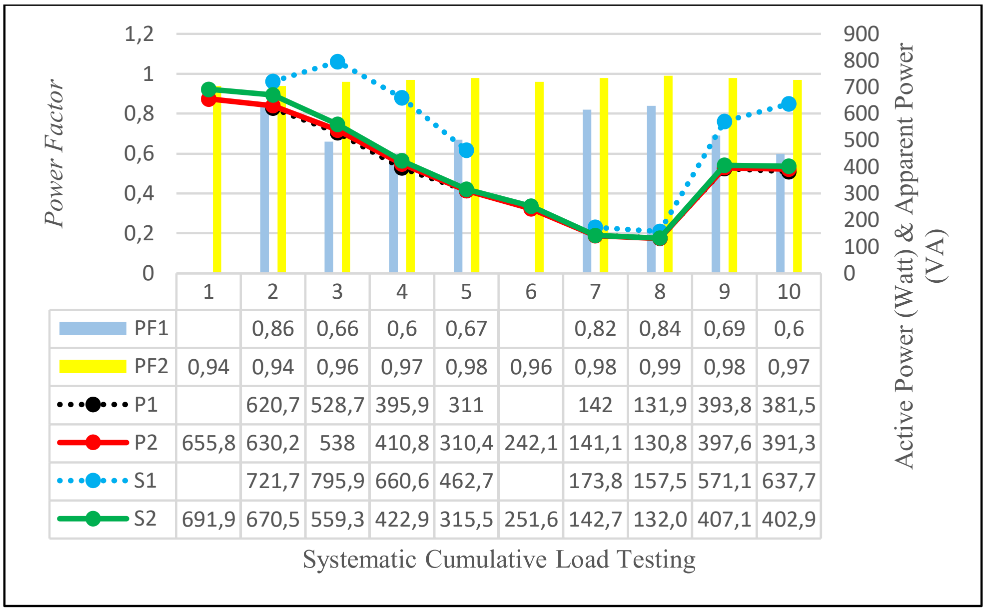

Figure 5. Comparison Chart of Power Factor, Active Power and Apparent Power Before and After Power Factor Improvement at Systematic Cumulative Load

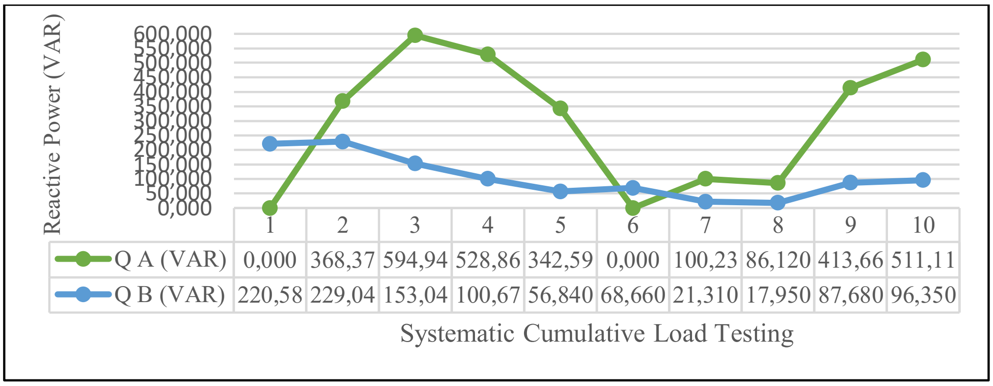

Figure 6. Comparison Chart of Reactive Power Before and After Systematic Cumulative Load Power Factor Improvement

In Figure 5, the initialization (PF1, P1 and S1) respectively is the power factor, active power and apparent power before the power factor improvement in the system and the initialization (PF2, P2, and S2) respectively is the power factor, active power and apparent power after the power factor improvement in the system. Figure 5 is a comparison graph of power factor, active power and apparent power before and after power factor improvement in the system. It can be seen that after the power factor increases, the apparent power and active power are almost the same (comparable), meaning that the apparent power which is the power generated or the source power obtained from PLN can be used by inductive loads, namely the active power optimally. In Figure 5 there are also empty values (PF1, P1 and S1) because there is no improvement in power factor because the power factor is good or above the standard that has been determined in the system, namely 0.9. In Figure 6, the initialization (Q A) is reactive power before power factor improvement and (Q B) is reactive power after power factor improvement by the system. Figure 6 is a comparison graph between reactive power before and after power factor improvement. From the graph it can be concluded that capacitor compensation has occurred in each cumulative load test. With this, the capacitor helps the power source to produce reactive power used by loads.

4. CONCLUSION

Based on the results of research that has been carried out in optimizing electrical energy consumption using a microcontroller-based automatic power factor corection tool, the following conclusions are obtained:

1. The design of an automatic power factor correction tool has been carried out which can automatically repair the power factor with commands or coding given to the brain of the system, namely the microcontroller and the use of pzem004t sensors to read the value of active power, voltage, current, frequency and power factor and LCD which is used to display the results before and after the occurrence of power factor improvement by the system, the solid state relay used has the advantage of being able to distribute capacitors on the power grid without fear of current spikes in inductive loads when the system works and also uses a panel box as a container for each component used to be safe and neat.
2. In this study, the capacitor bank has a function as a reactive power producer used for compensation in order to improve the power factor which affects the optimization of electrical energy because the capacitor is able to reduce the dependence of the electricity source (PLN) in supplying reactive power to inductive loads. Evidenced by the percentage increase in the value of power factor efficiency after improving the power factor, namely 4.04% - 59. 57% and the percentage decrease in current that occurs in inductive loads after improving the power factor, namely 1.76% - 57.38% and also the value of active power (P) becomes almost the same (comparable) with apparent power (S).
3. In this study, a microcontroller has been used as the brain of the system so that it can work automatically in performing power factor improvement. The microcontroller provides input to the pzem004t sensor to read the required value as well as instructs the relay to activate according to the needs of the capacitor used in the repair of the power factor and instructs the LCD to display the value before and after repairing the power factor.

REFERENCES

[1] Almanda, D., & Majid, N., 2019, Studi Analisa Penyebab Kerusakan Kapasitor Bank Sub Station Welding di PT. Astra Daihatsu Motor, RESISTOR (ElektRonika KEndali TelekomunikaSI Tenaga LiSTrik KOmputeR), 2(1), 7. https://doi.org/10.24853/resistor.2.1.7-14

[2] Asali, S., & Sollu, T. S., 2021, Rancang Bangun Alat Penetas Telur Ayam Otomatis Dengan Pengiriman Data Via Sms Gateway Berbasis Arduino Nano, Foristek, 11(1), 57–67. https://doi.org/10.54757/fs.v11i1.105

[3] Dani, A., & Hasanuddin, M., 2018, Perbaikan Faktor Daya Sebagai Kompensator Daya Reaktif (Studi Kasus STT Sinar Husni). Seminar Nasional Royal (SENAR), 998(September), 673–678. https://jurnal.stmikroyal.ac.id/index.php/senar/article/download/268/211

[4] Eko Kustiawan, 2018, Meningkatkan Efisiensi Peralatan dengan Menggunakan Solid State Relay (SSR) dalam Pengaturan Suhu Pack Pre-Heating Oven (PHO) , CIR Jurnal STT YUPPENTEK, 9(1), 1–6.

[5] Esye, Y., & Sigit Lesmana, 2018, ANALISA PERBAIKAN FAKTOR DAYA SISTEM KELISTRIKAN, Jurnal SPORTIF : Jurnal Penelitian Pembelajaran, 2(6), 24–29. https://www.ptonline.com/articles/how-to-get-better-mfi-results%0Amuhammadkahfi16060474066@mhs.unesa.ac.id

[6] Jaya, H., Saharuddin, Suhaeb, sutarsih, Sabara, E., Supardi, & Yunus, I., 2018, PERAWATAN DAN PERBAIKAN PERALATAN ELEKTRONIKA, Universitas Negeri Makasar

[7] Lisiani, Razikin, A., & Syaifurrahman, 2020, Identifikasi dan Analisis Jenis Beban Listrik Rumah Tangga Terhadap Faktor Daya (Cos Phi), Jurnal Untan, 1(3), 1–9.

[8] Melipurbowo, B. G., 2016, Pengukuran Daya Listrik Real Time Dengan Menggunakan Sensor Arus Acs.712, Orbith, 12(1), 17–23. https://jurnal.polines.ac.id/index.php/orbith/article/view/309

[9] Mulawarman, U., 2019, Pip Unmul, 1–23. https://lp3m.unmul.ac.id/web/download/xPX34W_KENHfz5Sb1t88_77YKN7Na355-LVVqFaWXPo

[10] Neidle, M., 1982, TEKNOLOGI INSTALASI LISTRIK, (P. A. Simorangkir (ed.); 3rd ed.), Erlangga.

[11] Priambodo, S., 2015, Monitoring Prototipe Drop Tegangan Dan Perbaikannya Pada Jaringan Tegangan Rendah Menggunakan Kapasitor Paralel, 91. http://repository.its.ac.id/51617/

[12] Ramadhan, R., Surojo, & Saputra, Z., 2021, Rancang Bangun Perbaikan Faktor Daya Menggunakan Kapasitor Bank Berbasis Mikrokontroler untuk Beban Rumah Tangga dengan Daya Maksimal 900 W, Politeknik Manufaktur Negeri Bangka Belitung

[13] Riese, P., 2015, Manual of Power Factor Correction, FRAKO Kondensatoren- Und Anlagenbau GmbH, https://www.academia.edu/27655891/Manual_of_Power_Factor_Correction_Manual_of_Power_Factor_Correction_Information_at_BULLET_Tables_at_BULLET_Formulas_Everything_on_the_subject_of_power_factor_correction_for_engineers_and_users

[14] Rizal, M. H., 2015, Kualitas Daya Listrik Industri. November, Universitas Indonesia.

[15] Sartika, Y., 2021, Sistem Pengoperasian Kapasitor Bank Dan Monitoring Menggunakan Internet Of Things (IoT) Di Gedung Elektro, http://eprints.polbeng.ac.id/2063/%0Ahttp://eprints.polbeng.ac.id/2063/4/SKRIPSI - 3204171164 - FULL TEXT.pdf

[16] Sugiarto, H., 2012, Kajian Harmonisa Arus Dan Tegangan Listrik di Gedung Administrasi Politeknik Negeri Pontianak, Teknik Elektro Politeknik Negeri Pontianak, 8(2), 80–89.

[17] Supardi, A., Budiman, A., & Khairudin, N. R., 2013, Pengaruh Kecepatan Putar Dan Beban Terhadap, Emitor: Jurnal Teknik Elektro, 16(01), 26–31.

JURNAL ECOTIPE
Electronic, Control, Telecommunication, Information, and Power Engineering
Volume 11, Issue 1, April 2024, pp. 19-28
ISSN 2355-5068 ; e-ISSN 2622-4852
DOI: 10.33019/jurnalecotipe.v11i1.4442

Feasibility Analysis of the Implementation of a Photovoltaic Water Cooling System

Riyani Prima Dewi[1], Saepul Rahmat[2]
[1,2] Departement of Electrical Engineering, Politeknik Negeri Cilacap, Jl. Dr. Soetomo, No.1, Cilacap 53212, Indonesia

ARTICLE INFO

Article historys:

Received : 14/09/2023
Revised : 31/10/2023
Accepted : 01/04/2024

Keywords:

Efficiency; Net Output Power; Photovoltaic; Temperature; Water Cooling System

ABSTRACT

This research examines the impact of implementing a cooling system on PV panels, utilizing a water flow controller, to enhance efficiency and augment power generation. The cooling system was affixed to pre-existing 200W monocrystalline photovoltaic panels. The controller effectively regulates the temperature of the photovoltaic (PV) panel at a constant value of 30°C by employing a water-cooling system. This system utilizes PVC tubes that are strategically positioned on the surface of the panel. The cooling control system is programmed to operate according to a predetermined schedule. The experimentation involved the implementation of a cooling system during PV testing, with the inclusion of non-cooled PV panels for comparison. The analysis examines the impact of temperature on the output power of a photovoltaic system, taking into account losses from the cooling system. In conclusion, an assessment was conducted on the comprehensive utilization of a water-cooling system for PV panels. The experimental findings indicate that the PV output power exhibited a 7.8% increase when the cooling system was employed as compared to the PV system without cooling. Incorporating the computation of system losses results in a net increase of 5.9% in the output power of the photovoltaic system.

Corresponding Author:

Riyani Prima Dewi
Departement of Electrical Engineering, Politeknik Negeri Cilacap, Jl. Dr. Soetomo, No.1, Cilacap 53212, Indonesia
Email: riyanipd@pnc.ac.id.

1. INTRODUCTION

Indonesia, as a nation, benefits from a consistently high level of sunlight throughout the year. Consequently, the Indonesian government has prioritised harnessing this abundant solar resource as a means to address the persistent issue of power supply shortages inside the country. The objective is to mitigate excessive reliance on fossil energy as a power source due to its insufficiency. The prevalence of solar energy as a form of electricity generation in Indonesia is more pronounced compared to other renewable energy, mostly due to the country's ample sunlight resources.

Solar photovoltaic (PV) is an emerging form of renewable energy that is employed for the purpose of generating electricity. Photovoltaic (PV) technology is capable of directly converting solar energy into electrical energy, which can then be utilized, stored, or transmitted over large distances[1]. The utilization of photovoltaic technology is expected to experience significant growth in the future due to its reliance on solar energy as a clean, dependable, scalable, and cost-effective source of electricity on a worldwide scale[2].

Solar or photovoltaic (PV) cells are composed of semiconductor materials. When the material absorbs photon energy, the electrons are liberated from the atomic bonds and become mobile, resulting in the generation of a direct current electric voltage over time. The majority of photovoltaic (PV) cells utilized in commercial applications are composed of silicon and can be classified into three main categories: monocrystalline, polycrystalline, and amorphous. Monocrystalline cells, also known as single crystals, are manufactured by utilizing silicon wafers that are derived from individual cylindrical silicon crystals. The aforementioned photovoltaic cell variant has the highest level of efficiency, approximately 15%, as measured by the proportion of solar energy successfully transformed into electrical energy[3]. However, it is worth noting that this particular type of cell is also characterized by a rather high production cost.

Temperature is an additional component that can exert an influence on the performance of photovoltaic (PV) panels, in addition to solar radiation. Photovoltaic (PV) panels commonly experience an increase in temperature as a result of solar radiation. This rise in temperature often surpasses the ideal threshold, leading to a significant decline in the performance and efficiency of both monocrystalline and polycrystalline solar cells. A rise in solar panel temperature by 1°C beyond the baseline of 25°C is associated with a decrease in the generated output power by around 0.4-0.5% [4, 5, 6, 7] . The output voltage of solar panels can be reduced by up to 0.22 V/°C due to a rise in cell temperature [8, 9, 10]. The relationship between temperature change characteristics and the electrical parameters of photovoltaic (PV) systems is illustrated in Figure 1. The rise in temperature leads to a notable decline in PV voltage, accompanied by a minor increase in PV current, resulting in a reduction in output power.

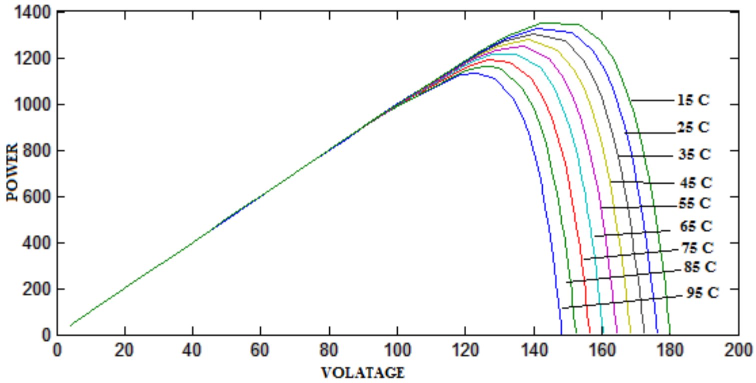

Figure 1. PV characteristics for different temperatures

Several cooling approaches have been previously suggested to enhance the effectiveness of photovoltaic (PV) systems in response to increasing temperatures. These techniques include the implementation of an active cooling system that utilizes water [11, 12, 13] and thermoelectric [14, 15]. In the context of active cooling systems, it is imperative to account for the additional electricity required in order to accurately assess the overall efficiency. Passive cooling relies on the principles of natural convection and conduction to facilitate the extraction of heat. The utilization of passive cooling with a heat sink has resulted in a notable improvement in electric efficiency[16]. Heat pipe cooling is a technique that combines phase change cooling with convection of a cooling medium[17, 18], together with the utilization of thermoelectric cooling systems that operate based on the Peltier effect[19]. Nanofluids are commonly regarded as heterogeneous blends including a cooling fluid and solid nanoparticles that are scattered throughout it. The majority of the particles employed in this context consist of metal oxides. The primary benefits associated with nanofluids are enhanced thermal conductivity, resulting in improved connection, as well as a modest increase in heat capacity[20, 21]. Through various studies and experiments, it has been demonstrated that the implementation of a cooling system can result in an increase in power output ranging from 1% to 15%.

Numerous cooling approaches have been proposed; however, only a limited number of studies have conducted comprehensive measurements and computations to determine the net power gained, as well as the relative and overall increase in efficiency. The objective of this study is to examine the impact of temperature on photovoltaic (PV) net power increases through the implementation of a suggested water cooling system. The determination of net power was conducted by incorporating cooling system losses, which were derived from the measurement of pump power during operation. Moreover, an examination and assessment of the various aspects that impact cooling system losses, which have the potential to decrease the net power output of a photovoltaic system, are conducted in order to ascertain their practicality.

2. RESEARCH METHOD

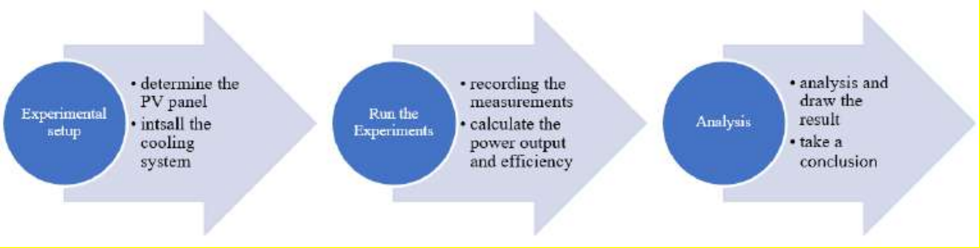

Figure 2. Research Methodology

Figure 2 shows the research methodology of this study. There are 3 main stages in this experiments, namely Experimental setup, Run the experiments, and Analysis. A detailed explanation of this research methodology will be provided in the subsequent section.

2.1. Photovoltaic (PV Panel)

The PV panel employed for experimentation in this study consisted of monocrystalline silicon solar panels with a power capacity of 100 Wp, as depicted in Figure 3. Table 1 presents the specifications of the photovoltaic (PV) panel by the standard testing conditions (STC), which include an irradiance level of 1,000W/m^2, a temperature of 25°C, and an air mass of 1.5.

Figure 3. The 100 Wp monocrystalline PV Panel

The calculation of maximum power (Pm) involves the multiplication of maximum voltage (Vm) and maximum current (Im), as expressed by the following equation (1) [22]:

$$P_m = V_m I_m \tag{1}$$

Table 1. The Specification of PV

Parameter	Value
Dimension	1020*540*30 mm
Nominal Output (Pm)	100 W
Open circuit voltage (Voc)	21.8 Vdc
Short circuit current (Isc)	6.05 A
Maximum power voltage (Vm)	17.8 Vdc
Maximum power current (Im)	5.62 A
NOCT	47±2°C

2.2. Water Cooling System

The study implements a photovoltaic (PV) cooling system that involves the application of water onto the PV panel's surface. The primary objective of this system is to regulate and sustain the temperature of the PV panel at 30^{o}C, hence mitigating the impact of increasing ambient and panel temperatures. The schematic representation of the cooling system controller, as depicted in Figure 4, is typically utilized.

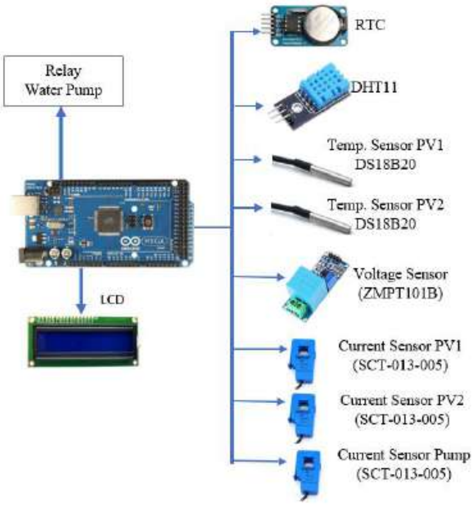

Figure 4. Schematic of cooling system controller

The primary controller utilizes an Arduino Mega 2560 microcontroller, which operates at a resolution of 10 bits. It receives input from a temperature sensor, specifically the DHT11, to measure the ambient temperature (Ta). Additionally, it utilizes an NTC (DS18B20) sensor to measure the temperature of the photovoltaic (PV) cell (Tc). Additional inputs are obtained from the voltage sensor and the current sensor. These sensors are utilized to measure the output power of the photovoltaic system (PPV). The output controller consists of relay switches that serve as regulators for the on-off operation of the pump. Additionally, it has an LCD display which presents the measured temperature values and the electricity generated by the photovoltaic system. A water pump was utilized, which was fitted a PVC tube perforated at a distance of 2 cm to circulate water on the surface of the solar panel. This PVC tube is installed at the top of the solar panel, as depicted in Figure 5. Table 2 presents the comprehensive specs of the water cooling system.

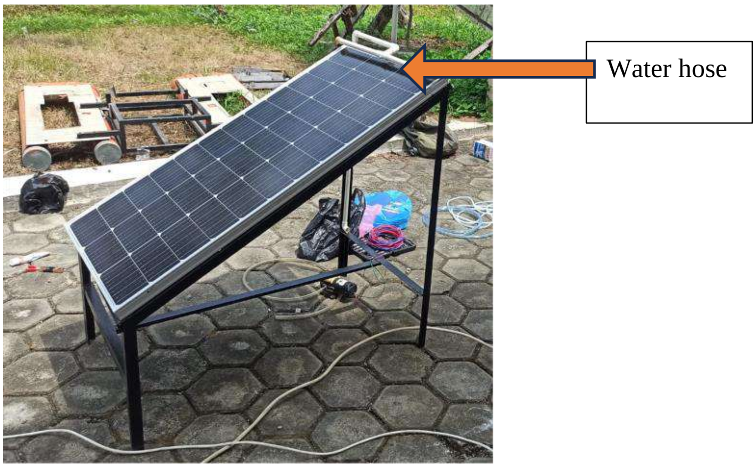

Figure 5. The position of PVC Tube on solar panel

Volume 11, Issue 1, April 2024, pp. 19-28
ISSN 2355-5068 ; e-ISSN 2622-4852
DOI: 10.33019/jurnalecotipe.v11i1.4442

Table 2. The Specification of Watercooling System

Devices	Specification
Controller	Arduino Mega 2560, 10 Bit, with 1 DHTII, 2 DS18B20
Pump	DC water pump, 12V, 8 W, 4L/m
Water hose	PVC 5/8’’

The initiation of the water cooling system program involves activating the liquid crystal display (LCD) and issuing a series of display commands. The software initiates the sensor to collect temperature data. The looping sensor operates based on predetermined settings. Specifically, if the RTC module detects the time at 09.00 am, the relay is activated. Consequently, the system triggers the pump to release water onto the surface of solar panel. In contrast, in the event that the temperature of the photovoltaic module is equal to or below 30°C, the pump will off, resulting in the cessation of water into the PV. Figure 6 displays the flowchart illustrating the designed method for controlling the cooling of photovoltaic panels.

2.3. Experimental Setup

A total of two solar panels were subjected to testing utilizing a cooling system. These panels were arranged in a linked system configuration, as depicted in Figure 7. The output of the photovoltaic (PV) system was connected to water pump, lamp, and battery. The controller records and measures the photovoltaic (PV) power, which is in the form of direct current (DC). This measurement is then examined in relation to variations in the temperature of the PV panel. The power capacity of the system is 200 watts peak (Wp). The evaluation of PV panel performance, namely PV1, involves the incorporation of non-cooled PV panels (PV2) of equivalent capacity for concurrent comparison in daylight conditions. In the photovoltaic (PV) system equipped with a cooling mechanism, there are PVC tube positioned on the top side of solar panel (see Figure 5).

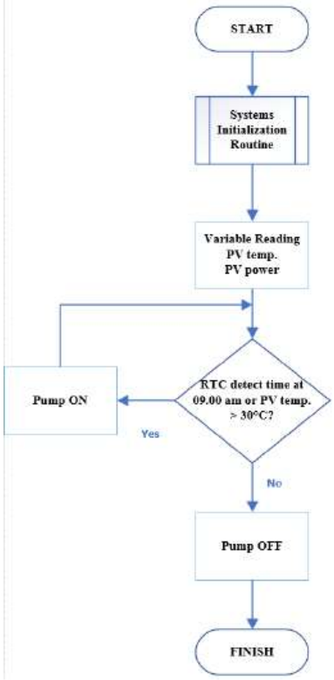

Figure 6. The flowchart of system

During the experimental procedure, the controller effectively captured and recorded all relevant parameters from the sensor in a simultaneous manner. These parameters encompassed the PV temperature and PV output power. The determination of the duration of pump operation throughout the test necessitates the acquisition of pump power values. The aggregate energy consumption of the pump is attributed to the electrical losses incurred by the cooling system. The purpose of this study was to assess the efficacy and importance of implementing a cooling system in the solar photovoltaic power system, specifically in relation to the overall net power output.

3. RESULTS AND DISCUSSION

In this section the experimental results are interpreted and presented. The measurements were recorded between 06:00am and 17:00 pm. All the readings have been recorded in a clear day on on Augustus 28th, 2023 in Cilacap. The present discourse encompasses an examination of the performance of the water cooling system, the impact of cooling PV panels on output power, and the evaluation of the system. In an early study by Bahaidarah et al. [23], the operating temperature of the water cooled CPV is reduced by 43.75% and 33.8% relative to the CPV system and the PV module, respectively, by the cooling system. And it is noted from the results that reducing the operating temperature has an obvious impact on the power output, as the power output of water cooled CPV system is almost twice as high as that of the CPV system. By comparing the present study with Bahaidarah et al., it is noted that both of the studies have the same tendency only there are variations in the values due to the circumstances of each study, such as the ambient temperature, the value of the solar radiation and the environment and the location in which the experiments are conducted. The result will be provided in the subsequent section.

Figure 7. PV panels configuration

3.1. The Performance of Water Cooling System

The simultaneous measurement outcomes, in which all readout parameters are fully depicted in curve, can be observed in Figure 8. At 6:00 AM, as the sunlight begins to rise and illuminates the panel surface, both PV panels equipped with a cooling system (PV1) and non-cooled PV panels (PV2) commence generating less power. Consequently, the temperature of both panel types starts to increase over 20ºC. At 7:30 AM, the temperature of the panel hits 30°C, while the average output power of PV1 (P-PV1) and PV2 (P-PV2) ranges between 38 - 45 W.

The temperature of the non-cooled photovoltaic (PV) panels, denoted as T-PV2, exceeded 30°C between 07:30 and 15:20. At 13:30, it reached its peak value of 58.1°C, coinciding with a power production of 66.2 W. Simultaneously, the temperature of the photovoltaic (PV) panel equipped with a cooling system, denoted as T-PV1, is around 30.12 °C, while generating an output power of 71.6 W. The findings of the calculation indicate that there is a loss of 0.411% in the output power of photovoltaic (PV) systems for every 1°C increase in temperature, specifically in the context of crystalline silicon solar cells.

Hence, it may be inferred that the functionality of the cooling system's controller was satisfactory. The pump operates in an automated manner, activating and deactivating in response to temperature fluctuations. The duration of its operation is contingent upon the readings of the temperature sensor. At present, it is evident that the influence of photovoltaic (PV) temperature on PV output power is very discernible. Specifically, the PV power generated with a cooling system (referred to as P-PV1) surpasses the power generated by noncooled PV systems (referred to as P-PV2) as a result of the lower temperature conditions.

Figure 8 displays the mean values of all parameters during one-hour intervals of daytime testing. The total power consumed during the test, denoted as P-PV1, is measured to be 501.7 Wh. Similarly, the power consumption for P-PV2 is recorded as 425.2 Wh, resulting in a difference of 36.5 Wh between the two measurements. In this particular scenario, there exists an excess power of around 7.28% as a result of the cooling phenomenon exhibited by photovoltaic (PV) panels. The surplus mentioned does not encompass the energy utilized by the cooling system, specifically the pumps. However, the losses incurred by the controller were disregarded due to their minimal power consumption, specifically less than 1 W.

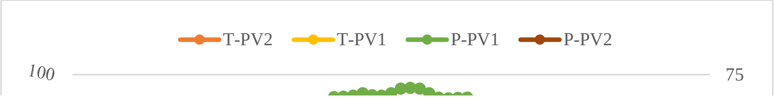

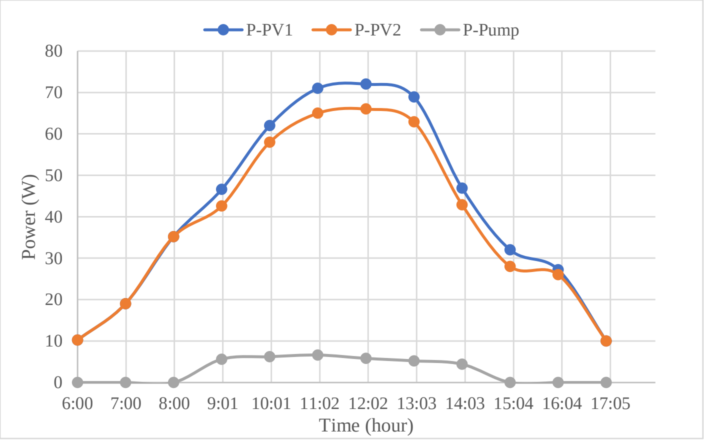

Figure 8. The hourly of measurement results

Additionally, the graph depicts the outcomes of the pump's running power measurement conducted throughout the test, shown by the gray curve. A detailed explanation of this measurement will be provided in the subsequent section.

3.2. Technical Feasibility Analysis of Water Cooling System

In addition to passive and natural cooling systems that operate without electrical power, it is important to take into account the power losses associated with the implementation of active cooling systems. The inclusion of the cooling system should be assessed in terms of its technical viability.

However, when considering the pump power, the disparity in power is observed to be 33.8 Wh, as depicted in Figure 8. The aforementioned number is derived from the computation of the disparity between the power generated by the photovoltaic (PV) system with the inclusion of the cooling mechanism (P-PV1) and the power dissipated by the cooling system. The cumulative duration of the pump's operation during the chilling procedure amounts to 3 hours, 24 minutes, and 25 seconds, leading to a total energy consumption of 40.12 watt-hours. The net output power of a photovoltaic (PV) system equipped with a cooling system, denoted as P-PV1', can be calculated as $501.7 - 40.12 = 461.58\,Wh$. When comparing the power output of cooled PV systems (P-PV2 = 425.2 Wh) to non-cooled PV systems, there is still an approximate surplus of 7.8% in power.

Figure 9 illustrates the variation in efficiency resulting from the impact of photovoltaic (PV) temperature during the experimental evaluation. Based on the photovoltaic (PV) characteristics provided in Table 1, the PV panel possesses a capacity of 100 watts peak (Wp) and occupies an area of 0.732 square meters (m2). The standard test conditions (STC) for the PV panel are defined as an irradiance of 1000 watts per square meter (W/m2) and a temperature of 25 degrees Celsius (°C). By employing equation (3), the calculated efficiency of the PV panel amounts to 13.7%.

The overall performance of the cooling system controller has demonstrated its effectiveness in regulating the temperature of photovoltaic (PV) panels at 30ºC, preventing it from exceeding this threshold. However, it is important to note that the net output power of the system is still rather low. During the cooling process, the cooling system has been in operation for 3 hours, 24 minutes, and 25 seconds, and has consumed a total of 40.12 watt-hours (Wh) of power. The manual water measurement yielded a total water usage of 248.6 liters throughout the testing process, which is comparable to 1.9 liters per minute. The current pump capacity being utilized remains below the specified rate of 4 liters per minute. The potential explanation of the low net power gains observed in the planned photovoltaic cooling system is being considered. One potential improvement involves augmenting the current pump discharge capacity by a minimum of two-fold. Rationally, augmenting the cooling water capacity will result in an accelerated cooling process. This, in turn, will lead to a reduced operational length of the pump, hence mitigating power losses in the cooling system. Consequently, the net power gain will be amplified, albeit at the expense of increased water consumption. Furthermore, it is worth noting that the suboptimal cooling process may be attributed to the positioning and spacing of the PVC tube, as observed in the field. The inadequate installation of PVC tube can result in an uneven distribution of water spray across the whole surface of the panel.

Based on the findings and assessment presented earlier, it is evident that addressing these technical challenges presents an opportunity for enhancing the net output power of the photovoltaic (PV) panels in the proposed cooling system, notwithstanding the aforementioned limitations. The consideration of these many aspects is crucial while designing the photovoltaic (PV) cooling system, with particular emphasis on active water-cooling systems, to ensure long-term viability and effectiveness.

4. CONCLUSION

This research presents a comprehensive analysis and assessment of the water-cooling methods that have been designed and subsequently tested on monocrystalline PV panels with a power output of 200 W. The cooling mechanism operates by employing water on the surface of the panel in instances at the specified time and condition. The objective of this research is to increase the power performance of the PV module by using a cooling system that are practically and economically feasible. The power performance of the monocrystalline PV module was investigated experimentally by using a cooling system. The cooling system is developed based on the water flowing on the front side of the panel to keep the temperature of the water as low as possible without consuming energy. The experimental findings during daylight hours demonstrated that the photovoltaic (PV) output power exhibited a 7.8% increase when the cooling system was implemented, in comparison to the PV system without cooling. In the context of an active cooling system, it is imperative to consider the power losses associated with the system to obtain more accurate and realistic estimations. When incorporating the computation of system losses, the net gain in PV output power amounts to 5.9%. Other variables contribute to these losses, with derating being the primary cause. One significant derating issue is the water capacity, which is lower than the pump discharge capacity. Another factor that contributes to system losses is the incorrect installation of PVC tubes, specifically in terms of spacing and orientation. This leads to uneven distribution of cooling throughout the surface of panels, resulting in suboptimal cooling processes and wastage of water. By successfully addressing these challenges, the suggested cooling system holds the potential to enhance the net output power of the photovoltaic (PV) panels, hence enhancing their feasibility.

Acknowledgments

This research was fully funded by the Academic Directorate of Vocational Education, Directorate General Vocational Education Ministry of Education, Culture, Research and Technology in 2023 with the contract number : 189/SPK/D.D4?PPK.01.APTV/VI/2023.

REFERENCES

[1] R. J. Mustafa, M. R. Gomaa, M. Al-Dhaifallah, and H. Rezk, "Environmental Impacts on the Performance of Solar Photovoltaic Systems," *Sustainability*, vol. 12, no. 2, p. 608, Jan. 2020, doi: 10.3390/su12020608.

[2] A. El Hammoumi, S. Chtita, S. Motahhir, and A. El Ghzizal, "Solar PV energy: From material to use, and the most commonly used techniques to maximize the power output of PV systems: A focus on solar trackers and floating solar panels," *Energy Reports*, vol. 8, pp. 11992–12010, Nov. 2022, doi: 10.1016/j.egyr.2022.09.054.

[3] S. Nižetić, E. Giama, and A. M. Papadopoulos, "Comprehensive analysis and general economic-environmental evaluation of cooling techniques for photovoltaic panels, Part II: Active cooling techniques," *Energy Convers Manag*, vol. 155, pp. 301–323, Jan. 2018, doi: 10.1016/j.enconman.2017.10.071.

[4] M. S. Ahmed, R. Karal, B. K. Das, and A. Das, "Experimental investigation of cooling, wind velocity, and dust deposition effects on solar PV performance in a tropical climate in Bangladesh," *Case Studies in Thermal Engineering*, vol. 50, p. 103409, Oct. 2023, doi: 10.1016/j.csite.2023.103409.

[5] A. Risdiyanto, Ant. A. Kristi, B. Susanto, N. A. Rachman, A. Junaedi, and E. W. Mukti, "Implementation of Photovoltaic Water Spray Cooling System and Its Feasibility Analysis," in *2020 International Conference on Sustainable Energy Engineering and Application (ICSEEA)*, IEEE, Nov. 2020, pp. 88–93. doi: 10.1109/ICSEEA50711.2020.9306133.

[6] M. R. Gomaa, R. J. Mustafa, and H. Rezk, "An experimental implementation and testing of a concentrated hybrid photovoltaic/thermal system with monocrystalline solar cells using linear Fresnel reflected mirrors," *Int J Energy Res*, p. er.4862, Sep. 2019, doi: 10.1002/er.4862.

[7] M. R. Gomaa, W. Hammad, M. Al-Dhaifallah, and H. Rezk, "Performance enhancement of grid-tied PV system through proposed design cooling techniques: An experimental study and comparative analysis," *Solar Energy*, vol. 211, pp. 1110–1127, Nov. 2020, doi: 10.1016/j.solener.2020.10.062.

[8] A. Bria, B. Raillani, D. Chaatouf, M. Salhi, S. Amraqui, and A. Mezrhab, "Evaluation of the efficiency of a cooling system using PCM materials for glazed and unglazed PV panels," in *2023 3rd International Conference on Innovative Research in Applied Science, Engineering and Technology (IRASET)*, IEEE, May 2023, pp. 1–7. doi: 10.1109/IRASET57153.2023.10152935.

[9] A. Hussien, A. Eltayesh, and H. M. El-Batsh, "Experimental and numerical investigation for PV cooling by forced convection," *Alexandria Engineering Journal*, vol. 64, pp. 427–440, Feb. 2023, doi: 10.1016/j.aej.2022.09.006.

[10] M. K. , N. M. , & O. A. N. YEŞİLYURT, "Techniques for enhancing and maintaining electrical efficiency of photovoltaic systems," *International Journal of New Technology and Research*, vol. 4, no. 4, Apr. 2018.

[11] M. Y. Abdalhamed, A. Almalih, M. Alshaikh, M. A. Hadi, and Y. Aldali, "Modeling and experimental investigation on the performance of a PV panel with water cooling system," in *2023 IEEE 3rd International Maghreb Meeting of the Conference on Sciences and Techniques of Automatic Control and Computer Engineering (MI-STA)*, IEEE, May 2023, pp. 836–841. doi: 10.1109/MI-STA57575.2023.10169292.

[12] S. A. Zubeer and O. M. Ali, "Experimental and numerical study of low concentration and water-cooling effect on PV module performance," *Case Studies in Thermal Engineering*, vol. 34, p. 102007, Jun. 2022, doi: 10.1016/j.csite.2022.102007.

[13] M. A. Yildirim, A. Cebula, and M. Sułowicz, "A cooling design for photovoltaic panels – Water-based PV/T system," *Energy*, vol. 256, p. 124654, Oct. 2022, doi: 10.1016/j.energy.2022.124654.

[14] P. B, V. Ravindran, M. Marimuthu, S. Ragunathan, S. K, and R. V, "Design and Implementation of PV Powered Air Cooler System Using Thermoelectric Cooler," in *2021 Innovations in Power and Advanced Computing Technologies (i-PACT)*, IEEE, Nov. 2021, pp. 1–6. doi: 10.1109/i-PACT52855.2021.9697007.

[15] V. V. Kulkarni and V. A. Kulkarni, "Performance Optimization of Photovoltaic Systems using Thermoelectric Cooling System," in *2022 International Conference on Futuristic Technologies (INCOFT)*, IEEE, Nov. 2022, pp. 1–4. doi: 10.1109/INCOFT55651.2022.10094413.

[16] S. N. Razali *et al.*, "Performance enhancement of photovoltaic modules with passive cooling multidirectional tapered fin heat sinks (MTFHS)," *Case Studies in Thermal Engineering*, vol. 50, p. 103400, Oct. 2023, doi: 10.1016/j.csite.2023.103400.

[17] A. K. Azad and S. Parvin, "Photovoltaic thermal (PV/T) performance analysis for different flow regimes: A comparative numerical study," *International Journal of Thermofluids*, vol. 18, p. 100319, May 2023, doi: 10.1016/j.ijft.2023.100319.

[18] S. D. Prasetyo, A. R. Prabowo, and Z. Arifin, "The use of a hybrid photovoltaic/thermal (PV/T) collector system as a sustainable energy-harvest instrument in urban technology," *Heliyon*, vol. 9, no. 2, p. e13390, Feb. 2023, doi: 10.1016/j.heliyon.2023.e13390.

[19] G. Fabbri and M. Greppi, "Numerical modeling of a new integrated PV-TE cooling system and support," *Results in Engineering*, vol. 11, p. 100240, Sep. 2021, doi: 10.1016/j.rineng.2021.100240.

[20] M.-W. Tian *et al.*, "Energy, exergy and economics study of a solar/thermal panel cooled by nanofluid," *Case Studies in Thermal Engineering*, vol. 28, p. 101481, Dec. 2021, doi: 10.1016/j.csite.2021.101481.

[21] A. Aydin, I. Kayri, and H. Aydin, "The Efects of TiO $_2$ Nanofluid on Efficiency and Heat Transfer Indicators of an Inner-Plate Finned Collective Cooling in a PV/T Hybrid System," in *2022 Global Energy Conference (GEC)*, IEEE, Oct. 2022, pp. 368–373. doi: 10.1109/GEC55014.2022.9986908.

[22] Aldi Cahya Muhamad *et al.*, *KONVERSI ENERGI*, 1st ed. Padang: PT Global Eksekutif Teknologi, 2023.

[23] S. Bazarchi, G. R. N. Bidhendi, I. Ghazi, And A. Kasaeian, "A Techno-Economic Feasibility Study For Reducing The Energy Consumption In A Building: A Solar Energy Case Study For Bandar Abbas," *Journal of Thermal Engineering*, vol. 6, no. 4, pp. 633–650, Jul. 2020, doi: 10.18186/thermal.766463.

JURNAL ECOTIPE
Electronic, Control, Telecommunication, Information, and Power Engineering
Volume 11, Issue 1, April 2024, pp. 29-37
ISSN 2355-5068 ; e-ISSN 2622-4852
DOI: 10.33019/jurnalecotipe.v11i1.4479

Analysis of System Operation Optimization In Steam Power Plants With the Lagrange Method

Aripriharta[1], Rafli Amirul Husain[2], Sujito[3], Mohamad Rodhi Faiz[4], Muchamad Wahyu Prasetyo[5], Arya Kusumawardana[6], Langlang Gumilar[7], Muhammad Afnan Habibi[8]
[1,2,3,4,5,6,7,8] Department of Electrical Engineering and Informatics, State University of Malang, Jl. Semarang 5 Malang, 65145, Indonesia

ARTICLE INFO

Article historys:
Received : 12/12/2023
Revised : 10/01/2024
Accepted : 01/04/2024

Keywords:
Cost Optimization; Economic Dispatch; Lagrange

ABSTRACT

A Steam Power Plant (PLTU) harnesses kinetic energy from hot steam to generate electrical power, exemplified by the Paiton Power Plant where thermal energy stems from coal combustion. Despite coal-fired power's global dominance, escalating fuel expenses underscore the significance of optimizing electric power system operations. The system comprises power generation units catering to load requirements, and cost-effective operation is achieved through Economic Dispatch. Economic Dispatch, a critical research area, utilizes diverse optimization methods. This study employs the Lagrange method, comparing its performance against the Firefly algorithm and genetic algorithm. Results reveal the Lagrange method's exceptional optimization capabilities, achieving a 7,043% cost difference, equating to $243,227,475/hour compared to actual costs. The Firefly algorithm closely follows with a 7.043% difference, amounting to $243,227,471/hour, while the genetic algorithm achieves a 7.011% difference, totaling $242,119,792/hour against actual costs. These findings underscore the efficacy of the Lagrange method in enhancing economic dispatch within steam power plants, offering valuable insights for efficient and cost-effective energy production.

Corresponding Author:

Aripriharta
Department of Electrical Engineering and Informatics, State University of Malang, Jl. Semarang 5 Malang, 65145, Indonesia
Email: aripriharta.ft@um.ac.id

1. INTRODUCTION

Steam Power Plant (PLTU) is a plant that relies on kinetic energy from hot steam to produce electrical energy [1]. At the Paiton Power Plant, thermal energy is generated from burning a certain amount of coal. The use of coal-fired power plants still dominates most of the world's electricity supply. In 2020, as many as 9,452,492 GWh or 35% of the world's electricity suppliers were supplied by coal-fired power plants [2]. Indonesia still relies heavily on steam power plants, especially those that use coal to meet thermal energy needs. Coal-fired power plants supplied 61% of Indonesia's electricity supply in 2020[2]. This is because coal is still the cheapest energy source. This condition also makes Indonesia have quite a lot of coal-fired power plants spread across various provinces.

The optimal operation of electric power systems has grown in importance in recent years due to ever-increasing fuel costs [3,4,5]. An electric power system basically consists of power generation units that aim to serve the needs of the load. The amount of load supplied and the power produced or produced by the plant must be balanced so that the plant can be operated optimally with minimal operating costs [6,7,8]. Total production costs can be minimized by a combination of power loading in existing generating units so that an optimal or more economical loading is obtained [9,10]. This optimization process is called Economic Dispatch [11]. Economic Dispatch has conducted a lot of research using various optimization methods. Some of these methods are the Lagrange method [12,13,14,15] this method solves the economic dispatch problem by minimizing costs in meeting the needs of a given load and lagrange algorithm obtained the optimal solution with a cost value of 815.1807 $/hour and PSO with a cost value of 816.8095 $/hour, the particle swarm optimization (PSO) method [16] this method used 24 bus with generation cost obtained is 16.69 $/MWh. Generation cost after rescheduling to 13.89 $ / MWh, the firefly algorithm [17] can run the optimization well, optimization results obtained using firefly with modified firefly is 41 $/hour, and many other methods [18,19,20] Genetic algorithm gets a total cost of 17607.7 $/hour and 17608.4 $/hour for Lambda Iteration method (LIM). In this study, the optimization method to be used is the Lagrange method [21]. The choice of the Lagrange method is because this method has been proven to solve economic dispatch problems [22,23,24]. The Lagrange method will compare its optimization performance with the firefly algorithm method and genetics to obtain the most optimal optimization results. The selection of these two comparison methods is because from several references collected, no one has compared these two methods with the Lagrange method.

2. RESEARCH METHOD

This study seeks the minimum value of the cost of generation using the Lagrange method. The input parameters needed to obtain the cost value are the number of units, load power, unit limit power, and generation cost coefficient.

Table 1. Generating Unit Constants

Unit	**Cash**			**Minimal (MW)**	**Maximum (MW)**
	A	**B**	**C**		
5	6757,7	113,92	0,0088	350	640
6	6403,8	121,77	0,0001	350	640

Table 2. 24 Hours Load

Time	**Load Demand**	**Time**	**Load Demand**
01.00	709,47158	13.00	1115,08796
02.00	709,99995	14.00	1230,4375
03.00	709,67175	15.00	1219,81997
04.00	702,1616	16.00	1169,1987
05.00	741,38942	17.00	1068,4471
06.00	710,95492	18.00	1072,05586
07.00	703,5477	19.00	1116,13376
08.00	715,94657	20.00	1242,767
09.00	795,16464	21.00	1252,8876
10.00	1007,7563	22.00	1244,7508
11.00	1215,3938	23.00	1244,8125
12.00	1144,1701	00.00	1246,7528

After obtaining the parameters in Table 1 and Table 2, the calculation of economic dispatch is carried out using the Lagrange method. The Lagrange method is a method that can be used to solve cost optimization problems in plants. The equation used in the Lagrange method is as in the following equation:

$$\mathcal{L} = F_T + \lambda(P_D - \textstyle\sum_{i=1}^{n} P_i) \quad (1)$$

The minimum value of the lagrange equation above occurs when the partial derivative is equal to zero:

$$\frac{\partial L}{\partial P_i} = 0 \quad (2)$$

$$\frac{\partial \mathcal{L}}{\partial P_i} = \frac{\partial F_T}{\partial P_i} + \frac{\partial \lambda P_D}{\partial P_i} - \frac{\partial \lambda \sum_{i=1}^{n} P_i}{\partial P_i} = 0 \quad (3)$$

From the above derivatives produce:

$$\frac{\partial F_T}{\partial P_i} + \lambda(0 - 1) = 0 \quad (4)$$

Then:

$$\frac{\partial F_T}{\partial P_i} = \frac{dF_i}{dP_i} = \lambda \tag{5}$$

or

$$b_i + 2c_iP_i = \lambda \tag{6}$$

From equation (6) can be obtained the value by using P_i :

$$P_i = \frac{\lambda - b_i}{2c_i} \tag{7}$$

The solution to get the value λ can be by substituting the equation P_i :

$$P_D = \sum_{i=1}^{n} \frac{\lambda - b_i}{2c_i} \tag{8}$$

So, λ it can be written as:

$$\lambda = \frac{P_D + \sum_{i=1}^{n} \frac{b_i}{2c_i}}{\sum_{i=1}^{n} \frac{1}{2c_i}} \tag{9}$$

Figure 1 shows a flowchart of research conducted to complete the study. In the picture, the first thing to do is to obtain the required data. The next thing is to solve the economic dispatch problem with the Lagrange method.

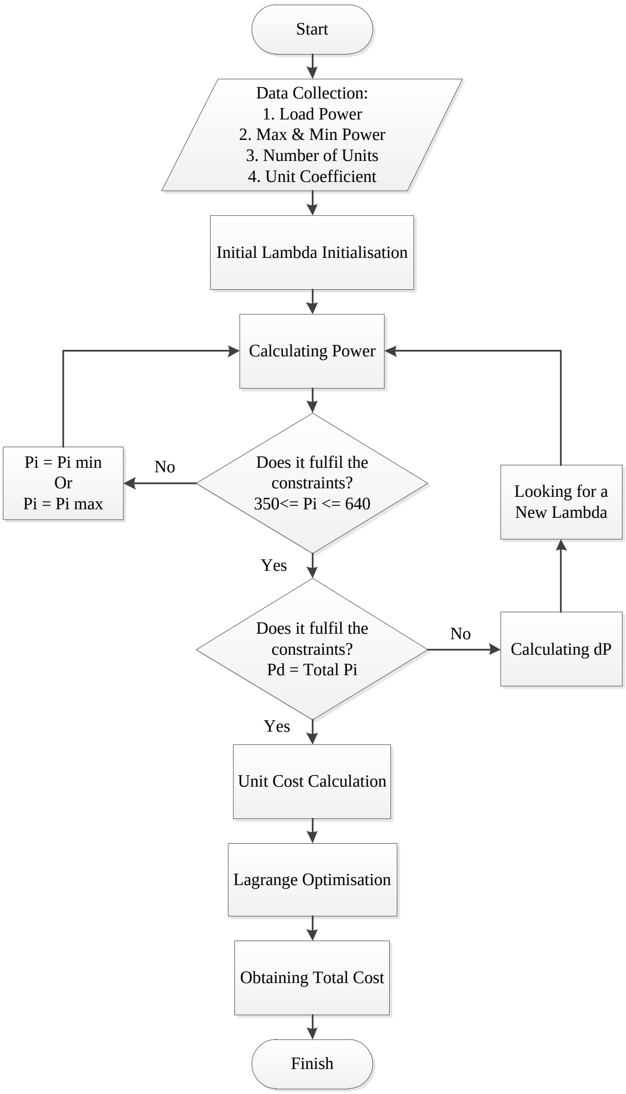

Figure 1. Research Flowchart

3. RESULTS AND DISCUSSION

3.1. Account

Manual calculations are carried out using the Lagrange method to calculate plant optimization. The plant consists of 2 generating units whose characteristics have been described with a load power at 01.00 which is 709.47158 MW.

$$P_D = 709{,}47158\ MW$$

$$\lambda = \frac{P_D + \sum_{i=1}^{n} \frac{b_i}{2c_i}}{\sum_{i=1}^{n} \frac{1}{2c_i}}$$

$$\lambda = \frac{709{,}47158 + \frac{113{,}92}{2(0{,}0088)} + \frac{121{,}77}{2(0{,}0001)}}{\frac{1}{20{,}0088)} + \frac{1}{2(0{,}0001)}}$$

$$\lambda = \frac{83852509111528059}{68780937500000}$$

$$\lambda = 1219{,}12425$$

$$P_i = \frac{\lambda - b_i}{2c_i}$$

$$P_5 = \frac{1219{,}12425 - 113{,}92}{2(0{,}0088)}$$

$$P_5 = 62795{,}6960\ \mathrm{MW}$$

$$P_6 = \frac{1219{,}12425 - 121{,}77}{2(0{,}0001)}$$

$$P_6 = 5486771{,}25\ MW$$

Because the scheduling is not perfect, the rescheduling is done as below:

$$\frac{dF_i}{dP_i} = \lambda$$

$$\lambda = b_i + 2c_iP_i$$

Then the following function is obtained:

$$\frac{dF_i}{dP_i} = b_i + 2c_iP_i$$

Enter P_5= 350 MW into the function:

$$\frac{dF_5}{dP_5} = 113{,}92 + 2 * 0{,}0088 * 350$$

$$\frac{dF_5}{dP_5} = 120{,}08$$

$$P_5 = 350\ MW$$

From the function

$$P_D = \sum_{i=1}^{n} P_i$$

Obtained values P_6 are:

$$P_6 + 350 = 709{,}47158\ MW$$

$$P_6 = 359{,}47158\ MW$$

$$\frac{\lambda - 121{,}77}{2(0{,}0001)} = 359{,}47158\ MW$$

$$\lambda = 121{,}841894316\ \$/MWh$$

$$\sum_{i=1}^{n} Pi = 709{,}47158\ \text{MW}$$

Find the cost function:

$$\boldsymbol{F_5 = 6757{,}7 + 113{,}92(359{,}47158) + 0{,}0088(359{,}47158)^2}$$

$$\boldsymbol{F_5 = 48845{,}83678\ \$/jam}$$

$$\boldsymbol{F_6 = 6403{,}8 + 121{,}77(350) + 0{,}0001(350)^2}$$

$$\boldsymbol{F_6 = 49035{,}55\ \$/jam}$$

$$\boldsymbol{F_T = \sum_{i=1}^{n} F_i}$$

$$F_T = 48845{,}83678 + 49035{,}55$$

$$F_T = 97.881{,}38678\ \$/jam$$

Find the Lagrange cost function:

$$\boldsymbol{\mathcal{L} = F_T + \lambda(P_D - \textstyle\sum_{i=1}^{n} P_i)}$$

$$\mathcal{L} = 97.881{,}38678 + 121{,}841894316\ (709{,}47158 - 709{,}47158)$$

$$\mathcal{L} = 97.881{,}38678 + 121{,}841894316\ (0)$$

$$\mathcal{L} = 97.881{,}38678\ \$/jam$$

3.2. Calculation of Optimization Method

The problem was also solved using the MATLAB application Table 3. 1. In the MATLAB application, the optimization results on the cost of generation are 97,881,387 $ / hour. The time needed to solve one problem in the MATLAB application is 0.00084 seconds. The use of the application certainly saves the time needed to solve the problem. The MATLAB application is also programmed to calculate problems using the firefly algorithm and genetic algorithm.

Table 3. Calculation At Load 709.47

Method	**Load Demand (MW)**	**PG 5 (MW)**	**PG 6 (MW)**	**Cost ($/h)**	**F6 ($/hr)**	**F5 ($/hr)**	**Elapsed Time (s)**
Real conditions	709,47	357,342	352,13	105.062,54	-	-	-
Lagrange	709,47	359,472	350	97.881,39	48.845,84	49.035,55	0,000084
Firefly	709,47	359,472	350	97.881,39	48.845,84	49.035,55	5,242561
Genetic	709,47	352,041	357,43	97.893,72	47.952,86	49.940,85	0,639069

3.3. Comparison

Comparison of the three methods used to solve the problem, there are some differences in optimization results. Performance comparison is based on the value of the cost generated and the time taken to solve the problem. This difference in optimization is caused by different ways of solving the three methods. The Lagrange method uses a Lagrange multiplier and rescheduling if it has not been achieved optimally. While the firefly method uses light intensity in the distribution of fireflies and the genetic method uses gene changes / mutations to find optimal values.

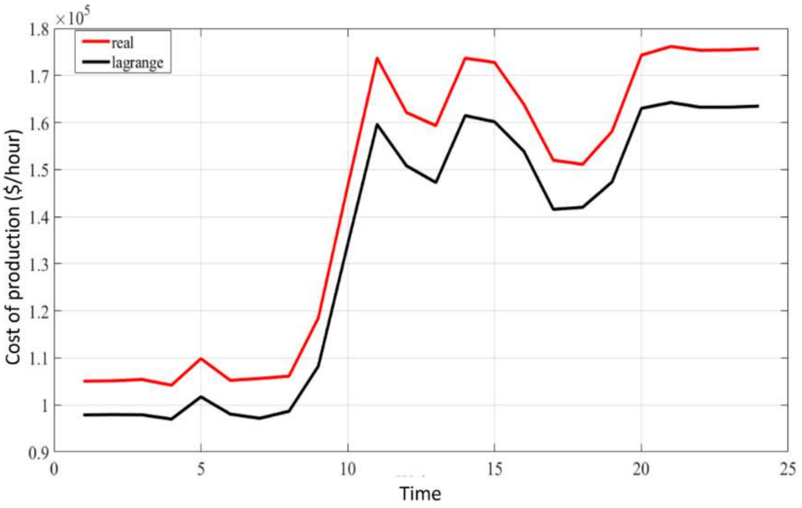

Figure 2. Real and Lagrange Cost Comparison Charts

The actual cost gets a total FT cost of 3,453,311.26$/hour while the Lagrange method gets a total FT cost of 3,210,083,790$/hour. In this way, the result of both methods is a difference of 243,227.475 $ / hour for the simulated data for 24 hours. In Figure 1 it can be seen that the cost generated by the Lagrange method is less than the actual cost of the generating unit. In Figure 2 and Figure 3 it can be seen that the cost generated by the firefly and genetic methods is less than the actual cost of the generating unit.

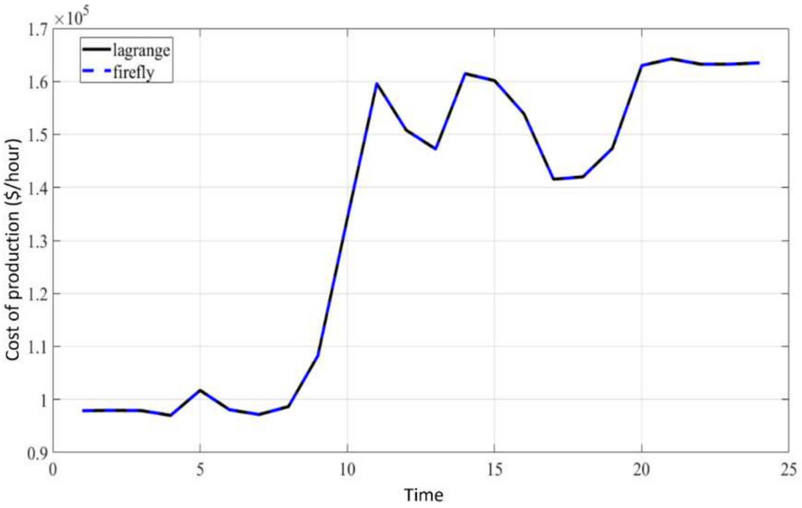

Figure 3. Firefly Cost Comparison Graph with Lagrange

Data discrepancies are also visible in the time it takes to resolve the issue. The difference in computational time performance is due to the Lagrange method which does not require random values for initial generation power. Random initial generation power means that firefly and genetic methods require more than one iteration to reach the most optimal power.

In Figure 4 It can be noted that the Lagrange method can solve problems faster than genetic algorithms and is followed by the Firefly algorithm with a longer computational time. It can be seen that the average time needed to solve the problem in the Lagrange method is 0.00011075 seconds. Meanwhile, the average time needed to solve problems in the firefly algorithm method is 2.465568083 seconds and 0.908159875 seconds in the genetic algorithm.

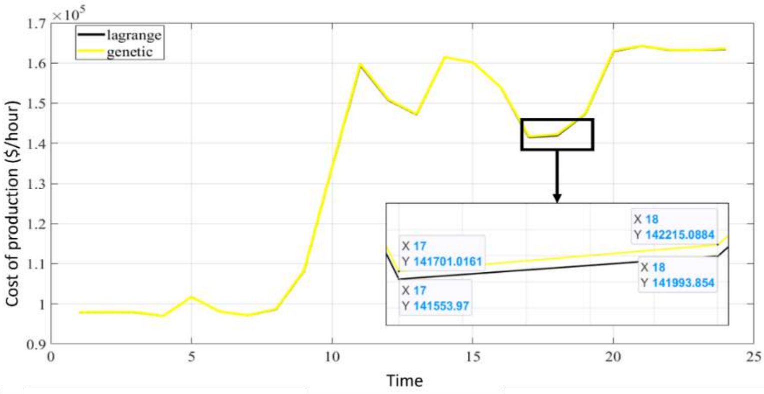

Figure 4. Genetic Cost Comparison Chart with Lagrange

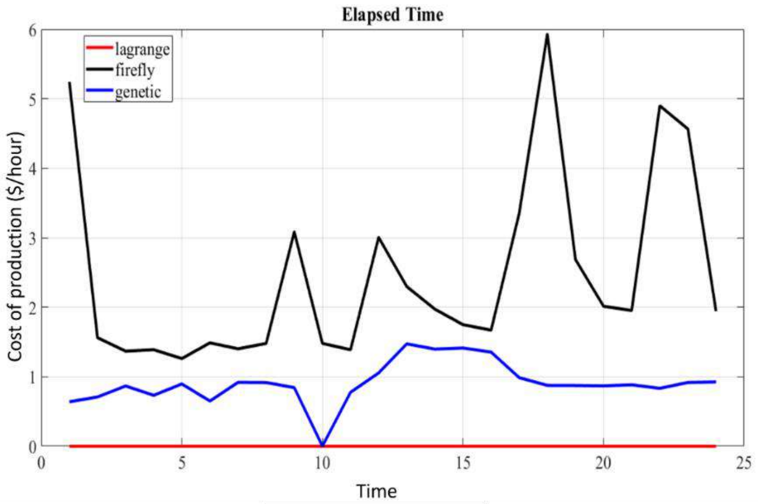

Figure 5. Graphic Elapsed Time

Data discrepancies are also visible in the time it takes to resolve the issue. In Figure 5. It can be noted that the Lagrange method can solve problems faster than genetic algorithms and is followed by the Firefly algorithm with a longer computational time. It can be seen that the average time needed to solve the problem in the Lagrange method is 0.00011075 seconds. Meanwhile, the average time needed to solve problems in the firefly algorithm method is 2.465568083 seconds and 0.908159875 seconds in the genetic algorithm.

4. CONCLUSION

Based on the results and analysis of the conducted data, it can be concluded that the economic dispatch issues in power generation units can be resolved using the Lagrange method. Calculations at 01:00 were performed both manually and through simulation using the MATLAB application, resulting in a total cost of $97,881.387 per hour. The use of this application speeds up and enhances the efficiency of calculation time.

The economic dispatch program and simulation using the Lagrange method, firefly algorithm, and genetic algorithm have been successfully executed, yielding improved optimization of generation costs. The Lagrange method optimizes generation costs with a difference of $243,227.475 per hour or 7.043% from the actual cost. Meanwhile, the firefly algorithm and genetic algorithm also provide optimization results with differences of 7.043% and 7.011% from the actual cost, respectively.

There is a noticeable difference in optimization performance among the Lagrange method, firefly algorithm, and genetic algorithm in terms of the generated generation cost values and the average required time. The Lagrange method and the firefly algorithm produce nearly identical total FT costs, with only a $0.004 per hour difference. However, the genetic algorithm yields a different total FT cost, differing by $1,107.682 per hour compared to the Lagrange method. Furthermore, the average time

Volume 11, Issue 1, April 2024, pp. 29-37
ISSN 2355-5068 ; e-ISSN 2622-4852
DOI: 10.33019/jurnalecotipe.v11i1.4479

required to solve the problem using the Lagrange method is very short, at 0.00011075 seconds, while the firefly algorithm requires 2.465568083 seconds, and the genetic algorithm requires 0.908159875 seconds.

Based on the results of the data analysis conducted, further research is needed with the utilization of environmentally friendly power generators. Analysis using different methods is also required to obtain a more optimal and efficient comparison of methods.

REFERENCES

[1] “Consumption Prediction on Steam Power Plant Using Data Mining Hybrid Particle Swarm Optimization (PSO) and Auto Regressive Integrated Moving Average (ARIMA),” 2019 Int. Work. Big Data Inf. Secur. IWBIS 2019, pp. 15–20, 2019, doi: 10.1109/IWBIS.2019.8935844.

[2] “Electricity Generation-World.”. https://www.iea.org/fuels-and-technologies/electricity

[3] “Optimization of Economic Dispatch of 150 kV Sulselrabar System using Lagrange Approach,” 2019 Int. Conf. Technol. Policies Electr. Power Energy, TPEPE 2019, 2019, doi: 10.1109/IEEECONF48524.2019.9102594.

[4] “Pengiriman Ekonomi Ideal dari Unit Tenaga Panas,” vol. 1, no. 1, 2021.

[5] “Optimal Scheduling Algorithm for Coal-Powered Power Plants-Considering Coal Delivery Constraints,” ICT-PEP 2021 - Int. Conf. Technol. Policy Energy Electr. Power Emerg. Energy Sustain. Smart Grid, Microgrid Technol. Futur. Power Syst. Proc., no. September, pp. 307–312, 2021, doi: 10.1109/ICT-PEP53949.2021.9601098.

[6] “Genetic Algorithm for Solving the Economic Load Dispatch,” Int. J. Electron. Electr. Eng., vol. 7, no. 5, pp. 523–528, 2014.

[7] “A Wind Turbine Generator Design and Optimization for DC Collector Grids,” IEEE J. Emerg. Sel. Top. Power Electron., vol. 10, no. 1, pp. 484–493, 2022, doi: 10.1109/JESTPE.2021.3066278.

[8] “Multi-Objective Optimization Design of Bearingless Permanent Magnet Synchronous Generator,” IEEE Trans. Appl. Supercond., vol. 30, no. 4, 2020, doi: 10.1109/TASC.2020.2970661.

[9] “Combinatorial optimization of pulverizers for blended-coal-fired power plant,” Proc. - Int. Conf. Comput. Distrib. Control Intell. Environ. Monit. CDCIEM 2011, pp. 413–418, 2011, doi: 10.1109/CDCIEM.2011.323.

[10] “Individual Thermal Generator and Battery Storage Bidding Strategies Based on Robust Optimization,” IEEE Access, vol. 9, pp. 66829–66838, 2021, doi: 10.1109/ACCESS.2021.3076872.

[11] “Investigation and optimization of a Co-Generation plant integrated of gasifier, gas turbine and heat pipes using minimization of Gibbs free energy, Lagrange method and response surface methodology,” Int. J. Hydrogen Energy, vol. 45, no. 38, pp. 19027–19044, 2020, doi: 10.1016/j.ijhydene.2020.04.278.

[12] “Analytical optimization of photovoltaic output with Lagrange Multiplier Method,” Optik (Stuttg)., vol. 199, no. June, p. 163379, 2019, doi: 10.1016/j.ijleo.2019.163379.

[13] “Multi-layered optimization of demand resources using lagrange dual decomposition,” IEEE Trans. Smart Grid, vol. 4, no. 4, pp. 2081–2088, 2013, doi: 10.1109/TSG.2013.2261565.

[14] “Passivity-Based Control of photovoltaic-wind hybrid system with Euler-Lagrange modeling,” IECON Proc. (Industrial Electron. Conf., pp. 1126–1131, 2012, doi: 10.1109/IECON.2012.6388614.

[15] “Comparison of the Lagrange’ s and Particle Swarm Optimisation Solutions of an Economic Emission Dispatch Problem” pp. 1–8, 2012.

[16] “Power System Optimization Model Using Economic Load Dispatch,” 2020 IEEE Reg. 10 Symp. TENSYMP 2020, no. June, pp. 469–472, 2020, doi: 10.1109/TENSYMP50017.2020.9230967.

[17] "Comparison of Firefly and Hybrid Firefly-APSO Algorithm for Power Economic Dispatch Problem," 2020 International Conference on Technology and Policy in Energy and Electric Power (ICT-PEP), Bandung, Indonesia, 2020, pp. 94-99, doi: 10.1109/ICT-PEP50916.2020.9249799.

[18] “Penggunaan Algoritma Genetika Dalam Peningkatan Kinerja Fuzzy Clustering Untuk (Application of Genetic Algorithm to Enhance the Performance of Clustering,” Berk. MIPA, vol. 17, no. 2, pp. 1–14, 2007.

[19] “A statistical energy efficiency optimization method for coal-fired power generation systems,” Proc. 2015 IEEE Innov. Smart Grid Technol. - Asia, ISGT ASIA 2015, 2016, doi: 10.1109/ISGT-Asia.2015.7387118.

[20] “Power systems optimization under uncertainty: A review of methods and applications,” Electr. Power Syst. Res., vol. 214, no. May 2022, 2023, doi: 10.1016/j.epsr.2022.108725.

[21] T. De Paula Machado Bazzo, J. F. Kölzer, R. Carlson, F. Wurtz, and L. Gerbaud, “Multiphysics Design Optimization of a Permanent Magnet Synchronous Generator,” IEEE Trans. Ind. Electron., vol. 64, no. 12, pp. 9815–9823, 2017, doi: 10.1109/TIE.2017.2726983.

[22] “An Energy Management System for Isolated Microgrids with Thermal Energy Resources,” IEEE Trans. Smart Grid, vol. 11, no. 4, pp. 2880–2891, 2020, doi: 10.1109/TSG.2020.2973321.

[23] “Comparison of ship power systems from an optimal economic operation point of view,” 2015 IEEE Electr. Sh. Technol. Symp. ESTS 2015, pp. 256–260, 2015, doi: 10.1109/ESTS.2015.7157900.

[24] “PSO Based Controlled Six-phase Grid Connected Induction Generator for Wind Energy Generation,” CES Trans. Electr. Mach. Syst., vol. 5, no. 1, pp. 41–49, 2021, doi: 10.30941/CESTEMS.2021.00006.

JURNAL ECOTIPE
Electronic, Control, Telecommunication, Information, and Power Engineering

Volume 11, Issue 1, April 2024, pp. 38-45
ISSN 2355-5068 ; e-ISSN 2622-4852
DOI: 10.33019/jurnalecotipe.v11i1.4481

Solar Tracker Prototype Based on Arduino Uno

Setiyono[1], Kunto Wibowo[2]
[1,2] Universitas Gunadarma, Jl. Margonda Raya 100 Pondokcina, Depok 16424, Indonesia

ARTICLE INFO

Article historys:

Received : 20/12/2023
Revised : 13/01/2024
Accepted : 01/04/2024

Keywords:

Solar Tracker; Solar Panel; Arduino Uno

ABSTRACT

The placement of solar panels to capture solar energy is generally installed in a certain and fixed position (static). The dynamic change in the sun's position from east to west at any time means that the solar panels absorb less energy. So, installing an automatic driving device on the solar panel to adjust its perpendicular position to the sun's rays is very necessary. This Solar Tracker tool has 4 light sensors that function to identify the intensity of sunlight as a signal entered by the Arduino Uno microcontroller. This information is then processed to become a signal to drive horizontal and vertical servo motors. The shaft of this motor is connected to the mechanical circuit of the solar panel via a gearbox to carry out movement. A comparator will compare sunlight information and a reference voltage to control the rotation of the servo motor which can determine the time needed for the motor to rotate or stop. The research results on solar panels using a tracker were that the best voltage and current values were obtained between 12.00-13.00 WIB with an average voltage value of 11.45 V and an average current value of 0.49A.

Corresponding Author:

Setiyono
Universitas Gunadarma, Jl. Margonda raya 100, Pondokcina Depok 16424, Indonesia
Email: setiyono@staff.gunadarma.ac.id

1. INTRODUCTION

The electricity and transportation industries are the main sources of global greenhouse gas emissions, contributing 40% and 24% respectively [1]. In the future, renewable energy sources will be better known as clean energy sources, which are power plants that have the potential for several consumers and the market is growing more rapidly. The fundamental reason is the emergence of global concerns about climate change [2]. One renewable energy that is environmentally friendly is the use of sunlight. Solar energy can be converted into electrical energy using semiconductor devices in the form of photovoltaics made from high-efficiency silicon silica (c-Si) crystals [3,4]. Solar energy can be obtained when the sun emits rays to the earth that move from east to west at a certain time. Nowadays, photovoltaics (PV) is growing in popularity because it is easily available. In Korea, solar panel (PV) devices are widely used to produce solar energy, and are one of the promising sources of renewable energy [5]. Photovoltaic systems can be synergistic or hybrid with other power generation networks such as wind power plants and can be built independently to increase electricity generation capacity [6] [7]. Solar panels are very appropriate for buildings in areas that are difficult to reach by conventional power plants, especially areas with certain heights, for example, mountainous areas [8]. In general, solar panels are installed by consumers in a permanent or fixed position, in a certain direction. This can cause non-continuous energy reception therefore we need a device that can follow the movement of the sun so that the position of the solar panel will always receive maximum sunlight. A solar tracker is a system designed so that solar cells are always in a perpendicular position to sunlight [9,10]. However, if the

Volume 11, Issue 1, April 2024, pp. 38-45
ISSN 2355-5068 ; e-ISSN 2622-4852
DOI: 10.33019/jurnalecotipe.v11i1.4481

energy used to move the tracker system is greater than the energy produced by the solar panel, then the position updating system is no longer needed [11].

To obtain maximum output power from solar panels without depending on temperature and solar radiation, control is required using the Maximum Power Point Tracking (MPPT) method to maintain PV performance at the MPP (Maximum Power Point) point [12]. However, some external influences such as weather and dust can reduce the maximum power received from solar cells [13]. Based on the number of rotation axes, Solar Tracker Systems can be classified into two, namely: one rotation axis and two rotation axes. Single-axis solar trackers have high-cost drive parts and control systems, this type of solar tracker is more suitable for small-sized solar cells. Single-axis solar trackers generally have a manual elevation angle setting on the second axis which is set at a fixed time period each year [14]. Until now, technology related to controlling solar panels continues to be developed, Nadia AL-Rousan developed an Artificial Intelligence application, an Adaptive Fuzzy Neural Inference System for controlling sunlight tracking on solar panels [15]. In a two-axis Solar Tracker system, the two circuits that track light consist of the same four LDR sensors placed on the east, west, south and north and two electric motors placed on each axis.

2. RESEARCH METHOD

The solar tracker prototype was made in two stages, namely designing the system block and then implementing it into an electronic control circuit. The outline of the system design is shown in Figure 1.

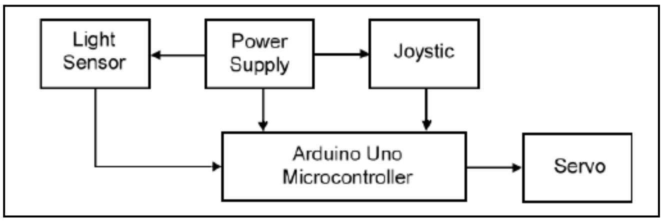

Figure 1. Diagram block

Figure 1 is an image of the block diagram process for designing a solar tracker prototype, each block has a different function. The power supply is a DC voltage supply, the DC voltage source supplies the light sensor circuit, Arduino UNO microcontroller, and joystick. There are 2 inputs, namely a light sensor which will detect the intensity of sunlight, and there is a joystick which will regulate the direction of movement of the solar panels. The process is carried out by the Arduino UNO microcontroller which processes data from the light sensor and joystick in the form of analog signals. The output of all data processed by the Arduino UNO will be sent to the servo to move the solar panel to a position with bright light intensity or according to the direction of movement of the joystick.

2.1. Research Workflow Diagram

The research workflow is shown in Figure 2. The research begins with designing the tool, assembling the tool (including repairs if necessary), and testing the tool as a whole.

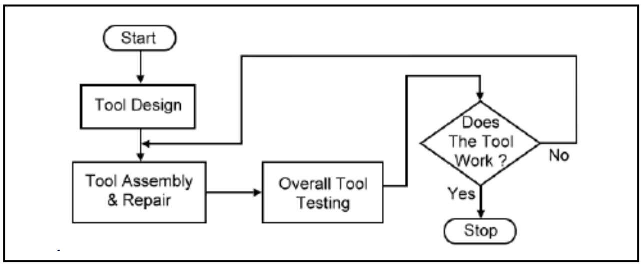

Figure 2. Research workflow diagram

In the process of making a solar tracker prototype, the first step that must be done is designing the tool. The prototype is designed in such a way that it can move the solar panels following the direction of the Sun.

2.2. Flowchart of Tool Working Principles

The flow diagram of the working principle of the tool can be seen in Figure 3. The power supply as a DC 9V voltage source supplies the light sensor circuit, joystick, and Arduino UNO microcontroller.

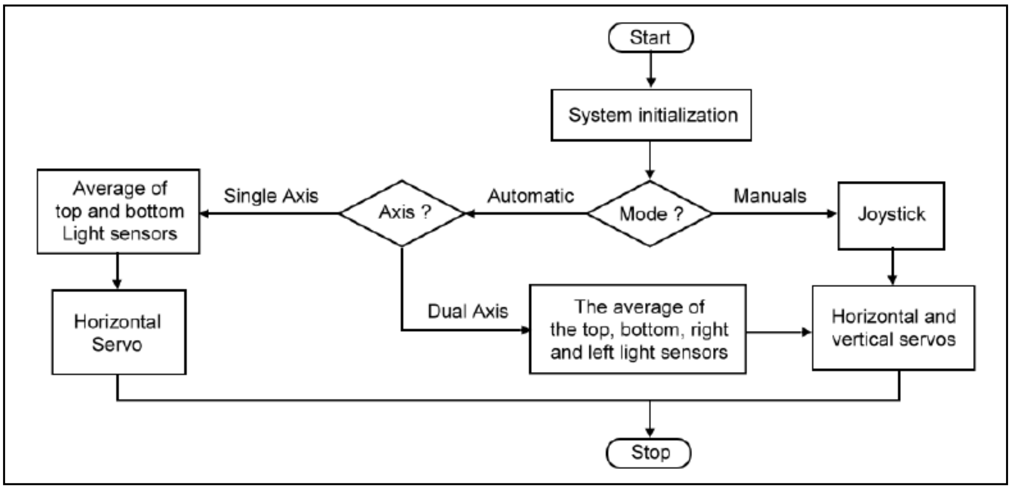

Figure 3. Flowchart of Working Principles

The way this tool works starts with initializing the Arduino UNO microcontroller, then the Arduino UNO will detect whether the mode selected is manual or automatic. When manual mode is selected, the joystick will read and move the horizontal servo and vertical servo. When in single-axis automatic mode, it will calculate the average of the up-down light sensors and activate the horizontal servo towards brighter light. When in dual axis automatic mode it will calculate the average from the up-down sensor and right-left sensor and activate the horizontal and vertical servos.

2.3. Control Circuit

The tool components used in the entire solar tracker prototype system can be seen in Figure 4.

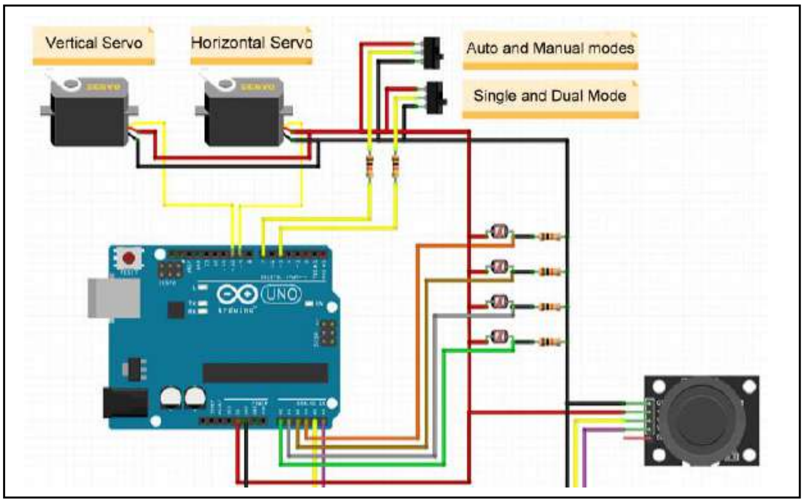

Figure 4. Schematic circuit of the tool

Figure 4 shows the entire series of components used in the solar tracker prototype using a light sensor and joystick. In the input section there is a power supply as a voltage source. In the input section there are 4 light sensors placed at the top left, top right, bottom left and bottom right. The light sensor functions to detect sunlight which will then be processed by the Arduino UNO microcontroller and will move the servo horizontally and vertically following the direction of the sun. The joystick functions as a manual driver which is processed by the Arduino UNO microcontroller and will later move the horizontal and vertical servos.

2.4. Hardware Prototype

This stage carries out the design of all components, starting from making the solar tracker prototype frame to installing the electronic components on the solar tracker prototype.

Figure 5. Solar Tracker Frame, Light Sensor Housing, Component Box

Figure 5 explains the hardware of the solar tracker system being made. The important parts of the tool are the light tracking unit, light sensor and control box.

2.5. Software

Making software is a program of all the commands that will run this tool. It could be said that this is the most important part in creating a condition program. The program code will be created as below:

```
include <Servo.h>
int switch1Pin = 5; //onoffswicth
int switch2Pin = 7; //singledualswitch
int ldrtopl = A0; //top left
int ldrtopr = A1; //top right
int ldrbotl = A2; //bottom left
int ldrbotr = A3; //bottom right
int left_joystick_x = A4; //Horizontal
int left_joystick_y = A5; //Vertical
void setup() {
servohori.attach(9); //Servo X
servohori.write(90);
servoverti.attach(10); //Servo Y
servoverti.write(90);
delay(500);
pinMode (5, INPUT_PULLUP); //onoffswitch
pinMode (7, INPUT_PULLUP); //singledualswitch
pinMode (9, OUTPUT);
pinMode (10, OUTPUT);
Serial.begin(9600);
}
```

The void setup defines the input and output, where the horizontal servo or servo X is connected to digital pin 9 and the vertical servo or servo Y is connected to digital pin 10. For manual and automatic selectors it is connected to digital pin 5 and for single axis or dual axis selectors it is connected to digital pin 7. The light sensor is connected to analog pins A0 to A3 and the vertical horizontal joystick is connected to analog pins A4 to A5.

2.6. Single Axis Automatic Software Design

Software design for a single-axis automatic program is a program for a light sensor that functions to control the X-axis servo motor. By comparing the top and bottom light sensors.

Single Axis Automatic Software Design

```
int avgtop = (topl + topr) / 2; //above average
int avgbot = (botl + botr) / 2; //lower average
if (avgtop < avgbot){
servohori.write(servoh -1);
if (servoh > servohLimitHigh){
servoh = servohLimitHigh;
}
delay(100);
}
else if (avgbot < avgtop){
servohori.write(servoh +1);
if (servoh < servohLimitLow){
servoh = servohLimitLow;
}
delay(100);
}
else{
servohori.write(servoh);
}
delay(50);
```

3. RESULTS AND DISCUSSION

Testing on the solar tracker prototype was carried out for three days from 7.00 – 17.00 WIB, with data taken every 1 hour. Solar panel voltage and current testing is carried out without load to obtain Voltage (V) and Current (I) values, weather conditions are categorized as clear and cloudy. The position of the solar panel is observed using the Arduino application which will display the position of the servo motor in degrees. Solar panel voltage and current measurements are measured using a multimeter.

Table 1. First Day Tool Data Collection

No	Time	Voltage (V)	Current (I)	Weather Conditions	Servo X Position	Servo Y Position
1.	7.00	10.50	0.36	Cloudy	140°	180°
2.	8.00	11.00	0.40	Cloudy	130°	180°
3.	9.00	11.30	0.44	Bright sky	120°	180°
4.	10.00	11.36	0.48	Bright sky	110°	180°
5.	11.00	11.60	0.50	Bright sky	100°	180°
6.	12.00	12.18	0.66	Bright sky	90°	180°
7.	13.00	12.05	0.65	Bright sky	80°	180°
8.	14.00	12.00	0.62	Bright sky	70°	180°
9.	15.00	11.70	0.53	Bright sky	60°	180°
10.	16.00	11.55	0.50	Bright sky	50°	180°
11.	17.00	11.12	0.38	Cloudy	40°	180°

Table 1 shows the values of voltage, current, servo X position and sevo Y position obtained from 140° – 40°. The highest voltage and current values were obtained at 12.18 V and 0.66 A at 12.00, and the lowest voltage and current values were 10.50 V and 0.36 A, so the difference between the voltage at the highest and lowest values was 1.68 V and the difference between the current at the highest and lowest values was 0.3A. The highest voltage and current values are at 12.00 WIB, with the solar panel positioned at 90°. It can be seen that the time range that gets the highest voltage and current values is around 11.00 – 13.00 WIB.

Table 2. Second Day Tool Data Collection

No	Time	Voltage (V)	Current (I)	Weather Conditions	Servo X Position	Servo Y Position
1.	7.00	11.10	0.40	Bright sky	140°	160°
2.	8.00	11.20	0.42	Bright sky	129°	160°
3.	9.00	11.30	0.46	Bright sky	123°	160°
4.	10.00	11.35	0.49	Bright sky	120°	160°
5.	11.00	11.60	0.53	Bright sky	100°	160°
6.	12.00	12.35	0.62	Bright sky	95°	160°
7.	13.00	12.10	0.58	Bright sky	86°	160°
8.	14.00	11.50	0.50	Bright sky	82°	160°
9.	15.00	11.00	0.43	Cloudy	75°	160°
10.	16.00	10.48	0.40	Cloudy	64°	160°
11.	17.00	10.33	0.35	Cloudy	55°	160°

Table 2 shows the values of voltage, current, servo X position and sevo Y position obtained from 140° – 55°. So that the highest values of voltage and current are 12.35 V and 0.60 A at 12.00, and the lowest values of voltage and current are 10.33 V and 0.31 A, so the difference in voltage at the highest and lowest values is 2.02 V and the difference in current at the highest and lowest values is 2.02 V. 0.27A. The highest voltage and current values are at 12.00 WIB, with the solar panel positioned at 95°. It can be seen that the time range that gets the highest voltage and current values is around 11.00 – 13.00 WIB.

Table 3. Third Day Tool Data Collection

No	Time	Voltage (V)	Current (I)	Weather Conditions	Servo X Position	Servo Y Position
1.	7.00	10.85	0.35	Cloudy	140°	160°
2.	8.00	11.21	0.42	Cloudy	130°	160°
3.	9.00	11.29	0.44	Bright sky	120°	160°
4.	10.00	11.36	0.47	Bright sky	110°	160°
5.	11.00	11.64	0.56	Bright sky	100°	160°
6.	12.00	12.16	0.63	Bright sky	90°	160°
7.	13.00	12.40	0.73	Bright sky	80°	160°
8.	14.00	12.07	0.60	Bright sky	70°	160°
9.	15.00	11.86	0.58	Cloudy	60°	160°
10.	16.00	11.24	0.46	Cloudy	50°	160°
11.	17.00	11.20	0.44	Cloudy	40°	160°

Table 3 shows the values of voltage, current, servo X position and sevo Y position obtained from 140°-40°. So that the highest voltage and current values are 12.40 V and 0.73 A at 13.00, and the lowest voltage and current values are 10.85 V and 0.35 A, so the difference between the voltage at the highest and lowest values is 1.85 V and the difference between the current at the highest and lowest values is 1.85 V. 0.38 A. The highest value of voltage and current at 13.00 WIB, achieved with the solar panel position at 80°. It can be seen that the time range that gets the highest voltage and current values is around 12.00-14.00 WIB.

3.1. Servo Axis Testing

Servo axis testing is carried out using an Arduino idea which will show the magnitude of the servo movement due to changes in the direction of the light sensor.

Table 4. Servo Axis Testing of Light Sensors

No	Light Sensor				Servo	
	Top Left	Top right	Bottom left	Bottom right	Horizontal	Vertical
1	<500	<500	>500	>500	180º	0º
2	>500	>500	<500	<500	0º	180º
3	<500	>500	<500	>500	180º	0º
4	>500	<500	>500	<500	0º	180º

Table 4 shows the angles of the horizontal and vertical servo motors according to the light sensor values. When the top left light sensor is <500, the top right light sensor is <500, the bottom left light sensor is >500, the bottom right light sensor is >500 then the horizontal servo is at an angle of 180º and the vertical servo is at an angle of 0º. When the top left light sensor is >500, the top right light sensor is >500, the bottom left light sensor is <500, the bottom right light sensor is <500 then the horizontal servo is at an angle of 0º and the vertical servo is at an angle of 180º. When the top left light sensor is <500, the top right light sensor is >500, the bottom left light sensor is <500, the bottom right light sensor is >500 then the horizontal servo is at an angle of 180º and the vertical servo is at an angle of 0º. When the top left light sensor is >500, the top right light sensor is <500, the bottom left light sensor is >500, the bottom right light sensor is <500 then the horizontal servo is at an angle of 0º and the vertical servo is at an angle of 180º.

4. CONCLUSION

The prototype of the sun ray tracker that was built can work well, the sun ray tracking process is carried out by four LDR sensors which will detect the movement of the sun rays and convert them into input for the microcontroller to give commands to the motor to move right to left or up and down. There are two working modes of this tool, namely automatic mode and manual mode. Automatic mode will work based on the top and bottom light sensors for horizontal movement using a single axis and the top, bottom, right and left light sensors for vertical movement using a dual axis. The average measurement results for 3 days show the highest voltage and current values at 12.00 with voltage levels of 12.15 V and 0.64 A.

Acknowledgments

The author would like to express his deepest gratitude to Gunadarma University for its moral and financial support so that this research could be completed successfully.

REFERENCES

[1] D. Zhao *et al.*, “Dispatching Fuel-cell Hybrid Electric Vehicles Toward Transportation and Energy,” vol. 9, no. 4, pp. 1540–1550, 2023, doi: 10.17775/CSEEJPES.2020.03640.

[2] Z. Ullah and M. Baseer, “Operational Planning and Design of Market-Based Virtual Power Plant with High Penetration of Renewable Energy Sources,” vol. 11, no. 3, pp. 620–629, 2022.

[3] M. Dada and P. Popoola, “Recent advances in solar photovoltaic materials and systems for energy storage applications : a review,” *Beni-Suef Univ. J. Basic Appl. Sci.*, 2023, doi: 10.1186/s43088-023-00405-5.

[4] P. Siagian and R. Manurung, “Pengembangan Panel Surya 120 Wp Dengan Solar Tracker Double Axis Sebagai Bahan Pembelajaran Mahasiswa di Program Studi Teknik Mesin UHN,” vol. 3, no. 2, pp. 115–128, 2022.

[5] J. Kim, D. Kim, W. Yoo, J. Lee, and Y. B. Kim, “Daily prediction of solar power generation based on weather forecast information in Korea,” doi: 10.1049/iet-rpg.2016.0698.

[6] P. S. Sikder and N. Pal, “Journal of King Saud University – Engineering Sciences Modeling of an intelligent battery controller for standalone solar-wind hybrid distributed generation system,” *J. King Saud Univ. - Eng. Sci.*, vol. 32, no. 6, pp. 368–377, 2020, doi: 10.1016/j.jksues.2019.02.002.

[7] D. Menaga and V. Sankaranarayanan, “Journal of King Saud University – Engineering Sciences Performance comparison for grid connected photovoltaic system using sliding mode control,” *J. King Saud Univ. - Eng. Sci.*, vol. 33, no. 4, pp. 276–283, 2021, doi: 10.1016/j.jksues.2020.04.012.

[8] J. Karpi, “Comparison of solar power measurements in alpine areas using a mobile dual-axis tracking system,” vol. 2, pp. 1–14, 2019.

[9] A. M. Putra and U. N. Padang, “Sistem Kendali Solar Tracker Satu Sumbu berbasis Arduino dengan sensor LDR,” vol. 06, no. 01, pp. 322–327, 2020.

[10] Q. Hidayati, N. Yanti, and N. Jamal, “P-7 SISTEM PEMBANGKIT PANEL SURYA DENGAN SOLAR TRACKER DUAL AXIS Tracker Cerdas dan Murah Berbasis membahas Sistem Kerja Solar Sell Dalam Solar Panel Tipe Polikristal yang dimana penelitian ini hanya sebatas mengukur hasil Perancangan Sistem Perancangan Sistem dibagi menjadi 3,” pp. 68–73, 2020.

[11] C. Kasburg *et al.*, “Hybrid deep learning for power generation forecasting in active solar trackers,” doi: 10.1049/iet-gtd.2020.0814.

[12] A. K. Podder, N. K. Roy, and H. R. Pota, “MPPT methods for solar PV systems : a critical review based on tracking nature,” doi: 10.1049/iet-rpg.2018.5946.

[13] A. Hussain, A. Batra, and R. Pachauri, “An experimental study on effect of dust on power loss in solar photovoltaic module,” *Renewables Wind. Water, Sol.*, 2017, doi: 10.1186/s40807-017-0043-y.

[14] I. W. Sutaya and K. U. Ariawan, “SOLAR TRACKER CERDAS DAN MURAH BERBASIS MIKROKONTROLER 8 BIT ATMega8535,” vol. 5, no. 1, pp. 673–682, 2016.

[15] N. Al-rousan, N. Ashidi, M. Isa, M. Khairunaz, and M. Desa, “Journal of King Saud University – Engineering Sciences Efficient single and dual axis solar tracking system controllers based on adaptive neural fuzzy inference system,” *J. King Saud Univ. - Eng. Sci.*, vol. 32, no. 7, pp. 459–469, 2020, doi: 10.1016/j.jksues.2020.04.004.

JURNAL ECOTIPE
Electronic, Control, Telecommunication, Information, and Power Engineering

Volume 11, Issue 1, April 2024, pp. 46-54
ISSN 2355-5068 ; e-ISSN 2622-4852
DOI: 10.33019/jurnalecotipe.v11i1.4482

Motion Control of 5-Degree of Freedom Humanoid Robot Arm System Using Fuzzy Logic Algorithm

Ike Bayusari[1], Darma Sandi[2], Rahmawati[3], Sri Agustina[4], Suci Dwijayanti[5],
Bhakti Yudho Suprapto[6]
[1,2,3,4,5,6] Electrical Engineering, Universitas Sriwijaya, Palembang-Prabumulih street KM. 32, Inderalaya,
Ogan Ilir 30662, Indonesia

ARTICLE INFO

Article historys:

Received : 23/12/2023
Revised : 22/01/2024
Accepted : 01/04/2024

Keywords:

Fuzzy Logic; Humanoid Robot; Robotic Arm; Sugeno Method

ABSTRACT

Humanoid robots are the evidence of the rapid advancement of technology in robotics. One of their applications is replacing humans in certain tasks, such as moving goods. For this type of activity, humanoid robots need arms; however, their arm system is not effective enough because of the material used. Thus, this study proposes the use of filament as the material of frames in robot arms. A 5-degree of freedom (DoF) robot arm system was implemented, and the motor worked as the driving force. The movement of this robotic arm was based on proximity and camera sensor readings. Then, the movement control used fuzzy logic with the Sugeno method. During experimental testing, the humanoid robot arm could grip and move objects from one place to another at varying times according to the object type. The length of time obtained depends on the reading of the proximity sensor on the gripper. In another experiment, the humanoid robot arm could shake hands with humans in real time within 36 sec. In conclusion, the results verified the effectiveness of the proposed fuzzy logic controller with the Sugeno method.

Corresponding Author:

Bhakti Yudho Suprapto
Electrical Engineering Universitas Sriwijaya, Palembang-Prabumulih street KM. 32, Inderalaya, Ogan Ilir 30662, Indonesia
Email: bhakti@ft.unsri.ac.id

1. INTRODUCTION

Industrial technology has been rapidly developing; currently, industry 4.0 has automated many systems. Human work has begun to be replaced by machines or robots for various tasks, such as cleaning houses, communicating with humans, walking, and moving and lifting objects from one place to another. For these purposes, artificial intelligence and the Internet of Things (IoT) have been used[1,2]. In addition, robots have been designed to perform physical interactions with humans, such as shaking hands, lifting, moving, and assembling objects. A robot arm system works automatically using control assistance to maintain movement and the process of lifting and placing an object. It can also be combined with sensors and cameras to detect an object and determine its coordinates. The object detection and coordinates are the inputs processed using image processing; the automatic movement of the robot arm is the output [3].

Several studies have been conducted on robot arms, including 5-degree of freedom (DoF) position control for a kinematic controller for handshaking on humanoid robots [4], 2-DoF robotic arms based on the adaptive neuro-fuzzy inference system (ANFIS) [5,6], and the fuzzy logic algorithm for controlling the movement of 4-DoF robotic arms [7, 8]. However, the robot arms in these studies could not automatically shake hands, and the robots moved slower compared with human dynamics [4]; thus, it took more time to automatically lift and move objects. Moreover, the distance to reach the object was very limited [5]. Additionally, using a manual system requires a lot of time and energy; hence, such robot arms are inefficient and ineffective [9]. Therefore, in this study, we designed the robot arm with 5 DoF to extend the robotic arm range. The proposed robot arm could lift and move objects, and shake hands. The input used in this study was based on camera and proximity sensor readings. The fuzzy logic algorithm was utilized as a controller due to its simplicity, ease of understanding, flexibility, and tolerance for inaccurate data, making it suitable for moving humanoid robotic arms. This fuzzy logic algorithm has been widely used in various fields such as economics [10], manufacturing industry [11,12], transportation [13, 14], environmental and social sciences, businesses [15], and pico hydro systems [16] because of these advantages. The difference in this research compared to previous studies lies in the utilization of a 5-degree-of-freedom (5 DOF) robotic arm, which facilitates both movement and reach. Additionally, it incorporates a handshake capability based on a Fuzzy Logic controller employing several membership functions.

2. RESEARCH METHOD

The process of lifting and moving items by a humanoid robot arm was carried out in several stages, as shown in Fig. 1. The humanoid robot arm was designed to make it easier to place the servomotor and components, as shown in Fig. 2. The humanoid arm was made of filament and printed using a 3D printer.

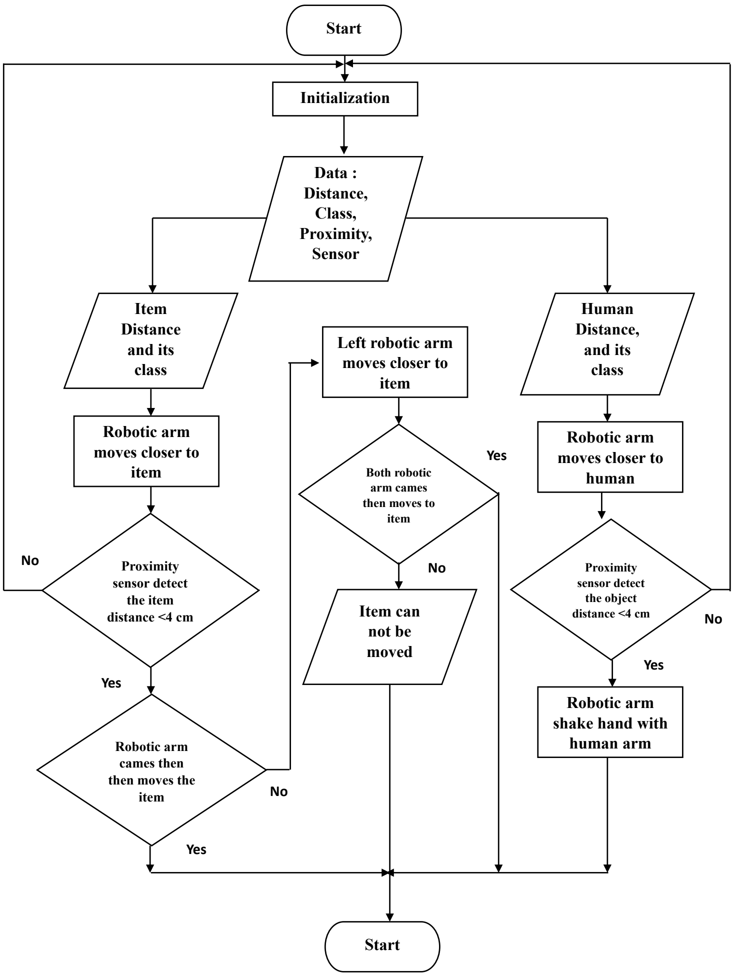

Figure 1. System flowchart

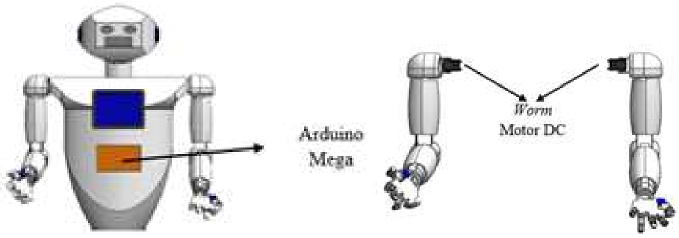

(a) Body of robot (b) Arm System

(b) Arm Joint (d) Gripper

Figure 2. Design of robotic arm

The arm robot was made based on the design and printed with a 3D printer using filament material, as shown in Fig. 3. The components used in the arm robot include DC worm motors, servomotors, proximity sensors, limit switches, and other microcontrollers that were arranged inside the humanoid arm and body. The movement of the humanoid robot arm was controlled by the Arduino Mega microcontroller. The driving force of each arm was controlled using seven servomotors placed at the 3rd, 4th, and 5th DoF as grippers; and two 12V DC worm gear motors were placed at the 1st and 2nd DoF, which can be seen in Fig. 3. The robot arm was made using a filament as the base material, thus functioning as the substrate for the placement of the components and sensors used.

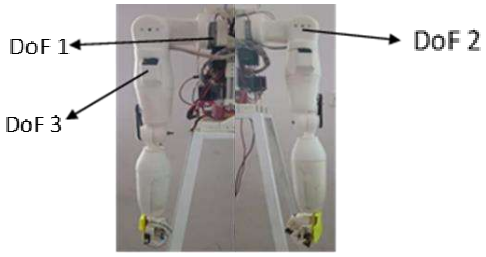

Figure 3. Design of robotic arm

Whereas a fuzzy membership represents the distance input and readings from the crisp distance sensor that is changed into a fuzzy set. The membership function of this fuzzy system uses three variables: object and human distance, x-distance, and ultrasonic sensor distance. In this study, a fuzzy set was used to determine the movement of the humanoid robot arm. The set was divided into five classes: very far, far, medium, close, and very close. The membership function of each variable can be seen in Figs. 4, 5, and 6, in the form of object and human distance variables, x-distance variables, and ultrasonic sensor distance variables, respectively.

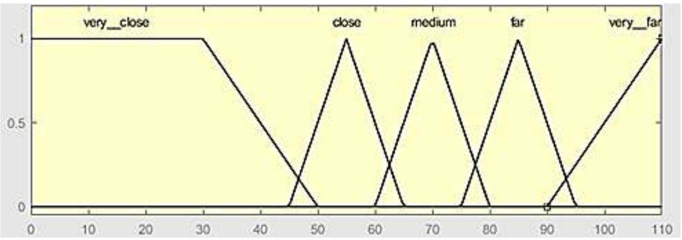

Figure 4. Distance variable curves of objects and human

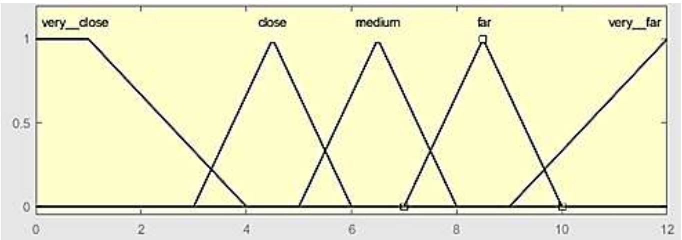

Figure 5. X-distance variable curve

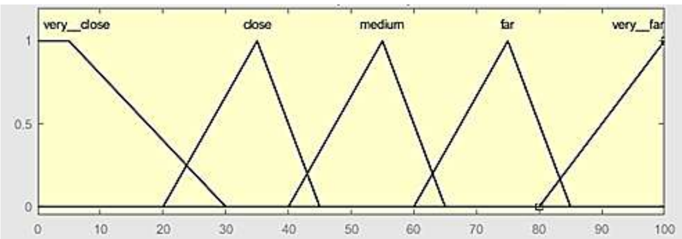

Figure 6. Ultrasonic sensor distance variable curve

After determining the membership function, the next step is to compile fuzzy rules used as a reference for the process of acquiring the output of the robot arm movement. In this study we used three types of variables with five membership functions in order to obtain the fuzzy rules, that is, we had 125 rules in total.

3. RESULTS AND DISCUSSION

3.1 Humanoid Robot Performance Testing

First, the robotic arm was tested for movement without using the fuzzy logic method. These tests included the movements of the 1-DoF, 2-DoF, 3-DoF, and 4-DoF. Next, the gripper was evaluated for opening and closing, and the proximity sensor readings on the gripper were also tested. The test was carried out to ensure that the components worked well so that the robotic arm as a whole would work well in moving objects using the Sugeno fuzzy logic method. The test of the robotic arm using the Sugeno fuzzy logic method was carried out six times: (1) standby position, as the start and end positions of the robotic arm; (2) lifting eggs; (3) lifting an empty mineral water bottle; (4) lifting a filled mineral water bottle; (5) lifting a glass of water; and (6) shaking hands directly with humans. The humanoid arm test was performed 20 times with changes in the object's distance from the robotic arm. Table I presents the distance data of the object to be moved from the robotic arm.

Based on the data in Table 1, the input value of the distance used varies, while the output of the linguistic variable was determined in advance from the calculation of fuzzy 'Gripping1' and 'Gripping' with the servomotor angle on the robot arm. When the input distance between objects and humans is 65, the x-distance is 30, and the sharp distance is between 5 to 12; the output of the fuzzy calculation is 'Gripping1', with the 1-DoF to 4-DoF servomotor angles being 140°, 100°, 120°, and 20°. Furthermore, when the input distance between objects and human is 65, the x-distance is between 20 to 45, and the sharp distance is less than 12; then, the result of Sugeno fuzzy logic calculation is 'Gripping', with the 1-DoF to 4-DoF servomotor angles being 140°, 100°, 10°, and 20°. The 5-DoF represents a gripper with a shape resembling a human hand's palm, equipped with five fingers as a tool for clamping objects. The output data from the gripper test on the humanoid robot arm can be seen in Table 2.

Table 1. Humanoid Arm Testing

No	**Input**			**Output**				
	Distance between objects & human	**x-axis distance**	**Linguistic Variable**	**Distance between objects & human**	**x-axis distance**			
					1	**2**	**3**	**4**
1	30	6	2	Gripping	140^0	100^0	120^0	20^0
2	45	10	4	Gripping	140^0	100^0	120^0	20^0
3	50	20	6	Gripping	140^0	100^0	120^0	20^0
4	55	8	3	Gripping	140^0	100^0	120^0	20^0
5	60	11	5	Gripping	140^0	100^0	120^0	20^0
6	65	16	8	Gripping	140^0	100^0	120^0	20^0
7	30	20	2	Gripping	140^0	100^0	120^0	20^0
8	34	25	5	Gripping	140^0	100^0	120^0	20^0
9	37	27	6	Gripping	140^0	100^0	120^0	20^0
10	40	30	8	Gripping	140^0	100^0	120^0	20^0
11	45	35	4	Gripping	140^0	100^0	120^0	20^0
12	50	40	10	Gripping	140^0	100^0	120^0	20^0
13	50	20	7	Gripping	140^0	100^0	120^0	20^0
14	53	25	10	Gripping	140^0	100^0	120^0	20^0
15	60	30	3	Gripping	140^0	100^0	120^0	20^0
16	65	33	6	Gripping	140^0	100^0	120^0	20^0
17	43	33	3	Gripping	140^0	100^0	120^0	20^0
18	48	37	7	Gripping	140^0	100^0	120^0	20^0

Table 2. Testing of Humanoid Arm Gripper

No	**Objects**	**Thumb**	**Index**	**Middle**	**Ring**	**Pinkie**
1	Egg	180^0	110^0	102^0	30^0	40^0
2	Empty water bottle	130^0	90^0	124^0	80^0	90^0
3	Full water bottle	130^0	100^0	77^0	70^0	80^0
4	Plastic glass of water	140^0	90^0	89^0	90^0	70^0
5	Human hand	90^0	70^0	50^0	70^0	83^0

Based on Tables 1 and 2, the output either changes the servomotor angle of each joint or the DoF of the humanoid arm during lifting and moving objects. This can be seen in the movement graphs of the humanoid robotic arm and the gripper. Then, the humanoid robot arm was tested 20 times with five different types of objects. Table 3 presents the results of a real-time humanoid robot arm test.

Table 3. Testing of Humanoid Arm Gripper

Test	**Object**	**Photo**	**Information**
1	Egg		The humanoid robotic arm successfully moves the object.
2	Egg		The humanoid robotic arm successfully moves the object.

3	Egg		The humanoid robotic arm successfully moves the object.
4	Egg		The humanoid robotic arm successfully moves the object.
5	Empty water bottle		The humanoid robotic arm successfully moves the object.
6	Empty water bottle		The humanoid robotic arm successfully moves the object.
7	Empty water bottle		The humanoid robotic arm successfully moves the object.
8	Empty water bottle		The humanoid robotic arm successfully moves the object.
9	Full water bottle		The humanoid robotic arm successfully moves the object (both arms).
10	Full water bottle		The humanoid robotic arm unsuccessfully moves the object (both arms).
11	Full water bottle		The humanoid robotic arm unsuccessfully moves the object (both arms).
12	Full water bottle		The humanoid robotic arm unsuccessfully moves the object (single arm).
13	Plastic glass of water		The humanoid robotic arm successfully moves the object.

14	Plastic glass of water		The humanoid robotic arm successfully moves the object.
15	Plastic glass of water		The humanoid robotic arm unsuccessfully moves the object.
16	Plastic glass of water		The humanoid robotic arm successfully moves the object.
17	Handshake		The humanoid robotic arm successfully moves the object.
18	Handshake		The humanoid robotic arm successfully moves the object.
19	Handshake		The humanoid robotic arm successfully moves the object.
20	Handshake	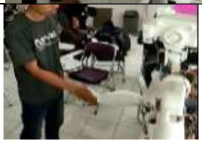	The humanoid robotic arm successfully moves the object.

Based on Table 3, the system of the humanoid robotic arm managed to move objects in real time. The humanoid robotic arm completed clamping and moving objects properly without deforming the object being moved. To determine the accuracy of the system's success in moving the objects with an overall accuracy rate of 65% based on Table III, the robotic arm has an accuracy of 50%, 75%, 75%, and 100% for moving eggs, moving the empty water bottle, moving the full water bottle, moving the plastic glass of water, and shaking hands with humans, respectively. The angular movement of each DoF of the humanoid robotic arm can be seen on each graph in Fig. 7.

4.1. Test of movement arm robot

The humanoid robotic arm was tested to lift and move a soft egg. It successfully moved the egg by clamping and lifting it, as shown in Fig. 7(a), without deforming or breaking it. Meanwhile, the robotic arm movement while lifting eggs is 50 second for a time duration.

(a) arm lifts the egg (b) arm lifts the full water bottle

(c) arm lifts the plastic glass of water (d) handshaking test

Figure 7. The humanoid robotic arm testing

Fig. 7(b) shows the test of the robotic arm lifting a full water bottle. As using a single arm cannot move it the robotic system uses both arms to lift and move it. Fig. 7(c) shows that the humanoid robotic arm has successfully gripped and moved the plastic glass of water; it takes 50 second to move the plastic glass of water. Fig. 7(d) shows that the humanoid robotic arm successfully interacts with a human in real time and it takes 45 second the gripper movement while handshaking. To evaluate the humanoid robot arm using the Sugeno fuzzy logic method as seen in Table 4.

Table 4. Accuracy Type of Test

Action / object	Experiments	Accuracy
eggs	15	13.333%
empty mineral water bottle	12	58.333%
bottle filled with water	46	4.761%.
glass	6	66.666%.
shaking hands	5	100%

From Table 4, tests were carried out with five different types of objects, including eggs with an accuracy of 13.333% from 15 tests. This happened because it was difficult for the robot arm to clamp the egg due to its small diameter and round shape, which caused the distance sensor reading on the gripper to not be detected. The second test was carried out with an empty mineral water bottle where the robot obtained an accuracy of 58.333% from 12 experiments. In this test, the accuracy was higher because the diameter and height of the mineral water bottle exceeded the size of the gripper, thereby making it easy for the distance sensor to detect the mineral water bottle. The third test was conducted with a bottle filled with water, where both the arms of the humanoid robot were used. This test was carried out 42 times with a very small success of 4.761%. This was due to the fact that the gripper was too large, and it lacked the necessary clamping force. Thus, the robotic arm could not move the bottle filled with water. The fourth test, using a glass, was conducted six times, and the robot obtained an accuracy value of 66.666%. In this test, there were two attempts that were not successful, caused by the thumb on the gripper not clamping a part of the glass. The fifth and the last test involved interaction with humans by shaking hands. The humanoid robot arm showed good performance at shaking hands with humans, obtaining an accuracy of 100% from five experiments. This was due to the ability of the proximity sensor on the gripper to detect human hands very quickly and efficiently.

4. CONCLUSION

The implementation of the zero-order Sugeno fuzzy logic method in the movement of the humanoid robotic arm in moving objects or shaking hands has been successfully performed in an automated manner. The humanoid robotic arm was able to successfully move objects such as a water bottle (empty and full) and plastic glass of water; it could hold an egg for 30 second without breaking it. Additionally, it could shake hands directly with humans, taking 36 second to complete the handshake command. Future research will be implemented systemically so that this humanoid robot will be able to carry out activities like humans in providing services.

Acknowledgments

This research was funded by Faculty of Engineering, Sriwijaya University, Fiscal Year 2022 with contract number 023.17.2.677515/2022 dated November, 17, 2021 and accordance with the Rector Decree number: 0390/UN9.FT/TU.SK/2022 dated on May, 13, 2022.

REFERENCES

[1] R. Pinillos, S. Marcos, R. Feliz, E. Zalama, and J. Gómez-García-Bermejo, "Long-term assessment of a service robot in a hotel environment," *Rob. Auton. Syst.*, vol. 79, pp. 40–57, 2016.

[2] A. Stăncioiu, "The Fourth Industrial Revolution 'Industry 4.0,'" *Fiabil. Şi Durabilitate*, vol. 1, no. 19, pp. 74–78, 2017.

[3] P. Tsarouchi *et al.*, "Robotized assembly process using dual arm robot," *Procedia CIrP*, vol. 23, pp. 47–52, 2014.

[4] A. Melnyk and P. Henaff, "Bio-inspired plastic controller for a robot arm to shake hand with human," in *2016 IEEE 36th International Conference on Electronics and Nanotechnology (ELNANO)*, 2016, pp. 163–168.

[5] A. Sambas and D. S. Rahayu, "Rancang Bangun Robot Arm 2 DOF Berbasis Adaptive Neuro-Fuzzy Inference System (ANFIS)," *Al-Jazari J. Mech. Eng.*, vol. 3, no. 2, pp. 41–45, 2018.

[6] A. S. Trisnawan and D. S. Rahayu, "Rancang Bangun Robot Arm 2 DOF Berbasis Adaptive Neuro-Fuzzy Inference System (ANFIS)."

[7] T. Dewi, S. Nurmaini, P. Risma, Y. Oktarina, and M. Roriz, "Inverse kinematic analysis of 4 DOF pick and place arm robot manipulator using fuzzy logic controller.," *Int. J. Electr. Comput. Eng.*, vol. 10, no. 2, 2020.

[8] K. Lochan and B. K. Roy, "Control of two-link 2-DOF robot manipulator using fuzzy logic techniques: a review," in *Proceedings of fourth international conference on soft computing for problem solving*, 2015, pp. 499–511.

[9] Salim Chennai, "Performance Analysis of Universal Power Quality Conditioner Systems Based on Seven-level NPC Inverter Using PD-SPWM with Fuzzy Control Scheme," *Period. Polytech. Electr. Eng. Comput. Sci.*, vol. 66, no. 4, pp. 315–324, 2022, doi: https://doi.org/10.3311/PPee.20140.

[10] V. Scherger, H. P. Vigier, and M. G. Barberà-Mariné, "Finding business failure reasons through a fuzzy model of diagnosis," *Fuzzy Econ. Rev.*, vol. 19, no. 1, p. 45, 2014.

[11] A. Susilawati, J. Tan, D. Bell, and M. Sarwar, "Fuzzy logic based method to measure degree of lean activity in manufacturing industry," *J. Manuf. Syst.*, vol. 34, pp. 1–11, 2015.

[12] I. J. Orji and S. Wei, "An innovative integration of fuzzy-logic and systems dynamics in sustainable supplier selection: A case on manufacturing industry," *Comput. Ind. Eng.*, vol. 88, pp. 1–12, 2015.

[13] A. Sarkar, "Application of fuzzy logic in transport planning," 2012.

[14] S. Rajak, P. Parthiban, and R. Dhanalakshmi, "Sustainable transportation systems performance evaluation using fuzzy logic," *Ecol. Indic.*, vol. 71, pp. 503–513, 2016.

[15] R. S. Santos, J. Soares, P. C. Marques, H. V. G. Navas, and J. M. Martins, "Integrating business, social, and environmental goals in open innovation through partner selection," *Sustainability*, vol. 13, no. 22, p. 12870, 2021.

[16] C. Y. Kang, H. Nabipour, H. S. Chua, and C. C. Kang, "Design of Battery Energy Storage System (BESS) with Fuzzy Control for Pico Hydro," 2021.

JURNAL ECOTIPE
Electronic, Control, Telecommunication, Information, and Power Engineering
Volume 11, Issue 1, April 2024, pp. 55-65
ISSN 2355-5068 ; e-ISSN 2622-4852
DOI: 10.33019/jurnalecotipe.v11i1.4472

Design of Dipole Antenna at 433 Mhz ISM Band for Underwater to Land Communication

Erna Alimudin[1], Arif Sumardiono[2], Riyani Prima Dewi[3], Saepul Rahmat[4], Hendi Purnata[5], Novita Asma Ilahi[5]
[1,2,3,4,5] Electronics Engineering, Cilacap State of Polytechnic, Jl. Dr. Soetomo No. 1, Cilacap 53212, Indonesia

ARTICLE INFO

Article historys:

Received : 09/11/2023
Revised : 08/01/2024
Accepted : 01/04/2024

Keywords:

Dipole Antenna; Underwater to Land Communication; VSWR; S11; ISM Band

ABSTRACT

This research has designed a dipole antenna which is intended for communication underwater to land that worked and was implemented into prototype form. Design using the software Ansoft High-Frequency Structural Simulator (HFSS) v13 and analyze parameters which are generated in simulation results, namely the Voltage Standing Wave Ratio (VSWR), reflection coefficient (S11), the radiation pattern of two-dimensional and three-dimensional. On its design was made of two dipole antennas that can work in a system as a transmitter and receiver. Both of these-dipole antenna operating at ISM 433 MHz frequency band and produce VSWR = 1.62 at the transmitter antenna and = 1.406 on the receiving antenna. In addition, has been measured radiation patterns by antenna performance. From the results of radiation patterns measurements, two pieces of Main Lobe in its field azimuth.

Corresponding Author:

Erna Alimudin
Cilacap State of Polytechnic, Jl. Dr. Soetomo No. 1, Cilacap 53212, Indonesia
Email: ernaalimudin@pnc.ac.id

1. INTRODUCTION

Antenna is defined in Webster's Dictionary as a metallic device which in general used for radiating or receiving radio waves in rod or wire form. Meanwhile, the IEEE Standard Definitions of Terms for Antennas (IEEE Std 145-1983)* defines an antenna or aerial as a device for radiating or receiving radio waves. [1]

Another definition states that an antenna (antenna or aerial) is a device that functions to transfer electromagnetic wave energy from the physical channel media to the air or vice versa from the air to the physical channel media. Because it is an intermediary device between the physical channel media and the air, the antenna must have properties that match the supplying physical channel media. [2] The antenna functions as a transition medium between free space and a transmission channel which can be in the form of a coaxial channel or guided wave which has the function of carrying electromagnetic energy from the transmitting source to the antenna or from the antenna to the receiving system. [3] In a system consisting of a sender and a receiver, of course an antenna is needed as a tool that will transmit information. This information signal will be processed into electromagnetic waves which are then emitted through the antenna. [4]

Underwater wireless communication is a form of communication that uses water as its propagation medium. In this case, communication from underwater to land is also included in underwater communication. Underwater communication with land control certainly has different characteristics. Because this communication is through transmission lines on two different mediums. This of course will affect the performance of the antenna. [5] Therefore, it is necessary to do good design and planning by reviewing two different media, namely water and air to make an antenna that can work optimally in the two media.

Wireless communication from underwater to land is utilized for various aspects. Communication for submarines uses underwater-to-ground wireless technology to determine the location of the submarine and facilitate the exchange of information from the submarine to headquarters on land. [6]

Submarine technology uses sonar as its communication. This is because at very low frequencies, the wavelength will also be greater. With a large wavelength, the frequency will be more resistant to attenuation so that the attenuation experienced by water becomes smaller. Thus, the transmission of information underwater becomes more possible using low frequencies. However, because it uses a low frequency, the dimensions of the antenna are getting bigger. In accordance with the wavelength formula (λ=c/f), the lower the frequency value, the greater the wavelength value. This wavelength value is directly related to the dimensions of the antenna. The greater the wavelength, the larger the dimensions of the antenna used. [7]

Radio Frequency (RF) describe as electromagnetic waves that have wavelengths which usually used in radio communications. [8] Radio frequencies range from very low frequency (vlf), which ranges from 10 to 30 kHz, to extremely high frequency (ehf), which ranges from 30 to 300 GHz. Radio waves propagate at a frequency of 100,000 Hz to 100,000,000,000 Hz, while audio waves propagate at a frequency of 20 Hz to 20,000 Hz. in radio broadcasts, audio waves are not transmitted directly but are superimposed on radio waves that will propagate through space. there are two methods of transmitting audio waves, namely through amplitude modulation (AM) and frequency modulation (FM). [9]
The frequency bands available for industrial, scientific and medical (ISM) applications are from 6.78 Mhz to 245 GHz. The study before recommendd the next research to using the RF module 433 operating at 433MHz to provide higher throughput, lower end-to-end delay and cheaper in case of Air-to-Air, Air-to-Water, and for long distance water-water communications with a low throughput. [10] According to the size of the antenna designed, the center frequency from the middle range was chosen as the frequency used. The frequency was 433 MHz.

2. RESEARCH METHOD

In this research, two dipole antennas have been made that function as transmitters and receivers through the water-to-land propagation medium. The two dipole antennas will be mounted on a ground-based receiving prototype and the transmitting antenna will be placed on a transmitter prototype that will be submerged in water.

The antenna that has been designed is in the ism 433 MHz frequency band. The selection of this frequency band is based on the consideration that the desired antenna size is not larger than the size of the prototype submarine that is planned to be used. On conventional submarines, the antenna that is commonly used has very large dimensions because it is operated at a low frequency band (audio). This is because at very low frequencies, the attenuation experienced by the water becomes smaller. Thus, transmitting information underwater becomes more possible using low frequencies. According to the wavelength formula (λ=c/f), if the lower the frequency value, the greater the wavelength value. This wavelength value is directly related to the dimensions of the antenna. The greater the wavelength, the larger the dimensions of the antenna used. For more details, as in the following equation.

$$(\lambda=c/f) \tag{1}$$

$$(l=\lambda/2) \tag{2}$$

The antenna designed is projected to be used for diver robots that are not too large dimensions. The 433 MHz frequency is used because the dimensions of the antenna at this frequency are quite proportional to the size of the submarine and the attenuation because the water experienced at this frequency is not too large when compared to the higher frequency band of 433 MHz.

The antenna is implemented as a transmitting and receiving antenna that can be used for communication from underwater to land with a compact and proportional design for the prototype to be used and can meet the operating frequency for that communication. In this design, two dipole antennas have been made using the software AnSoft High Frequency Structural Simulator Version 11

(HFSSV11). In addition, a dipole antenna prototype has been made so that direct testing can be carried out to compare the simulation results with direct testing.

2.1. Antenna Parameters

According to the IEEE Standard Definition of Terms for Antennas, the parameters to describe antenna performance are radiation pattern, radiation intensity, beam width, directivity, gain, bandwidth, polarization, and input impedance. Other parameters that also determine the success of the antenna performance are the Voltage Standing Wave Ratio (VSWR) and the reflection coefficient (S11). [11]

2.2. Radiation Pattern

Antenna radiation pattern is a diagram that describes the direction and magnitude of antenna radiation. Basically, the antenna radiation pattern has a ball-like shape, to make it easier to calculate and describe, it is arranged into two horizontal radiation patterns and a vertical radiation pattern. [12] Often, the radiation pattern is determined in the far field and is represented as a function of the directional coordinates.

Half Power Beam Width (HPBW) is the angular width that separates the two half power points on the main beam of the radiation pattern. HPBW can be calculated by finding the -3 dB point from the maximum value of the radiation pattern. Front To Back Ratio is the ratio between the maximum power emitted on the main lobe and the power on the back lobe [1]. Front To Back Ratio (FTBR) is the ratio between the maximum power emitted on the main lobe and the power on the back lobe.The value of the front to back ratio (FTBR) can be determined by comparing the antenna power at the maximum power reception level (position 00 on the main lobe) and in the opposite direction (position 1800 on the back lobe). However, it can also compare the power of the antenna when the position is 900 in the main lobe position and the power of the antenna when the position is 2700 in the back lobe position. So, thus comparing antenna power at a certain angular position is not an absolute (certain) thing and cannot be changed, but the determination of the angular position depends on the position of the main lobe and back lobe which are in the radiation pattern.

2.3. Radiation Intensity

Radiation intensity is defined as the power radiated from an antenna per unit space angle. Radiation intensity is a far field parameter and can be generated by multiplying the radiation density by the square of the distance Mathematically expressed as:

$$\mathrm{U} = \mathrm{r}^2 \mathrm{W}_{\mathrm{rad}} \tag{3}$$

where:
U = radiation intensity (W/space angle unit)
Wrad = radiation density (W/m2)
r = radiation radius (m)

2.4. Beamwidth

The beam width of an antenna radiation pattern is defined as the angle of separation between two points equal to opposite sides of the maximum pattern. In an antenna radiation pattern, there are several beam widths. One of the beamwidths used is Half Power Beamwidth (HPBW), which is defined by the IEEE that in a plane containing the direction of the maximum beam, the angle between the two directions is the radiation intensity half of the beam value. Another important beamwidth is the angle of separation between the first points of the pattern which is called the First Null Beamwidth (FNBW). In practice the term beamwidth is usually referred to as HPBW. [2]

2.5. Dipole Antenna Design

The dipole antenna that has been designed is used for communication purposes through two types of propagation which have very different characteristics, namely through the medium of seawater to land. This antenna is designed to operate in the unlicensed ISM 433 MHz frequency band. The design of this antenna is desired as an antenna whose radiation pattern is omnidirectional, that is, it has a pattern in a certain plane (azimuth) and a directional pattern in an orthogonal plane (elevation). The design of a dipole antenna has gone through three main stages. First, determine the specifications and dimensions of the dipole antenna design. The second is designing with Ansoft HFSSv11 software so that the expected results are obtained. The third is the prototyping process to test the success of the design.

The first stage of design is to determine the specifications and dimensions of the dipole antenna. The important parameters in designing a dipole antenna are as follows:

- Operating frequency (f_o) : The resonant frequency of the selected antenna is in the unlicensed ISM band, at 433MHz. So that the specified resonant frequency is 433 MHz
- Relative permittivity (ε_r): The conductor material used in this design is Aluminum (aluminum) which has a permittivity of $\varepsilon_r = 1$. The choice of this conductor material is based on the ease of obtaining it at a raw material store, as well as its closeness to the Perfect Electric Conductor (PEC), which also has a permittivity of the material $\varepsilon_r = 1$. While the insulating material used is Polyethylene with a permittivity of $\varepsilon_r = 2.25$ and a dielectric loss tangent of 0.001. The choice of this insulator material is based on its closeness to porcelain insulators with a dielectric loss tangent of 0.
- Antenna diameter: The width of the diameter used for this dipole antenna is 7 mm or with a radius (r) = 3.5 mm with the characteristics of a solid material. The reason for choosing this dimension is because it can be easily obtained on the market and is more capable of radiating waves in water when compared to those with holes.
- Impedance: The input impedance used in the design of this dipole antenna is 50 Ω.
- Selection of an insulating material of polyethelene or plastic that is resistant to water pressure as the material for wrapping the antenna and its transmitter device when submerged in water. The choice of this material is not only because it is easy to obtain, but also because of its ability to protect the device from water so that a short circuit does not occur due to exposure to water which can damage the prototype transmitter and its antenna.

The second stage is designing the dimensions of the dipole antenna using Ansoft High Frequency Structural Simulator Version 11 software. The length of the dipole antenna is greatly influenced by the wavelength. In theory, there are various length sizes of dipole antennas, including ($\ell = \lambda/4$), ($\ell = 3\lambda/4$), ($\ell = \lambda$), ($\ell = 3\lambda/2$), and half-wavelength dipole ($\ell = \lambda/2$) [3]. The type of dipole antenna used as a reference is a $\lambda/4$ dipole or in other words a dipole with a quarter-wave size ($\lambda/4$) on each pole. With fo = 433 MHz then $\lambda = 0.693$ m, so that the length of the Dipole Antenna l = 0.173 m or equal to 17.3 cm. The details show at the Table 1. The antenna design shown at the Figure 1.

Table 1. Dipole Antenna Design

	Pole length	**Gap**	**Radius**	**Material type**	**Boundary type**
Dipole Tx	17.3 cm x 2 pole	3 cm	3.5 mm	Aluminum Solid	*Fresh Water*
Dipole Rx	17.3 cm x 2 pole	3 cm	3.5 mm	Aluminum Solid	*Air*

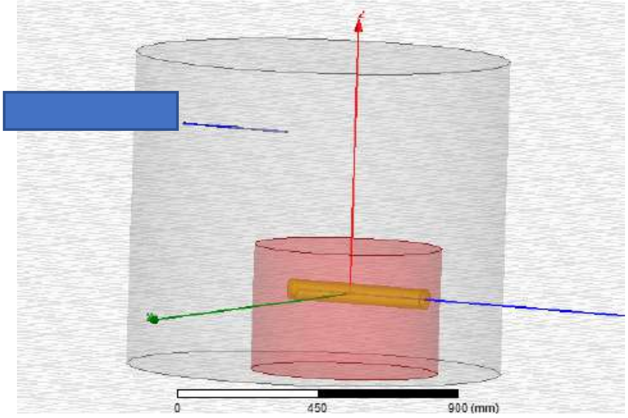

Figure 1. Antenna design simulation

Because the designed antenna is made to operate on two propagation mediums, water and air, the HFSS software design uses two boundaries (water and air), by placing the transmitter antenna in water and the receiver antenna on land. However, because of the characteristic of water which is short circuit when it encounters a material that can conduct electricity, the Rx dipole antenna is placed in a waterproof plastic material. The following is a design simulation image on medium two boundaries.

3. RESULTS AND DISCUSSION

The data from the table 1 above were obtained from themathematical equations and then simulated in the HFSS v.13 software were obtsiner the S11 and S22 values of the two antennas at a frequency of 433 MHz are still far from the optimum antenna standard, which is -4dB on S11 (Tx antenna in water), and -3.54 dB on S22 (antenna receive on land). Because the size obtained from the calculation results after simulation has not yet obtained optimal results in terms of the S11/S22 and VSWR values of the two antennas above, optimization is carried out using the trial-and-error method to obtain more optimal results by considering the environmental correction factor.

The several factors that led to the optimization of the dimensions of the antenna are as follows:

1. Environmental correction factor.
2. After simulating the antenna parameters (S11, VSWR, and radiation pattern), the results are not as expected.
3. Dimensional factors and characteristics of other devices that want to be integrated with the antenna that has been made.

Optimization is carried out by changing the dimensions of the poles and the size of the gap between the two poles of each antenna using the trial-and-error method so that an operating frequency of 433 MHz is obtained. The dipole diameter is set at 7mm. Optimization data shown in Table 2 below.

Table 2. Optimization Data on Dipole Antenna Design

No.	**Pole Length (cm)**	**Receiver Antenna**		**Transmitter Antenna**	
		S11 (dB)	**VSWR**	**S11 (dB)**	**VSWR**
1	17.3	-4.8	3.8	-4.5	4.7
2	16.5	-6	2.75	-5	3.5
3	16	-8	2.3	-6.25	3
4	15	-11	1.85	-8	2.4
5	15.5	-14.5	1.5	-10.5	1.9
6	14.7	-15	1.45	-12.5	1.6
7	**14.4**	**-16**	**1.4**	**-15**	**1.4**
8	14.0	-15	1.5	-12.5	1.7

According to S11 and VSWR which obtained from the 7th simulation result for receiver antenna and transmitter antenna, thus the final dimensions of the two dipole antennas are chosen as follows at Table 3.

Table 3. Dipole Antenna Design After Optimization

	Pole length	**Gap**	**Radius**	**Material type**	**Boundary type**
Dipole Tx	14.4 cm x 2 pole	3 cm	3.5 mm	Aluminum Solid	*Fresh Water*
Dipole Rx	14.4 cm x 2 pole	3 cm	3.5 mm	Aluminum Solid	*Air*

After designing, a simulation process is carried out to obtain antenna parameters such as reflection coefficient (S11/S22), VSWR, HPBW, and radiation pattern. The results shown at Figure 9.

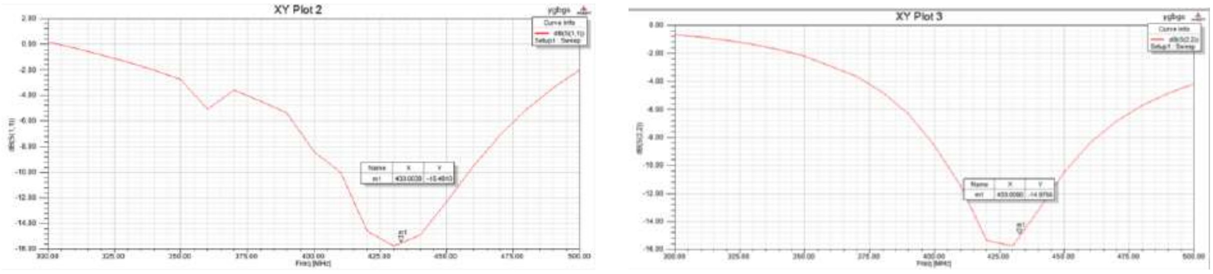

(a) (b)

Figure 9. (a) Reflection Coefficient (S11/S22) and (b) Return Loss Value of S11

From the simulation results, the return loss value of S11 on the underwater transmitting antenna reaches -15.5 dB at a frequency of 433 MHz and has almost fulfilled the desired results. Meanwhile, from the simulation results of the return loss value of S22 on the receiving antenna on the ground, it is -15dB at a frequency of 433 MHz This value is sufficient to meet the standard requirements for the allowable return loss value for each antenna. By using the trial-and-error method, this value is closest to the desired value.

VSWR

VSWR Antenna Transmitter and Receiver

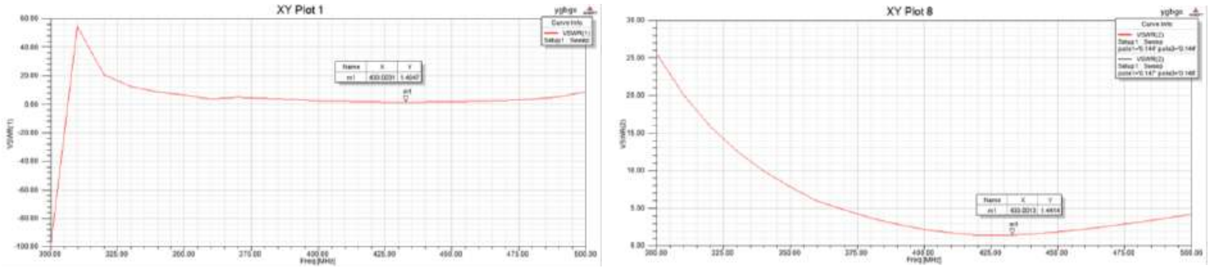

(a) (b)

Figure 10. VSWR (a) Antenna Transmitter and (b) after Optimization

From the simulation results at Figure 10, the value of the Voltage Standing Wave Ratio or VSWR of the two dipole antennas at a frequency of 433 MHz is below 2 so that the VSWR value is 2: 1. This value is as expected because the good VSWR value in signal reception is below 2 and close to 1.

HPBW

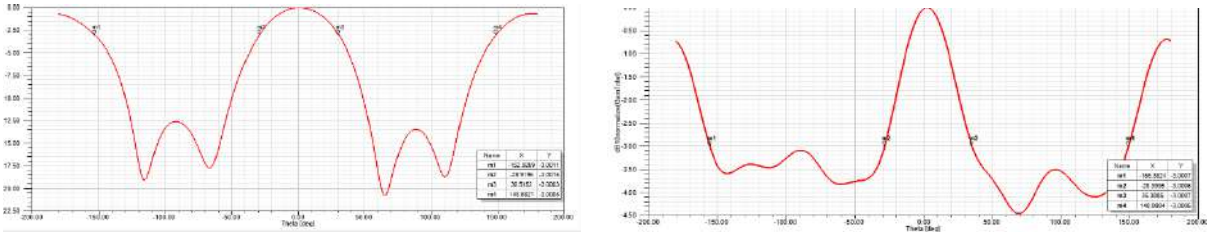

Figure 11. Simulation Results of Azimuthal Radiation Patterns in (a) Rectangular Coordinates and (b) Elevation Field in Rectangular for Dipole Antenna Design

From the simulation results at Figure 11, the -3 dB value in the normalization of the radiation pattern in rectangular coordinates is obtained at around -28° and 30° angles from the maximum radiation direction, so the azimuthal HPBW of the simulated field is 28° + 30° = 58°. This value indicates a large beamwidth. Meanwhile, the radiation pattern for the elevation plane is obtained at an angle of -28° and 35° from the maximum radiation direction, so the HPBW of the azimuthal plane from the simulation results is 28° + 35° = 63°. This value indicates a large beamwidth.

JURNAL ECOTIPE
Electronic, Control, Telecommunication, Information, and Power Engineering
Volume 11, Issue 1, April 2024, pp. 55-65
ISSN 2355-5068 ; e-ISSN 2622-4852
DOI: 10.33019/jurnalecotipe.v11i1.4472

Radiation Pattern

- Duo boundary (Water and Air)

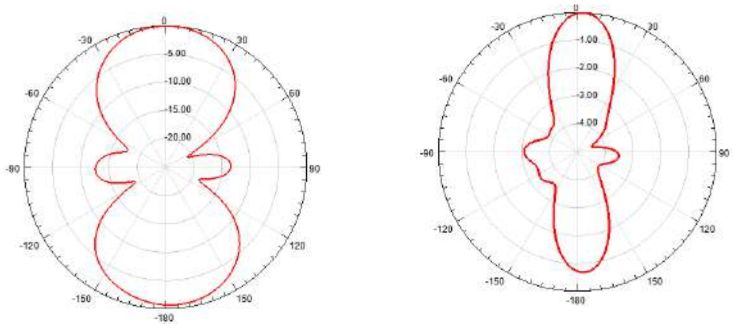

Figure 12. Azimuthal Elevation Duo boundary

- One boundary (Air)

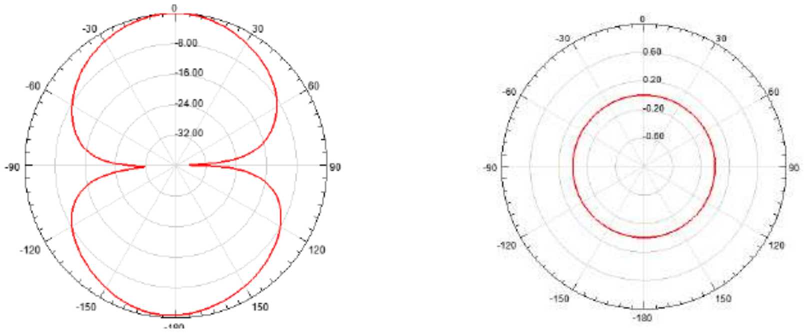

Figure 13. Azimuthal Elevation One Boundary

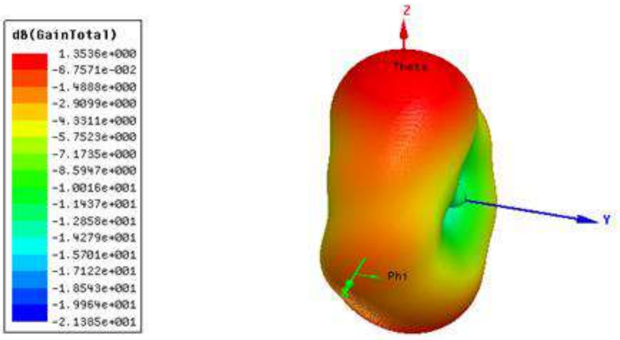

Figure14. Dipole Antenna 3D radiation pattern

Figure 112, Figure 13, and Figure 14 shows that the designed antenna is a directional antenna. Where the antenna radiates electromagnetic waves with a total gain of the antenna from the simulation results of 1.3536 dB. theoretically the maximum gain of a λ/2 dipole antenna is 10 log 1.66 or 2.2 dBi.

Comparison of Simulation Results with Measurement Results

Receiving Dipole Antenna Prototype

Reflection Coefficient (S11)

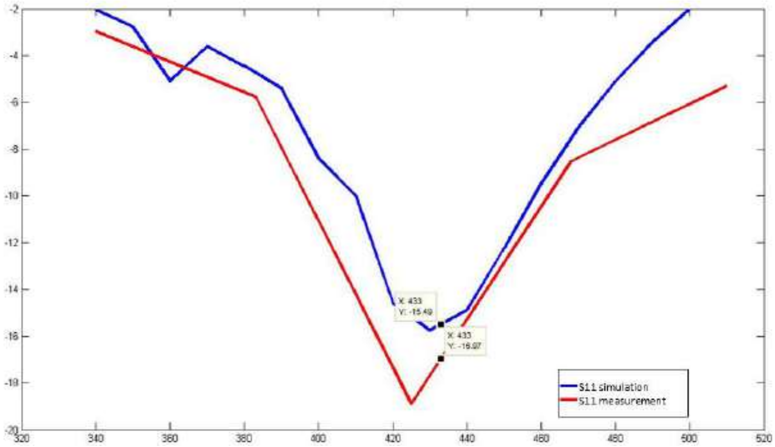

Figure 15. Comparison of S11 measurement results with simulation results receiving antenna

In Figure 15, it can be seen that there are similarities in the S11 graphic pattern between the measurement results and the simulation results. In the simulation, the S11 value tends to reach a frequency of 430 MHz. Meanwhile, in the measurement results, the S11 value tends to decrease to a frequency of 425 MHz. From the measurement results, it was found that the return loss value at the 433 MHz frequency was greater, namely -16.97 dB, while the return loss value in the simulation results was -15.49 dB, so the difference between the two was -1.48 dB. The bandwidth obtained from the measurement results is greater than the simulation results where in the measurement results s11 ≤ -10dB is at a frequency of 398 Mhz to 460 Mhz and in the simulation results at a frequency of 410 Mhz and 458 Mhz. There are differences in measurement results in the image because the area around the measurement room is not free from the influence of electromagnetic wave interference or reflected signals from the transmitting antenna.

VSWR

Figure 16 shows that the VSWR graphic pattern is similar between the measurement results and the simulation results. In the simulation, VSWR has a value of ≤2 starting from a frequency of 410 MHz to 430 MHz. Meanwhile, measurements start from a frequency of 410 MHz to 425 MHz. From the measurement results, it was found that the VSWR value at the 433 MHz frequency was smaller, namely 1.406, while the VSWR value in the simulation was 1.456. Where the difference in VSWR values from measurement results and simulation results is 0.050 dB. The difference between the measurement is due to the area around the measurement room not being free from the influence of electromagnetic wave interference or reflected signals from the transmitting antenna.

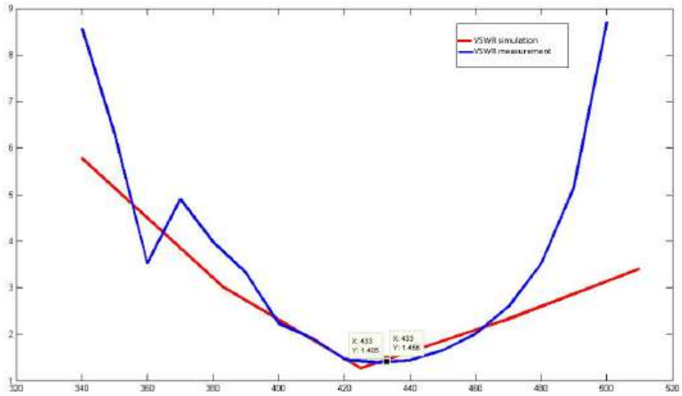

Figure 16. Comparison of VSWR Measurement Results with Simulation Results Receiving Antenna

Transmitting Dipole Antenna Prototype

Reflection Coefficient (S11)

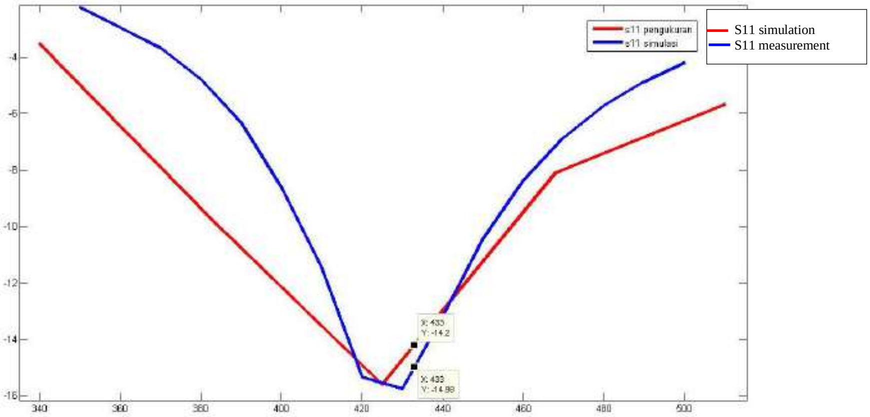

Figure 17. Comparison of S11 Measurement Results with Simulation Results Transmitting Antenna

In Figure 17, it can be seen that there are similarities in the S11 graphic pattern between the measurement results and the simulation results. In the simulation, the S11 value tends to decrease to a frequency of 430 MHz. Meanwhile, the measurement results start from a frequency of 385 MHz to a frequency of 425 MHz. From the measurement results, it was found that the return loss value at the 433 MHz frequency was smaller but still ≤ -10 dB, namely -14.2dB, while the return loss value in the simulation results was -14.98 dB so the difference between the two was -0.78 dB. The bandwidth obtained from the measurement results is greater than the simulation results where in the measurement results s11 ≤ -10dB is at a frequency of 385 Mhz to 458 Mhz and in the simulation results at a frequency of 405 Mhz and 455 Mhz. There are differences in measurement results in the images because the area around the measurement room is not free from the influence of electromagnetic wave interference or reflected signals from the transmitting antenna.

VSWR

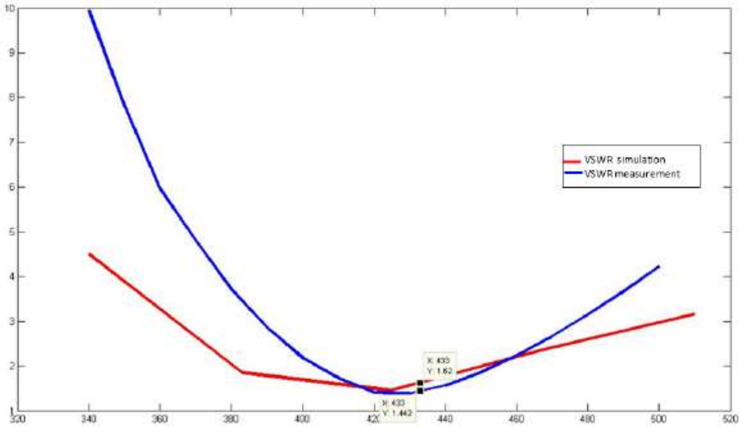

Figure 18. Comparison of VSWR Measurement Results with Simulation Results Transmitting Antenna

From Figure 18, it can be seen that the VSWR graphic pattern is similar between the measurement results and the simulation results. In the simulation, VSWR has a value of ≤2 starting from frequencies 405 MHz to 455 MHz. Meanwhile, measurements start from a frequency of 382 MHz to 450 MHz. From the measurement results, it was found that the VSWR value at the 433 MHz frequency was greater but still had a value of ≤2, namely 1.62, while the VSWR value in the simulation was 1.442. Where the difference in VSWR values from measurement results and simulation results is 0.020 dB. The differences in measurement results in Figure 21 are due to the area around the measurement room not being free from the influence of electromagnetic wave interference or reflected signals from the transmitting antenna.

Volume 11, Issue 1, April 2024, pp. 55-65
ISSN 2355-5068 ; e-ISSN 2622-4852
DOI: 10.33019/jurnalecotipe.v11i1.4472

4. CONCLUSION

Based on the analysis of the simulation results and the results of measurements of the dipole antenna prototype for underwater to ground communication using Ansoft HFSS and MATLAB software, it can be concluded as follows:

1. The selection of the ISM 433 MHz frequency is based on considerations of the propagation conditions encountered and considerations of the size and dimensions of the antenna expected as well as the availability of devices and materials on the market.
2. In determining the dimensions of an antenna, it is very important not only to focus on the theoretical formulation but also to pay attention to the environmental correction factor. In a dipole antenna, a change in the length of the antenna causes a change in the working frequency. In addition, the diameter size and the type of antenna material affect the S11 and VSWR values. The condition of the propagation medium also greatly affects the radiation pattern of the antenna.
3. Optimization of the best size for transmitting and receiving dipole antennas obtained for propagation in water and air mediums is to use a solid aluminium antenna with a diameter of 7 mm and a length of 144 mm for each pole.
4. The VSWR obtained in the antenna design simulation with Ansoft HFSS v13 software meets the ideal standard (VSWR ≤ 2). The VSWR at a working frequency of 433 MHz for the receiving dipole antenna is 1.456 for the simulation results and 1.406 for the measurement results. While the VSWR at the working frequency of the transmitting dipole antenna is 1.442 for the simulation results and 1.62 for the measurement results.
5. S11 obtained in the antenna design simulation with Ansoft HFSS v13 software meets the ideal standard (S11 $\leq$ -10 dB). S11 at a working frequency of 433 MHz for the receiving dipole antenna is -15.49 dB for the simulation results and -16.97 dB for the measurement results. Whereas S11 at a working frequency of 433 MHz for the transmitting dipole antenna is -14.98 dB for the simulation results and -14.2 dB for the measurement results.
6. The results of measurements of the radiation patterns of the two transmitting and receiving dipole antennas while in the air show almost the same results as the simulations in the azimuth and elevation planes. In the azimuth plane the radiation pattern of the two dipole antennas resembles the figure 8 and in the elevation plane they are circular.

REFERENCES

[1] Electronics Engineers, “IEEE Std 145-1983 IE E E Standard Definitions of Terms for Antennas,” *Publ. by Inst. Electr. Electron. Eng.*, vol. 145, 1983.

[2] H. A. Alsawaf and A. E. Kanaan, “Rectangular and circular antennas design for Bluetooth applications,” *Telkomnika (Telecommunication Comput. Electron. Control.*, vol. 21, no. 1, pp. 8–17, 2023.

[3] Y. Li, S. Wang, C. Jin, Y. Zhang, and T. Jiang, “A Survey of Underwater Magnetic Induction Communications: Fundamental Issues, Recent Advances, and Challenges,” *IEEE Commun. Surv. Tutorials*, vol. 21, no. 3, pp. 2466–2487, 2019.

[4] C. E. Santosa, J. T. S. Sumantyo, S. Gao, and K. Ito, “Broadband Circularly Polarized Microstrip Array Antenna with Curved-Truncation and Circle-Slotted Parasitic,” *IEEE Trans. Antennas Propag.*, vol. 69, no. 9, pp. 5524–5533, 2021.

[5] T. Shaneyfelt, M. A. Joordens, K. Nagothu, and M. Jamshidi, “RF communication between surface and underwater robotic swarms,” in *2008 World Automation Congress*, 2008, pp. 1–6.

[6] O. Aboderin, L. M. Pessoa, and H. M. Salgado, “Wideband dipole antennas with parasitic elements for underwater communications,” *Ocean. 2017 - Aberdeen*, vol. 2017-Octob, pp. 1–6, 2017.

[7] A. Massaccesi and P. Pirinoli, “Preliminary results on cylindrical antennas for underwater communication,” *2016 IEEE Antennas Propag. Soc. Int. Symp. APSURSI 2016 - Proc.*, pp.

1895–1896, 2016.

[8] Z. Wang, S. Zhou, and Z. Wang, “Underwater Distributed Antenna Systems: Design Opportunities and Challenges,” *IEEE Commun. Mag.*, vol. 56, no. 10, pp. 178–185, 2018.

[9] G. P. Joshi, S. Y. Nam, and S. W. Kim, *Cognitive radio wireless sensor networks: Applications, challenges and research trends*, vol. 13, no. 9. 2013.

[10] S. M. Maher, Z. M. Ali, H. H. Mahmoud, S. O. Abdellatif, and M. M. Abdellatif, “Performance of RF underwater communications operating at 433 MHz and 2.4 GHz,” *Proc. 2019 Int. Conf. Innov. Trends Comput. Eng. ITCE 2019*, no. February, pp. 334–339, 2019.

[11] Pahrurrozi, C. M. O. Muvianto, and S. Ariessaputra, “DESAIN MODIFIKASI CANTENNA UNTUK OPTIMASI FEED ANTENA GRID 2 . 4 GHz,” *J. Bakti Nusa*, vol. 1, no. 2, pp. 49–57, 2020.

[12] A. Aoad, “Design and manufacture of a multiband rectangular spiral-shaped microstrip antenna using EM-driven and machine learning,” *Elektron. ir Elektrotechnika*, vol. 27, no. 1, pp. 29–40, 2021.

JURNAL ECOTIPE
Electronic, Control, Telecommunication, Information, and Power Engineering
Volume 11, Issue 1, April 2024, pp. 66-76
ISSN 2355-5068 ; e-ISSN 2622-4852
DOI: 10.33019/jurnalecotipe.v11i1.4487

Performance Evaluation of Overcurrent Relay and Ground Fault Relay Coordination in Distribution Feeder

Azriyenni Azhari Zakri[1], Rezky Almi Ramadhan[2], Wahri Sunanda[3]
[1,2] Department of Electrical Engineering, Universitas Riau
Kampus Bina Widya, Jl. H. R. Soebrantas Km 12,5 Simpang Baru Panam, Pekanbaru, 28293
[3] Department of Electrical Engineering, Universitas Bangka Belitung
Kampus Terpadu Balunijuk, Bangka, 33172

ARTICLE INFO

Article historys:

Received : 02/02/2024
Revised : 07/02/2024
Accepted : 01/04/2024

Keywords:

OCR; GFR; Protection; Reliability

ABSTRACT

Reliable and sustainable electrical distribution systems require effective protection measures against internal and external disturbances, especially short-circuit disturbances, to avoid damage to the equipment. Overcurrent relays (OCR) and ground fault relays (GFR) play an important role in the safety of the distribution network. To improve performance, evaluation of relay coordination is essential. During the short circuit, the nearest relay to the fault point is activated first and the backup relay is activated if the fault current exceeds the adjustment of the main relay. Coordination ensures that timely signaling is sent to interrupt the circuit. Inspection of the OCR relay revealed that it did not comply with the IEC 60255 standard and consequently adjusted the classification time to 0.402 seconds. Similarly, the results of the GFR relay inspection did not meet the standards and required an adjustment of the evaluation time to 0.492 seconds. Resolving these deviations is crucial to maintaining the reliability and compliance of the distribution network with industry standards, ensuring that the protection relays respond quickly and effectively to disturbances, thereby preventing possible damage to equipment.

Corresponding Author:

Azriyenni Azhari Zakri
Department of Electrical Engineering, Universitas Riau
Kampus Bina Widya, Jl. H. R. Soebrantas Km 12,5 Simpang Baru Panam, Pekanbaru, 28293
Email: azriyenni@eng.unri.ac.id

1. INTRODUCTION

The electricity system must be reliable and capable of meeting the electricity demand constantly [1]. One of the supports is a good protection system. Protection systems are a means of preventing or limiting damage caused by interference [3] to devices and ensuring the continuity of electrical distribution in substations [2]. Almost all electrical circuit failures in the electrical distribution system are short circuit failures. If not removed immediately, the equipment will damage itself. Short circuit failures in substations are three-phase failures, two-phase failures, and single-phase ground failures [3]. Protection relays are used to overcome disturbances in the distribution system. Protection relays are electrical equipment designed to separate parts of the electrical system when there are disturbances in the system. In order to achieve high system reliability, safety relays with good selective capabilities are required, as rapid and precise safety measures will minimize the isolation of disturbances. The most used protection relays are the overcurrent relay (OCR) and ground fault relay (GFR). These two protection devices are installed on the input and output sides of the substation; therefore, the relay coordination on the input and output sides must be maintained, as the coordination between the relays determines the reliability of the protection system [6-7].

The setting of the OCR on the self-serving power distribution network was determined by determining the value of the adjustment of the current and time multiplier (TMS) of each OCR on the network. Under existing conditions, if the nearest OCR fails to function when interference occurs, it does not meet the protection coordination requirements. There was an OCR with a time classification and an overlapping coordination curve. This configuration is required so that the nearby OCR can work without interference. When the primary relay failed and no overhang curve was found, backup protection was implemented in a coordinated sequence. The time classification was based on the IEEE 242-1986 standard [8], which was 0.2-0.4 seconds [6]. The ground fault relay is a protection relay that is used to detect and protect ground faults, especially those involved in one or two phases. It works by preventing the electricity network from being interrupted by problems between phases or three phases and operates in a single direction. The relay is usually installed on high- and medium-voltage systems, including safety transformers, to ensure the protection of electrical equipment in the event of ground-phase faults [5].

Current differential protection schemes apply to medium voltage distribution systems to maintain as much energy as possible for loads and distribution units during defects [3]. Differential relays of the conventional two-terminal current percentage are used to form sequential time-current coordinated differential protection zones. Several times, different elements in each protection zone are delayed, which guarantees coordination with adjacent protection equipment of the area, and continuity between different protection zones [9].

In the context of a comprehensive evaluation of the protection mechanisms, the integration of the AC microgrid into the distribution network can provide insight into the dynamics of the interaction of the microgrid and contribute to improving the protection system of the distribution network [10]. Changes in the layout of the distribution network can have a significant impact on coordination and protection measures. To modernize the microgrid protection system, various protection strategies have been proposed, including DC/AC systems, communication frameworks, synchronized machines, and distributed generation based on inverters (IBDGs). These microgrids are classified as integral components of the overall protection framework.

Conventional overcurrent protection techniques in generator-assisted distribution networks can impede relay coordination, resulting in lower network reliability [11]. To address this problem, protective coordination strategies using double direction closure (DSDR) have been developed to improve the effectiveness of fuse storage systems. These DSDR protection strategies allow network operators to achieve flexible coordination coverage and precise protection settings according to coordination requirements. The effectiveness of the proposed protection system has been confirmed by standard IEEE systems and comparative analysis. Furthermore, the document emphasizes the economic aspects of designing protection strategies that involve fewer protective devices [12].

The superconducting fault current limiter (SFCL) causes a delay in OCR operation due to minimal error currents and has a negative impact on the coordination of energy distribution network protection systems [13]. These delays in the OCR pathway prolong the exposure time of neighboring power plants to asymmetric fault currents. In the case of asymmetric ground faults, the OCR index is used to compensate for barriers introduced by SFCL. The recommended OCR index contains all resistance components derived from the voltage and current measured in the distribution system and the SFCL [14]. To demonstrate the effectiveness of this algorithm, simulations were performed using power system computer aided design (PSCAD) to analyze the protective coordination between OCR and SFCL in the electricity distribution system [15].

In order to address the growing current failures in power distribution systems caused by the interconnected operation of high-capacity generators, superconductor fault current limiters are being investigated as protection devices [16]. This integration into the electrical distribution system can lead to malfunction or non-operation of protection relays and interfere with their coordination. To evaluate the operation of fault current limiters and coordinate protection between OCRs and network distribution circuit voltage components, overcurrent voltage relays are used. PSCAD simulations are used to examine the optimization of the proportional voltage coefficient of the OCR voltage component, with the aim of improving the protection coordination between the OCR [17].

Modern electricity networks require flexible energy use, but high energy penetration rates are the common source of wind and solar power, and this presents a challenge [18]. The network plays an essential role in the development of robust and sustainable electricity systems, especially in high intermittent renewable energy. To overcome these complex problems, and especially to increase energy production, public utilities and consumers must strictly demand distribution systems [19].

In order to ensure effective coordination of the protection relays, the closest relay to the source of disturbance is activated, and a circuit breaker trip command is issued when the electrical system encounters a problem. If the main relay is susceptible to interference or malfunction, the second relay or the backup relay will start to run. Evaluation of the coordination of installed protection relays is essential to maintain and improve the performance of the protection system.

2. RESEARCH METHOD

The protection system is a way to prevent or limit damage caused to electrical equipment due to interference to ensure the continuity of the electrical distribution [19]. Protection relays are electrical devices that detect disturbances in electrical systems. When the relay feels a disturbance, it automatically disconnects the circuit breaker and commands it to separate the affected part of the system. A protection relay is an OCR and GFR [21][22].

An overcurrent relay, or better known as an OCR, is a piece of equipment that detects overcurrent, which is caused by a short circuit between phases that can damage the electrical system equipment within its security area [12]. To adjust the OCR current value, equation (1) is:

$$I_{setOCR\,(feeder)} = 1.1\; x\; I_{load} \tag{1}$$

The setting on the side of the *incoming*, equation (2) is:

$$I_{setOCR\,(incoming)} = 1.2\; x\; I_{nominal} \tag{2}$$

Ground fault relay (GFR) basically has the same working principle as OCR but has differences in its use. If OCR detects a short-circuit current between phases, then GFR detects a short-circuit current from one phase to ground [6]. Setting the GFR current on the feeder side of equation (3) is:

$$I_{setGFR\,(feeder)} = 0.1\; x\; I_{load} \tag{3}$$

On the side of *incoming*, equation (4) is:

$$I_{setGFR\,(incoming)} = 0.1\; x\; I_{nominal\;trafo} \tag{4}$$

Time-Multiple Setting (TMS) is a time-multiple variable value used for setting protective relays. Inverse relays can be differentiated according to their working time characteristics [21] according to the IEC standard [23].

The protection system, which is placed sequentially along the distribution line, is arranged in such a way that it will work at a time grading according to the location of the protection relay against disturbances. Relays closest to the fault will operate faster than relays farther away. Meanwhile, if the relay does not work, the relay behind it will work longer. To determine the source impedance (Z_s) on the primary side, equation (5) is as follows.

$$Z_{s\,(primary)} = \frac{{kV_{L-L\,(primary)}}^2}{MVA_{SC}} \tag{5}$$

$Z_{s\ (primary)}$ is the source impedance on the primary side (Ω), kV $_{L\text{-}L}$ (primary) is the phase-to-phase voltage on the primary side (kV), MVA_{sc} is the current capacity when a fault occurs.

To determine the source impedance value on the secondary side, equation (6) is:

$$Z_{s\,(secondary)} = Z_{s\,(primary)}\; x\; \frac{{kV_{L-L\,(secondary)}}^2}{{kV_{L-L\,(primary)}}^2} \tag{6}$$

$Z_{s\ (secondary)}$ is the source impedance on the secondary side (Ω), $Z_{s\ (primary)}$ is the source impedance on the primary side (Ω), $Z_{s\ (secondary)}$ is the source impedance on the secondary side (Ω), $Z_{s\ (primary)}$ is the source impedance on the primary side (Ω), kV$_{L\text{-}L\ (secondary)}$ is the phase-to-phase voltage on the secondary side (kV), kV$_{L\text{-}L\ (primary)}$ is the phase-to-phase voltage on the primary side (kV).

When calculating the impedance of a transformer, the reactance value is taken, while the resistance is ignored because it is small. The following is how to find the impedance values for a positive sequence, a negative sequence, and a zero sequence. To calculate the positive and negative sequence impedance of a transformer, equation (7) is as follows:

$$Z_{t1} = Z_{t2} = \%Z\ x\ \frac{kV_{L-L}{}^{2}}{MVA} \tag{7}$$

Z_{t1} is the positive sequence impedance of the transformer (Ω), Z_{t2} is the negative sequence impedance of the transformer (Ω), %Z is the percentage of transformer impedance (%), kV$_{L\text{-}L}$ = phase-to-phase voltage (kV), MVA = power transformer capacity (MVA). To calculate the zero sequence impedance of a transformer (Z_{t0}) the equation (8) is as follows:

$$Z_{t0} = 3\ x\ Z_{t1} \tag{8}$$

Where:
Z_{t0} = Transformer zero sequence impedance (Ω)

Feeder impedance is divided into positive sequence, negative sequence, and zero sequence impedance. To calculate the positive and negative sequence impedance values of the feeder, equation (9) is:

$$Z_{L1} = Z_{L2} = Z_{1\,conductor}\ x\ l \tag{9}$$

ZL_1 is the impedance of the positive sequence feeder (Ω), Z_{L2} is the impedance of the negative sequence feeder (Ω), Z_1 The conductor is the impedance of the positive sequence feeder wire (Ω/km), l is the length of the channel (km). To calculate the zero sequence impedance value of the feeder, equation (10) is:

$$Z_{L0} = Z_{0\,conductor}\ x\ l \tag{10}$$

Z_{L0} is the zero-sequence impedance of the feeder (Ω), Z_0 conductor is the zero-sequence impedance of the feeder wire (Ω/km).

To calculate the equivalent positive sequence and negative sequence impedance, equation (11) is:

$$Z_1 = Z_2 = Z_s + Z_{t1} + Z_{L1} \tag{11}$$

Z_1 is the equivalent positive sequence impedance (Ω), Z_2 is the equivalent negative sequence impedance (Ω), Zs is the source impedance (Ω), Z_{t1} is the positive sequence impedance of the transformer (Ω), Z_{L1} is the positive sequence impedance of the feeder (Ω).

To calculate the zero sequence equivalent impedance, equation (12) is:

$$Z_0 = 3R_N + Z_{t0} + Z_{L0} \tag{12}$$

Z_0 = Equivalent zero sequence impedance (Ω), RN = soil resistance (Ω), Z_{t0} = Transformer zero sequence impedance (Ω), Z_{L0} = feeder zero sequence impedance (Ω).

To obtain the value of the three-phase short circuit fault current, equation (13) is:

$$I_{f,3\phi} = \frac{V_{L-N}}{Z_1} \tag{13}$$

$I_{f,3\phi}$ is the three-phase short circuit fault current (A), V_{L-N} is the phase to neutral voltage (V), Z_1 is the positive sequence impedance (Ω). To obtain the value of the two-phase short circuit fault current, equation (14) is:

$$I_{f,L-L} = \frac{V_{L-L}}{Z_1+Z_2} \tag{14}$$

$I_{f,L-L}$ is the two-phase short circuit fault current (A), V_{L-L} is the phase-to-phase voltage (V), Z_1 is the positive sequence impedance (Ω), Z_2 is the negative sequence impedance (Ω). To obtain the value of the single phase short-circuit fault current to ground, equation (15) is:

Volume 11, Issue 1, April 2024, pp. 66-76
ISSN 2355-5068 ; e-ISSN 2622-4852
DOI: 10.33019/jurnalecotipe.v11i1.4487

$$I_{f,L-G} = \frac{3\ x\ V_{L-N}}{Z_1+Z_2+Z_0} \tag{15}$$

$I_{f,L-G}$ is the single phase short circuit fault current to ground (A), V_{L-N} is the phase to neutral voltage (V), Z_1 is the positive sequence impedance (Ω), Z_2 is the negative sequence impedance (Ω), Z_0 is zero sequence impedance (Ω).

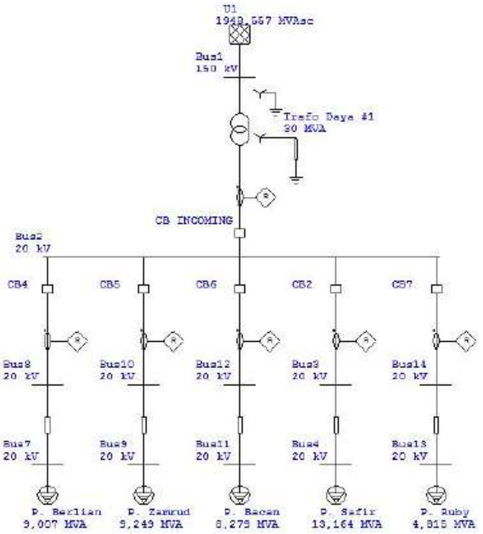

Figure 1. Diagram feeder of PK substation

Figure 1 is a single line diagram of the PK substation using the ETAP 12.6.0 programme to run simulations of short circuit faults and relay coordination. The data entered are the reset data. The results of the relay simulation are then compared with the relay data installed in the field.

Table 1. Over current relay

Incoming side		**Feeder side**	
Brand	Schneider	Brand	Schneider
Type	P142	Type	P142
Curve	IEC-*Standard Inverse*	Curve	IEC-*Standard Inverse*
CT ratio	1000: 1	CT ratio	400: 5
I_{set} (A)	1000	I_{set} (A)	352
I_{relay} (A)	1	I_{relay} (A)	4.4
TMS	0.22	TMS	0.13

Table 2. Ground fault relay

Incoming side		**Feeder side**	
Brand	Schneider	Brand	Schneider
Type	P142	Type	P142
Curve	IEC-*Standard Inverse*	Curve	IEC-*Standard Inverse*
CT ratio	1000: 1	CT ratio	400: 5
I_{set} (A)	100	I_{set} (A)	32
I_{relay} (A)	0.1	I_{relay}(A)	0.4
TMS	0.23	TMS	0.12

The evaluation of the coordination of OCR and GFR in the PK substation is by collecting data from the substation, transformer data, load data, feeder line data and relay data. The data in table 1 and table 2 will be used to calculate the equivalent impedance, short-circuit current, and TMS. Technical data on installed equipment includes installed power under three-phase short circuit conditions is 1948.557 MVA at a nominal voltage of 150 kV, power transformer capacity is 30 MVA, voltage on the secondary side is 20 kV at a nominal current of 866.02 ampere. The type of conductor used is AAAC with a size of 240 mm2, positive and negative sequence impedance 0.1344+j 0.3158 Ω/km, and a zero-sequence impedance 0.2824+j1.6034 Ω/km.

3. RESULTS AND DISCUSSION

Short-circuit fault current calculations and OCR and GFR resetting are carried out. After that, a short circuit fault simulation will be performed, a relay coordination simulation, and the OCR and GFR curves will be displayed on the incoming and feeder sides. The simulation results before and after the reset will be compared. Using equation (5), the source impedance (Z_s) is as follows:

$$Z_{s\,(primary)} = 11.55\,\Omega$$

To convert the impedance on the primary side to the secondary side using equation (6), then:

$$Z_{s\,(secondary)} = 0.205\,\Omega$$

The positive and negative sequence impedance values of the transformer are obtained using equation (7):

$$Z_{t1} = Z_{t2} = 1.66\,\Omega$$

The transformer has a YY(d) winding connection which has a delta winding in it, the magnitude of Z_{t0} is three times the positive sequence impedance of the transformer. So, by using Equation (8) we have the following.

$$Z_{t0} = 3\ x\ 1.66 = 4.98\,\Omega$$

The feeder chosen as a reference is a sapphire feeder. The positive sequence, negative sequence, and zero sequence impedances of the feeder are calculated using equation (9) and (10):

$$\begin{aligned} Z_1 = Z_2 &= (0.1344 + j0.3158)\ x\ 64 \\ &= 8.6016 + j20.2112\,\Omega \\ Z_0 &= (0.2824 + j1.6034)\ x\ 64 \\ &= 18.0736 + j102.6176\,\Omega \end{aligned}$$

The feeder impedance values for fault locations with a distance of 0% and 100% of the feeder length in positive sequence and negative sequence are as follows:

$$\begin{aligned} Z_{1(0\%)} &= 0 \\ Z_{1(100\%)} &= 100\%\ x\ (8.6016 + j20.2112) \\ &= 8.6016 + j20.2112\,\Omega \end{aligned}$$

The feeder impedance values for fault locations with a distance of 0% and 100% of the zero-sequence feeder length are as follows:

$$\begin{aligned} Z_{0(0\%)} &= 0 \\ Z_{0(100\%)} &= 100\%\ x\ (18.0736 + j102.6176) \\ &= 18.0736 + j102.6176\,\Omega \end{aligned}$$

The equivalent impedance is calculated by adding the source impedance on the 20 kV side, the transformer impedance, and the feeder impedance. Equation (11) is used to calculate the equivalent impedance of positive sequence and negative sequence:

$$\begin{aligned} Z_{1(0\%)} &= j1.865 + 0 = j1.865\,\Omega \\ Z_{1(100\%)} &= j1.865 + 8.6016 + j20.2112 \end{aligned}$$

$$= 8.6016 + j22.0762\,\Omega$$

Equation (12) is used to calculate the equivalent impedance of the zero sequence:

$$Z_{0(0\%)} = 120 + j4.98 + 0 = 120 + j4.98\,\Omega$$
$$Z_{0(100\%)} = 120 + j4.98 + 18.073 + j102.6176$$
$$= 138.0736 + j107.5976\,\Omega$$

If the equivalent impedance value according to the fault location has been obtained, then the next step is to calculate the short-circuit fault current. The three-phase short circuit fault current is calculated using equation (13):

$$I_{f,3\phi(0\%)} = 6.191.42\ A$$
$$I_{f,3\phi(100\%)} = 487.36\ A$$

The two-phase short circuit fault current is calculated using equation (14):

$$I_{f,L-L(0\%)} = 5.361.93\ A$$
$$I_{f,L-L(100\%)} = 422.07\ A$$

Single phase short circuit fault current to ground is calculated using equation (15):

$$I_{f,L-G(0\%)} = 279.74\ A$$
$$I_{f,L-G(100\%)} = 155.73\ A$$

Feeder side OCR current adjustment

$$I_{set} = 418\ A$$

The TMS OCR setting on the feeder side at the specified working time (t) is 0.3 seconds.

$$0.3 = \frac{0.14}{\left(\frac{6.260}{418}\right)^{0.02} - 1}\ x\ TMS$$
$$TMS = 0.12$$

Adjustment of feeder side GFR current;

$$I_{set} = 38\ A$$

The specified working time (t) is 0.5 seconds;

$$0.5 = \frac{0.14}{\left(\frac{287}{38}\right)^{0.02} - 1}\ x\ TMS$$
$$TMS = 0.15$$

Incoming side OCR current adjustment;

$$I_{set} = 1.2\ x\ 866.02 = 1.039.224\ A$$

The TMS OCR setting of the incoming side at the specified working time (t) is 0.3 + 0.4 seconds.

$$0.7 = \frac{0.14}{\left(\frac{6,260}{1.039.224}\right)^{0.02} - 1}\ x\ TMS$$
$$TMS = 0.184$$

Adjusting the incoming side GFR current;

$$I_{set} = 0.1\ x\ 866.02 = 86.6\ A$$

The working time (t) set is 1 second;

$$1 = \frac{0.14}{\left(\frac{287}{86.6}\right)^{0.02} - 1}\, x\, TMS$$

$$TMS = 0.173$$

Figure 2 (a) simulates the coordination of OCR in three-phase short circuits. The relay sequence is that relay 2 sends a signal to CB 2 to drive, and relay 1 sends a signal to CB 2. Figure 2 (b) is the OCR working time coordination curve of the input and output sides of the three-phase short circuit when a short circuit error occurs. The work time of the second relay is 0.302 seconds, and the first relay is 0.704 seconds. Therefore, we get a time of 0.402 seconds.

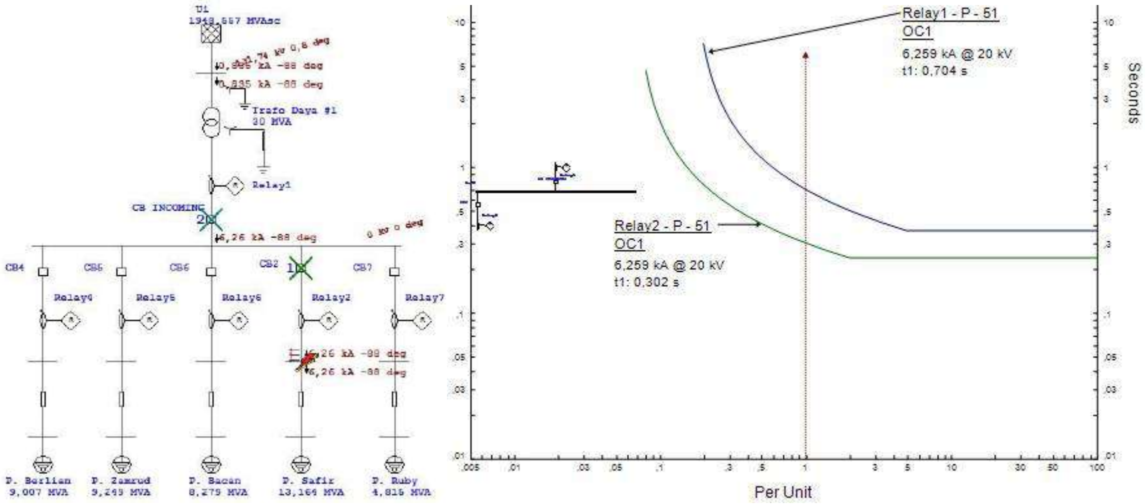

(a) (b)

Figure 2. (a) Simulation of OCR coordination when three phase faults; (b) Time coordination curve

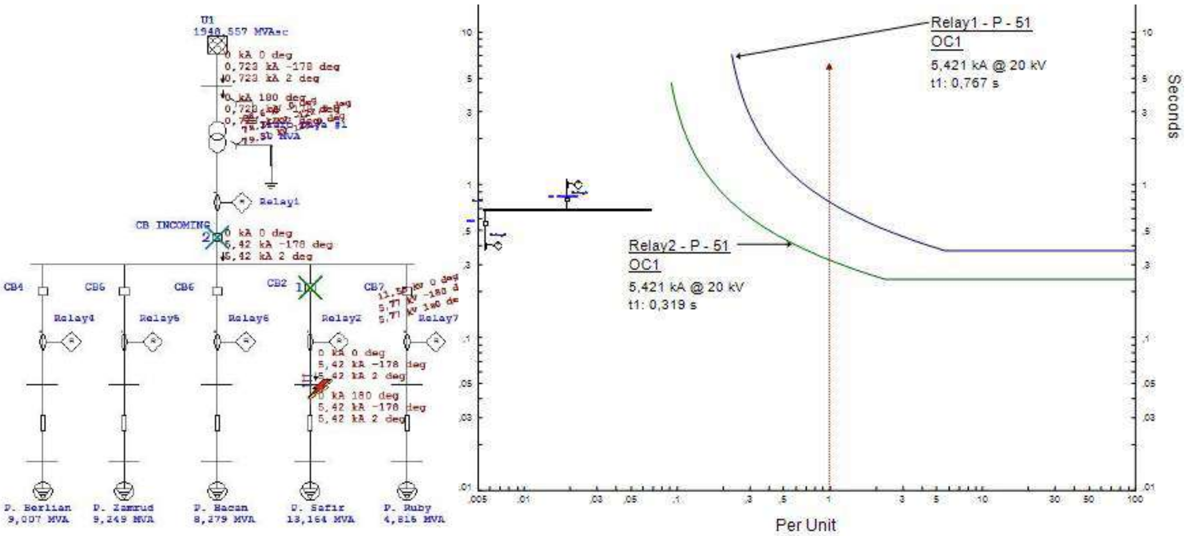

(a) (b)

Figure 3. (a) OCR coordination simulation when phase-to-phase fault (b) time coordination curve

Figure 3 (a) is a simulation of OCR coordination when a two-phase short circuit occurs. The relay sequence that works is that relay 2 gives a signal to CB 2 to trip, then relay 1 gives a signal to the incoming CB to trip. Figure 3 (b) is the OCR working time coordination curve of the input and output sides of the feeder when a two-phase short circuit malfunction occurs. The working time of relay 2 was 0.319 seconds, while relay 1 was 0.767 seconds. Therefore, the time rating value is 0.448 seconds.

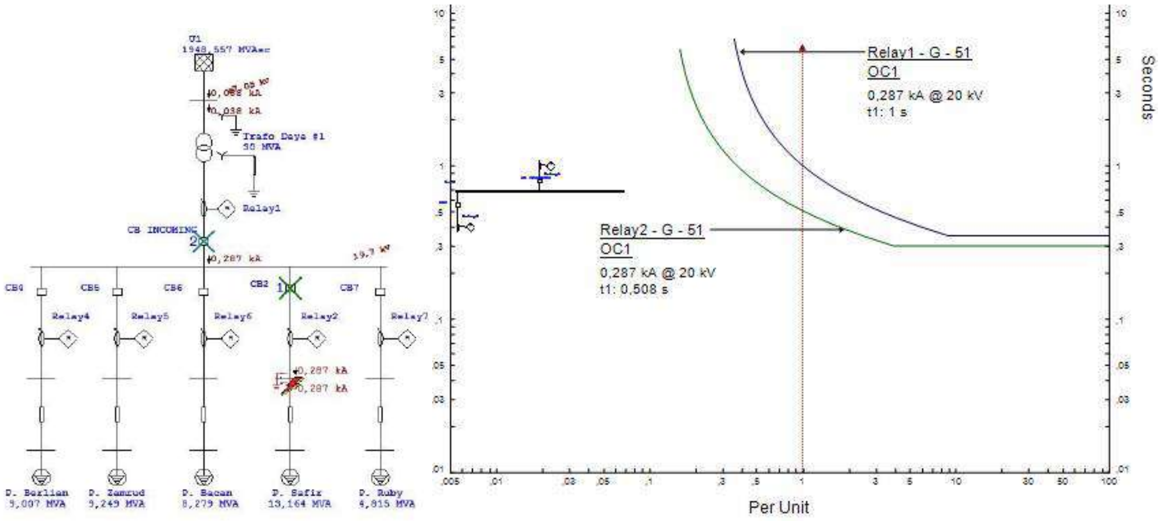

(a) (b)

Figure 4. (a) GFR coordination simulation when single phase ground fault (b) Time coordination curve

Figure 4 (a) is a simulation of GFR coordination when a single-phase short circuit to the ground occurs. The relay sequence that works is that relay 2 gives a signal to CB 2 to trip, then relay 1 gives a signal to the incoming CB to trip. Figure 4 (b) is the GFR working time coordination curve on the feeder side and on the incoming side when a single phase short circuit to ground fault occurs. The working time of relay 2 is 0.508 seconds and relay 1 is 1 second. Therefore, we get a time-grading value of 0.492 seconds. It can be concluded that after resetting the relay has a time grading that complies with IEC 60255 [24], which is 0.4 - 0.5 seconds. The installed relay also works according to its settings. When the short circuit fails, the closest relay will be activated. If the magnitude of the current failure exceeds the subsequent configuration of the backup relay, the backup relay will respond within the specified time parameters according to the recommendations of IEC 60255.

4. CONCLUSION

Analysis of short-circuit failure simulations shows that the farther away the failure point is from the power source, the lower the corresponding fault current. In contrast, when the fault point is closer to the power source, the current value of the fault is higher. As the existing OCR time classification does not meet the IEC 60255 standards, adjustments are made. The evaluation results show that OCR's work time on the top of the entry is 0.704 seconds, and the working time on the top of the feeder is 0.302 seconds. The time distribution between the OCRs complies with IEC 60255 standards in the range of 0.402 seconds. The GFR time classification under current conditions also does not comply with the IEC 60255 standards, so the GFR has been redesigned to make the GFR working time 1 second from the source and 0.508 seconds from the source. The calculation time between GFR is strictly in accordance with IEC 60255 standards, which is 0.492 seconds. Finally, after evaluating the coordination of the OCR and GFR protection relays in the distribution feeder, the relays were adjusted to IEC standards to improve the protection device performance. Future research could study the optimization techniques of OCR and GFR relay coordination to improve performance according to existing standards.

REFERENCES

[1] K. A. Mamun and F. R. Islam, "Reliability evaluation of power network: A case study of Fiji Islands," *in 2016 Australasian Universities Power Engineering Conference (AUPEC)*, 2016, pp. 1-6, doi: 10.1109/aupec.2016.7749359.

[2] A. G. Phadke, P. Wall, L. Ding, and V. Terzija, "Improving the performance of power system protection using wide area monitoring systems," *Journal of Modern Power Systems and Clean Energy*, vol. 4, no. 3, pp. 319-331, 2016, doi: 10.1007/s40565-016-0211-x.

[3] C. Ye, C. Guo, and Y. Ding, "Risk Evaluation of Short-Circuit Fault in Power System," *in Risk-Based Planning and Operation Strategy Towards Short Circuit Resilient Power Systems*, 2023, pp. 1-15, doi: 10.1007/978-981-19-9725-9_1.

[4] L. Sugesti, A. N. Afandi, and H. Putranto, "Setting Analysis of Over Current Relay and Ground Fault Relay on Transformer Protection System of High Voltage Substation System," *in 2018 Electrical Power, Electronics, Communications, Controls and Informatics Seminar (EECCIS)*, 2018, pp. 1-6, doi: 10.1109/eeccis.2018.8692825.

[5] S. Zaibah, A. T. Nugraha, and F. H. Ainudin, "Planning a Protection Coordination System Against Over Current Relays and Ground Fault Relays Using the NN Method," *Journal of Electronics, Electromedical Engineering, and Medical Informatics*, vol. 4, no. 4, 2022, doi: 10.35882/jeeemi.v4i4.239.

[6] S.-T. Lim and S.-H. Lim, "Analysis on Protective Coordination between Over-Current Relays with Voltage Component in a Power Distribution System with SFCL," *IEEE Transactions on Applied Superconductivity*, vol. 30, no. 4, pp. 1-6, 2020, doi: 10.1109/tasc.2020.2968252.

[7] V. C. Nikolaidis, G. Michaloudis, A. M. Tsimtsios, D. Tzelepis, and C. D. Booth, “A multi-zone differential protection scheme for MV distribution systems with distributed generation,” *15th International Conference on Developments in Power System Protection (DPSP 2020)*, 2020, doi: 10.1049/cp.2020.0071.

[8] IEEE, "IEEE Recommended Practice for Protection and Coordination of Industrial and Commercial Power Systems," *ANSI/IEEE Std 242-1986*, 1986, pp. 1-592, doi: 10.1109/IEEESTD.1986.81071.

[9] V. Patel and V. Patel, "A comprehensive review: AC & DC Microgrid Protection," *in 2020 21st National Power Systems Conference (NPSC)*, 2020, doi: 10.1109/npsc49263.2020.9331932.

[10] W. M. Hamanah, M. I. Hossain, M. Shafiullah, and M. A. Abido, “AC Microgrid Protection Schemes: A Comprehensive Review,” IEEE Access, vol. 11, pp. 76842–76868, 2023, doi: 10.1109/access.2023.3298306.

[11] A. Arafa, M. M. Aly, and S. Kamel, "Impact of Distributed Generation on Recloser-Fuse Coordination of Radial Distribution Networks," *in 2019 International Conference on Innovative Trends in Computer Engineering (ITCE)*, 2019, doi: 10.1109/itce.2019.8646557.

[12] M. Yousaf, A. Jalilian, K. M. Muttaqi, and D. Sutanto, "An Adaptive Overcurrent Protection Scheme for Dual-Setting Directional Recloser and Fuse Coordination in Unbalanced Distribution Networks with Distributed Generation," *IEEE Transactions on Industry Applications*, vol. 58, no. 2, pp. 1831-1842, 2022, doi: 10.1109/tia.2022.3146095.

[13] Y. J. Cho and S.-H. Lim, "Analysis on Protection Coordination of OCRs Using Index for Impedance Compensation Considering Unsymmetrical Ground Fault in a Power Distribution System With SFCL," *IEEE Transactions on Applied Superconductivity*, vol. 33, no. 5, pp. 1-6, 2023, doi: 10.1109/tasc.2023.3262765.

[14] M. U. M. Rao, D. S. N. M. Rao, and C. S. R. Reddy, "Protection of microgrids using Resistive Type Superconducting Fault Current limiter (RSFCL)," *in 2022 IEEE 2nd International Conference on Sustainable Energy and Future Electric Transportation (SeFeT)*, 2022, doi: 10.1109/sefet55524.2022.9909066.

[15] Y.-J. Cho, M.-K. Park, and S.-H. Lim, "Analysis on Operation Characteristics of OCR Using Impedance Compensation Algorithm Considering Application of SFCL in a Power Distribution

System," *The Transactions of The Korean Institute of Electrical Engineers*, vol. 70, no. 11, pp. 1670-1676, 2021, doi: 10.5370/kiee.2021.70.11.1670.

[16] F. Blaabjerg, Y. Yang, D. Yang, and X. Wang, “Distributed Power-Generation Systems and Protection,” *Proceedings of the IEEE*, vol. 105, no. 7, pp. 1311–1331, 2017, doi: 10.1109/jproc.2017.2696878.

[17] C. Guo, Z. Cai, Y. Zhang, P. Xie, K. Liu, and Y. Li, “Operation Condition Assessment Method and its Practical Implementation for Protection Systems,” *IEEE Access*, vol. 7, pp. 51771–51781, 2019, doi: 10.1109/access.2019.2911973.

[18] V. Telukunta, J. Pradhan, A. Agrawal, M. Singh, S.G. Srivani, "Protection challenges under bulk penetration of renewable energy resources in power systems: A review," *CSEE Journal of Power and Energy Systems*, vol. 3, no. 4, pp. 365-379, 2017, doi: 10.17775/cseejpes.2017.00030.

[19] M. Saifudin, S. Suryono, and I. Irianto, "Monitoring and Protection System for Overvoltage, Undervoltage and Unbalance Voltage," *Jurnal Ecotipe (Electronic, Control, Telecommunication, Information, and Power Engineering)*, vol. 9, no. 2, pp. 159-165, 2022, doi: 10.33019/jurnalecotipe. v9i2.3092.

[20] R. Nugrahadi, W. Sunanda, Asmar, R. F. Gusa, and I. Dinata, “Design of voltage regulator for photovoltaic and wind hybrid power plant based on microcontroller,” *AIP Conference Proceedings*, 2019, doi: 10.1063/1.5098250.

[21] M. Bamber, "Network Protection and Application Guide: Protective Relays, Measurement and Control," *Alstom Grid*, Paris, 2011.

[22] H. Prasetijo, A. Fadli, W. H. Purnomo, and Priswanto, "Working time coordination of over current relay (OCR) and ground fault relay (GFR) in 20 kV feeder distribution," *AIP Conference Proceedings*, doi: 10.1063/5.0113957.

[23] T. Penthong, M. Ginocchi, A. Ahmadifar, F. Ponci, and A. Monti, “IEC 61850-Based Protection Scheme for Multiple Feeder Faults and Hardware-in-the-Loop Platform for Interoperability Testing,” *IEEE Access*, vol. 11, pp. 65181–65196, 2023, doi: 10.1109/access.2023.3280128.

[24] IEC, "Measuring relays and protection equipment-Part 151: Functional requirements of over/under current protection," *IEC 60255-151*, 2009.

JURNAL ECOTIPE
Electronic, Control, Telecommunication, Information, and Power Engineering

Volume 11, Issue 1, April 2024, pp. 77-87
ISSN 2355-5068 ; e-ISSN 2622-4852
DOI: 10.33019/jurnalecotipe.v11i1.4488

Comparasion of HVAC Energy Consumption Prediction in an Academic Building using LSTM and DNN

Hadi Christian[1], Koko Friansa[2], Justin Pradipta[3], Irsyad Nashirul Haq[4], Edi Leksono[5]
[1,2,3,4,5] Engineering Physics Department, Bandung Institute of Technology, Bandung 40132, Indonesia

ARTICLE INFO

Article historys:

Received : 16/02/2024
Revised : 27/03/2024
Accepted : 01/04/2024

Keywords:

Long Short-Term Memory (LSTM); Deep Neural Network (DNN); Accuracy Metrics; Heating, Ventilation, and Air Conditioning (HVAC); Energy Consumption Prediction

ABSTRACT

Energy consumption information is a collection of information obtained from datasets that is useful for making decisions for energy conservation. In this paper, we proposed a modern approach based on LSTM and DNN. While many researchers have employed these methods for predicting energy consumption of HVAC, this paper seeks to compare their efficacy to determine which is superior. The comparative analysis in question employs accuracy metrics such as Mean Absolute Error (MAE), Mean Squared Error (MSE), Root Mean Squared Error (RMSE), and R-squared (R^2) values. Furthermore, the accuracy metric outcomes indicate that the LSTM method surpasses the DNN approach in terms of the R-squared (R^2) value, with respective scores of 0.941 and 0.782. Meanwhile, for other accuracy metrics, the DNN method outperforms LSTM. Nevertheless, the performance of the two proposed methods is excellent, as evidenced by the R-squared (R^2) value exceeding 0.75, which aligns with modeling standards observed in numerous research studies.

Corresponding Author:

Justin Pradipta
Engineering Physics Department, Bandung Institute of Technology, Bandung 40132, Indonesia
Email: justinpradipta@itb.ac.id

1. INTRODUCTION

Global warming has become an important problem which is largely influenced by increasing concentrations of CO2 dioxide carbon emissions in the air. CO2 emissions are caused by excessive energy use, especially in academia, recidential and commercial buildings [1,2]. Approximately 36% of the world's energy consumption and 38% of carbon emissions can be attributed to the building sector [3]. In Indonesia, a commitment has been made to achieve a 29% reduction in carbon emissions by 2030, employing measures focused on energy conservation. Additionally, there is a specified target to attain 23% utilization of new renewable energy by the year 2025. Considering the current condition and a goal to achieve carbon reduction and energy conservation by 2030, we are faced with the formidable challenge of diminishing building energy consumption and mitigating building carbon emissions [4]. The largest energy consumption in building systems is the HVAC (Heating, Ventilation, and Air Conditioning) system with approximately 40-60% according to the type of building [5], this is the focus of researchers in making efforts to increase building energy efficiency [6]. Many studies related to energy management systems in building have been carried out espicially in HVAC system [7-9].

The forecasting of building energy holds significant importance in the realms of energy saving by planning, management, and conservation. This is crucial as it facilitates the provision of precise solutions for demand response on the supply side [10,11]. The utilization of machine learning methods to the control and optimization of HVAC systems is emerging massively in the current era. Many studies show that machine learnig is used to prediction, which this method can be classified into white-box, black-box, and grey-box approaches [12,13]. Simplify, In the realm of predicting building energy consumption, black box models prove more adept at swiftly generating accurate forecasts compared to grey and white box models. Analyzing and mining extensive datasets within black-box models allows for bypassing the impact of real assumptions on predictions especially in electricity energy consumption load [14]. Black-box models can be sub-divided into non-deep learning and deep learning models [15].

Deep learning models possess the ability to comprehend intricate nonlinear connections, exhibit outstanding predictive precision, and are especially beneficial for scrutinizing extensive datasets related to building energy. They proficiently grasp prolonged dependencies and temporal dynamics, thereby enhancing the accuracy of predictions, particularly in the context of time-series forecasts. Common deep learning models encompass Artificial Neural Networks (ANN), Deep Neural Networks (DNN), recurrent neural networks (RNN), Long Short-Term Memory (LSTM), and gate recurrent units (GRU). Das et al. [16] employed a Long Short-Term Memory (LSTM) model for forecasting electricity consumption in residential environments. This was done to comprehend the usage patterns of residents and offer energy management solutions aimed at optimizing electricity utilization. Salam and El Hibaoui. [17] proposed a hybrid model, incorporating both neural network and Long Short-Term Memory (LSTM), which was developed with the aim of constructing effective models for predicting electricity consumption.

As we know, the LSTM neural network constitutes a type of recurrent neural network, featuring LSTM cells employed as hidden layers. The recurrent neural network (RNN) incorporates the notion of time series into its network structure design, enhancing its adaptability in the analysis of time series data. Additionally, the long short-term memory (LSTM) neural network addresses issues such as gradient disappearance, gradient burst, and inadequate long-term memory capacity observed in RNN. This enables LSTM to effectively utilize long-distance time information [18,19]. This neural network is widely using and successful outcomes have been attained in the prediction of building energy consumption. [20, 21]. While, the utilization of the deep neural network (DNN), a widely embraced artificial intelligence model, has been prevalent in various prior studies to create surrogate models, leading to notable success. In recent years, much research in DNN models has been developed in various energy applications such as prediction of HVAC energy consumption in a residential dormitory through the application of Deep Neural Network by opening window impact [22]. Alcántara et al. [23] deployed DNN for prediction interval of energy sources. DNN has the ability to increase the relevance of deep neural networks (DNN) in probabilistic forecasting due to its capacity to estimate prediction intervals accurately based on events that occur periodically. Therefore, forecasting HVAC system consumption will accurate, because the input layer is highly influenced by many events intermittent such as weather conditions, irradiance, wind and occupancy.

This research is proposed to analyze and compare both DNN and LSTM machine learning for prediction of consumption energy HVAC. In recent years, DNN has become more popular than the traditional ANN method, which is often applied to HVAC systems [24-26]. The main objective of this paper focuses on analyzing the application of DNN and LSTM machine learning for accurate prediction of HVAC energy consumption. That is possible to analyze energy conservation strategies and plans which can increase the efficiency of building consumption. In summary, in the realm of HVAC building optimization, control, and optimal control, machine learning finds extensive application across diverse phases encompassing planning, operation, and maintenance. In the next step, the results of both DNN and LSTM will be comparing by metric accuration tools. This paper utilized the Mean Squared Errot (MSE), Root Mean Squared Error (RMSE), Mean Absolute Error (MAE) and R-Squared (R^2) as a performance criterion for evaluating model results. Additionally, this research using Isolation Forest anomaly detection in data preparation step which is traditional techniques.

2. RESEARCH METHOD

This research uses the HVAC electricity consumption energy of Labtek XIX FIBRC SBM-ITB building as a case study object, which this building is used for academic activities and lectures by SBM students. In this paper, the data access of lake data of database Sielisa ITB (electricity and water system) obtains by connected to localhost Management Energy Laboratory. Figure 1 illustrates the research framework designed for predicting electrical energy consumption. This study employs Deep Neural

Network (DNN) and Long Short-Term Memory (LSTM) machine learning tools. The performance outcomes of each tool will be systematically examined and compared through accuracy metrics.

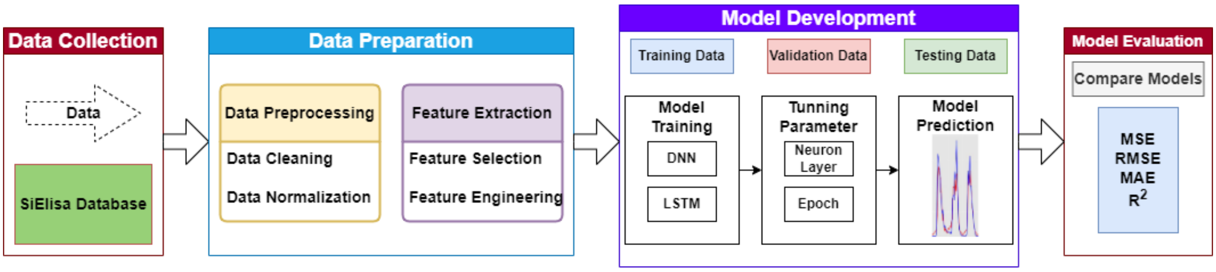

Figure 1. Framework for predicting electricity consumption in HVAC-SBM building energy

2.1. Data Collection

The first stage, Figure 1 describes how collected to the lake data within the (electricity and water system) SiElisa ITB database, which pertains to electricity and water systems, is facilitated through connection to the Management Energy Laboratory hosted on localhost. The research solely utilizes electricity consumption data sourced from the Advanced Metering Infrastructure (AMI) installed within the building. This data encompasses various electricity consumption categories such as lighting, HVAC (only AC), and other systems. The AMI system only records electricity usage in 3 phases (R, S, T) so it requires data processing in the datalake using the equation:

$$P_{AC} = (V_R I_R P_{f1}) + (V_S I_S P_{f2}) + (V_T I_T P_{f3}) \quad kW \tag{1}$$

Were P_{HVAC} represent HVAC electrical load, V (voltage) and I (Current) in each phase, divided by P_f (power factor). Further, The HVAC electricity consumption used is the entire building which is responsible for academic, office, library and administrative activities.

2.2. Data Preparation

In this paper, we used anomaly detection techniques for data cleaning. The Isolation Forest, commonly referred to as iForest, introduces a methodology involving the creation of an ensemble comprising iTrees tailored to a specific dataset. In equation (2), Anomalies are recognized as instances exhibiting notably shorter average path lengths within these iTrees. Anomalies are identified within hourly data using a sensitivity parameter setting of 1 percent, or a contamination value of 0.01, along with specified parameters including max features set at 0.3, max samples at 0.8, and n_estimators at 400. Equation (2) indicates that when we set $k = 1$, the isolation forest identifies a data point as an outlier if the function $E(t, M, k)$ for a larger range of k (greater than 1) considers it to be an outlier based on the sample dataset. Where t signifies the total number of trees, M denotes the overall number of binary splits executed during the search process, and k represents the size of the final node.

$$E(t, M, k) = \frac{1}{t} \sum_{i=1}^{t} \begin{cases} \sum_{j=1}^{M} 1 + c(0), & k = 1 \\ \sum_{j=1}^{M} 1 + c(k), & k \neq 1 \end{cases} \tag{2}$$

Additionally, holidays are predefined within the program to exclude anomalies recognized by ITB academics from the calendar system. Specifically, these holidays span from December 20th to January 16th for the semester break, April 19th to 25th for Eid holiday, and June 6th to August 20th, 2023, for the academic semester break. Following the completion of statistical analysis utilizing the isolation forest model, the subsequent steps will involve the removal of outliers and the normalization of data.

Furthermore, in this data preparation stage, we introduce novel features that impact the temporal dynamics of HVAC systems or physical variable features such as solar radiance, temperature and humidity environmental. For this paper, these features play a critical role in predicting output targets, particularly considering the geographical context of the research conducted in tropical countries. Meanwhile, time lagging techniques are employed to generate new features by incorporating data from the preceding one hour (P_{AC} $(t-1)$)and two hours (P_{AC} $(t-2)$). Table 1 illustrates the features employed in this research. While, the prediction model incorporates timeseries attributes including month, day, hour, and minute, resulting in a total of nine input features which the output target of the model is the prediction of HVAC power consumption (P_{AC}(t)).

Table 1. Features on LSTM and DNN model

Features	**Models**	
	LSTM	**DNN**
Minute	√	√
Hour	√	√
Day	√	√
Month	√	√
$irr\ (t)$	√	√
$T_{amb}\ (t)$	√	√
$H_{amb}\ (t)$	√	√
$(P_{AC}\ (t-1))$	√	√
$(P_{AC}\ (t-2))$	√	√
Target		
$(P_{AC}\ (t))$	√	√

2.3. Model Development

The subsequent stage involves developing a data-driven model for predicting HVAC electrical load, utilizing a hybrid architecture comprising LSTM and DNN layers. As we know, the LSTM neural network constitutes a type of Recurrent Neural Network (RNN). Meanwhile, DNN models has been developed in various energy applications such as prediction of HVAC energy consumption.

1) LSTM

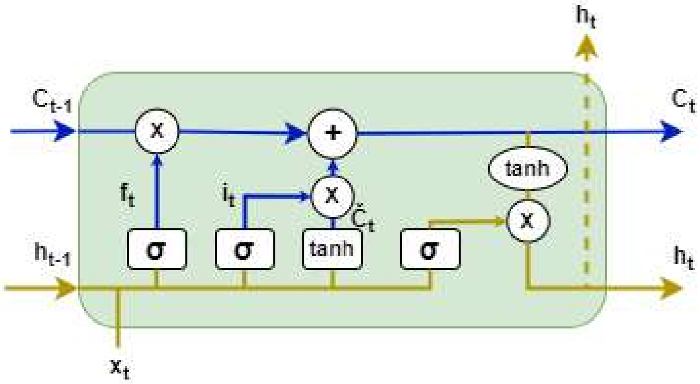

Figure 2. LSTM cell to overcome of limitation RNN

Simplify, Figure 2 show the model of LSTM which takes in previous cell state (C_{t-1}), previous cell output (h_{t-1}), and current input vector (x_t) as input parameters. It then generates the current state (C_t) and output vector (h_t) for the subsequent cell. The initial layer incorporates a forget gate, which applies a linear transformation to the current of input vector and previous states using a sigmoid function (r). This linear transformation can be written in the form (3), which gate outputs either 0 or 1, where 1 indicates to retain the state, and 0 indicates to 'discard and erase it' [27].

$$f_t = \sigma(W_f.[h_{t-1}, x_t] + b_f) \tag{3}$$

Next step in this cell, the "current state layer" operates, wherein another sigmoid function is employed. This function accepts both the previous cell output and the current input vector, conducting further linear transformations on them, which denotes in equation:

$$i_t = \sigma(W_i.[h_{t-1}, x_t] + b_i) \tag{4}$$

Volume 11, Issue 1, April 2024, pp. 77-87
ISSN 2355-5068 ; e-ISSN 2622-4852
DOI: 10.33019/jurnalecotipe.v11i1.4488

Ultimately, this layer incorporates a gate of hyperbolic tangent that reads the previous cell output and current input vector. It produces a candidate value (Č) which is subsequently added to the cell state update process by (5).

$$Č_t = tanh(W_c.[h_{t-1}, x_t] + b_t) \tag{5}$$

While, the current state undergoes an update by incorporating the previous cell state and the current candidate value, (6).

$$C_t = f_t\,.C_{t-1} + i_t\,.Č \tag{6}$$

Lastly, the current output vector, ht, is computed by applying a linear transformation through a sigmoidal function to the previous cell state and current input vector. The resulting output is then passed through a hyperbolic tangent function to normalize the values between (-1, 1), which is written in mathematically in (7) and (8).

$$o_t = \sigma(W_0[h_{t-1}, x_t] + b_0)_t \tag{7}$$

$$h_t = o_t\,.tanh(C_t) \tag{8}$$

2) DNN

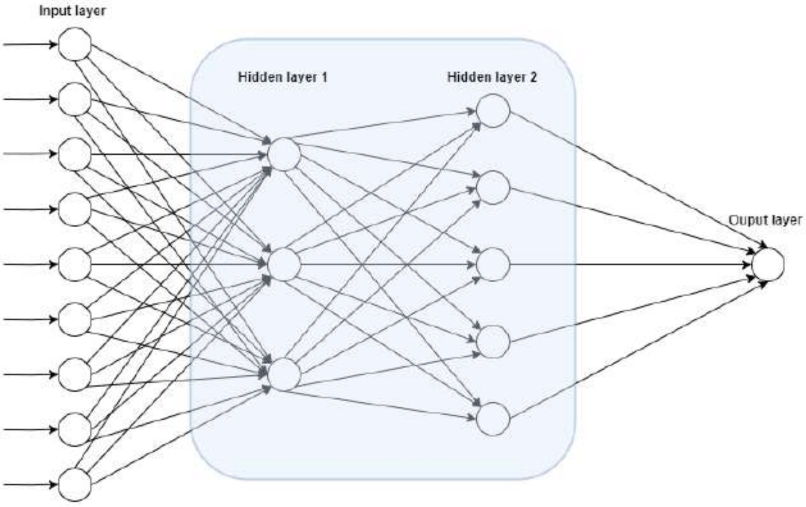

Figure 3. DNN layers and configuration

Figure 3 represents a specific architecture within artificial neural networks characterized by numerous layers comprising interconnected neurons or nodes. DNNs are termed "deep" due to their substantial layering, enabling them to effectively capture intricate patterns within data. Within the DNN framework, each layer of neurons serves to process and refine information before transmitting it to subsequent layers. In this research, the initial layer is denoted as the input layer which consists of nine input variables. Then the cover layer is the target output layer. Meanwhile, the intermediate layer is called the hidden layer which consists of 3 hidden layers 1 and 5 hidden layers 2. This study constructs a Deep Neural Network (DNN) model and evaluates the loss function during DNN training, employing the mean-squared error (MSE) metric. The MSE formula utilized in this research is as follows:

$$\mathcal{E}_{mse} = \frac{1}{d_{out}} \frac{1}{n^{\mathbb{T}}} \sum_{j=1}^{d_{out}} \left| \mathcal{N}_j^{ref}(\mathcal{L}) - \mathcal{N}_j(\mathcal{L}) \right|^2 \tag{8}$$

Where $\mathcal{N}_j^{ref}(\mathcal{L})$ denotes the corresponding reference solutions and $\mathcal{N}_j(\mathcal{L})$ $(j = 1, \ldots., d_{out})$ denotes j component of the output achieved during dimensional output d_{out} from DNN when a set of inputs $\mathcal{L}$ is given [28].

2.4. Model Evaluation

To evaluate the precision of the prediction, it is imperative to establish the metrics for evaluating the performance of the two models. This facilitates tracking the progression of estimated accuracy values over time. Four standard evaluation metrics are employed for assessment, as defined below:

- Mean Squared Error (MSE):

$$MSE = \frac{1}{n}\sum_{i=1}^{n}(x_i - y_i)^2 \tag{9}$$

- Root Mean Squared Error (RMSE):

$$RMSE = \sqrt{\frac{\sum_{i=1}^{n}(x_i - y_i)^2}{n}} \tag{10}$$

- Mean Absolute Error (MAE):

$$MAE = \frac{1}{n}\sum_{i=1}^{n}|x_i - y_i| \tag{11}$$

- R-squared (R^2):

$$R^2 = 1 - \frac{\sum_{i=1}^{n}(x_i - y_i)^2}{\sum_{i=1}^{n}(x_i - \bar{y})^2} \tag{12}$$

3. RESULTS AND DISCUSSION

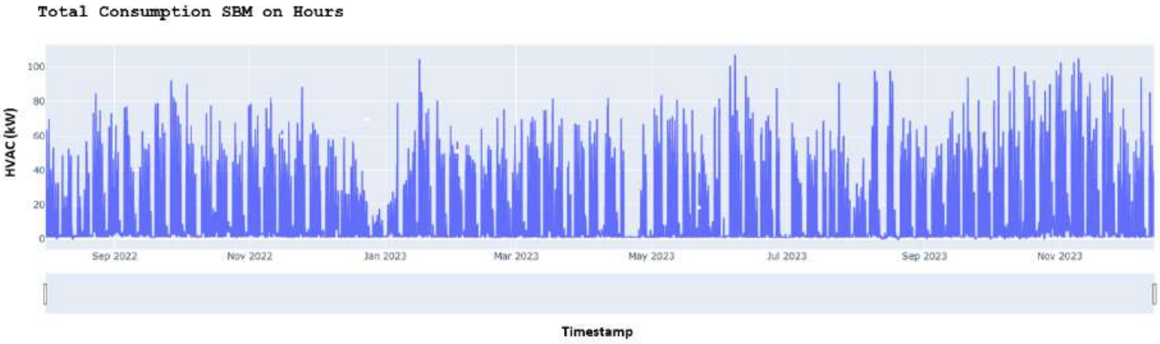

Figure 4. Dataset of HVAC electricity consumption in 2022 until 2023

Time series data is employed in this study to capture the normal building usage activities post the Covid-19 pandemic. Through rigorous outlier anomaly detection techniques, the data has been thoroughly cleaned and verified to ensure its reliability and accuracy for analysis. In this case study, this paper only focusing on the HVAC total consumption energy from September 2022 until November 2023 which represents by Figure 4. The main focus of this article is on the HVAC system, particularly on understanding and managing its electricity consumption. One significant aspect of this involves recognizing and eliminating outliers in the data by Isolation Forest anomaly detection to ensure its cleanliness and accuracy. That will help in identifying patterns and factors that influence HVAC electricity usage comprehensively.

3.1. LSTM results

The training loss of model depicted in Figure 5 reveals a significant difference in the number of epochs between LSTM and DNN, where the model shows high training loss. Despite both models employing two hidden layers, the LSTM model exhibits notably fewer epochs compared to the DNN counterpart which only used 150. Specifically, the first layer comprises 64 neurons, while the second layer consists of 32 neurons. For training purposes, the dataset is partitioned into three categories of data: 70% for training data, 20% for validation data, and 10% for testing data, following standard procedures in research papers.

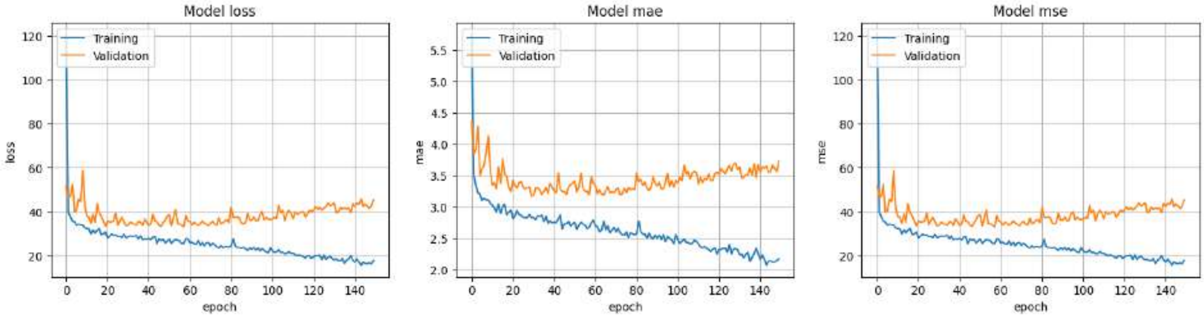

Figure 5. Training loss model of LSTM

As we know, the testing data used for the LSTM model that has been created is 10%, which is equivalent to 50 days of the total data These predictions will be validated using some of the same accuracy metrics in the DNN, while the performance results of each machine learning can be analyzed. Figure 6 presents the LSTM prediction outcomes, utilizing 1199 testing data points from the overall dataset. Additionally, the figure showcases the error percentage generated per unit time. Indirectly, the LSTM model yields a relatively high error rate over time. Nevertheless, it is imperative to note that several other accuracy metrics will be employed to ascertain the viability of this model.

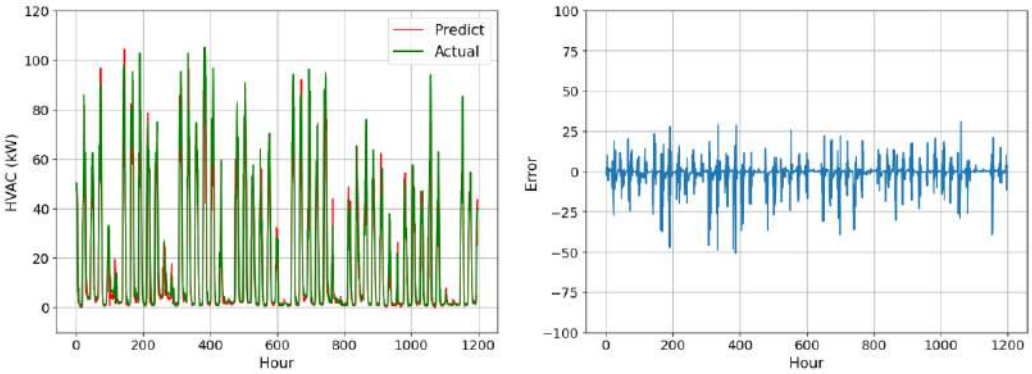

Figure 6. Prediction of HVAC electricity energy by LSTM model

3.2. DNN results

The reliability and accuracy of Deep Neural Network (DNN) models show significant consistency depending on the dataset used during the training, validation, and testing phases. With 9 sets of input variables across hidden layers 1 and 2, the DNN application aims to provide precise predictions despite the inherent volatility of the input data, characterized by variables such as solar radiation, outdoor temperature, and outdoor humidity.

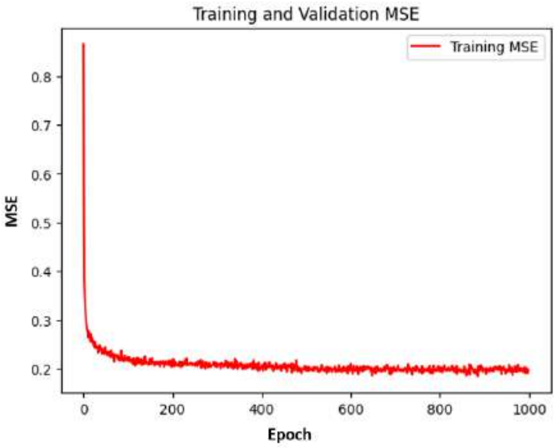

Figure 7. Training loss model of DNN

Figure 7 illustrates that the loss function or training data of DNN is lower than that of LSTM. This difference may be due to the much higher number of epochs for DNN, which is 1000 compared to model previously only 150 epochs. While, Figure 8 shows the DNN prediction outcomes utilizing 10% of the test data, equivalent to 50 days, spanning from October 23, 2023, to December 12, 2023. The results of model prediction data indicates that the training model adequately predicts the energy load of HVAC electricity consumption during weekends, especially on Saturdays and Sundays, despite the absence of holiday contextual features in the model input. Moreover, the model demonstrates reasonably accurate predictions for weekdays, even amidst numerous holidays present throughout the entire dataset.

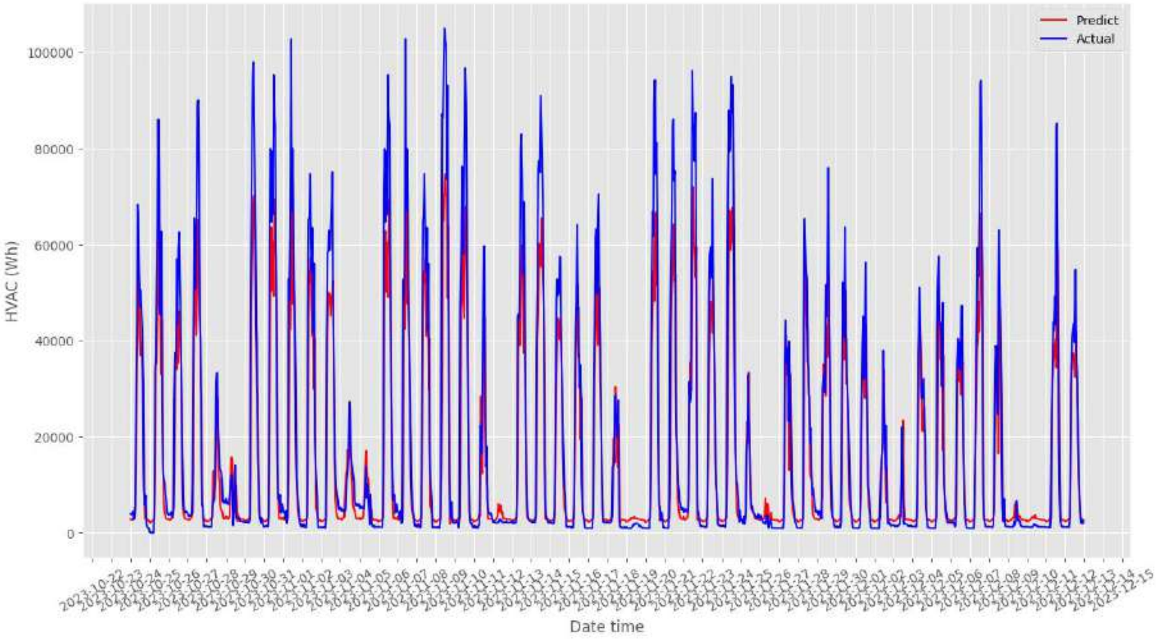

Figure 8. Prediction of HVAC electricity energy by DNN model

3.3. Metric Accuration

Table 2 provides a comprehensive overview of the errors observed in the second test for both LSTM and DNN models. The prediction efficacy of each model is evaluated through metrics such as MAE, MSE, RMSE, and R^2. This analysis allows for a thorough consideration of the various advantages and disadvantages inherent in each model, thereby facilitating the identification of the optimal model for predicting HVAC loads, particularly for university buildings.

Table 2. Metric accuration evaluation both LSTM and DNN model

Metric Accuration	Models	
	LSTM	DNN
MAE (Wh)	0.552	0.277
MSE (Wh)	25.42	0.236
RMSE (Wh)	5.042	0.486
R^2 (%)	0.941	0.782

4. CONCLUSION

The task of energy prediction is crucial in our daily lives due to its significant economic advantages and its potential to advance energy conservation efforts. While various methods have been suggested to predict energy consumption, traditional approaches often struggle because they overlook hidden periodic patterns in the data. This study aims to compare two modern techniques, Long Short-Term Memory (LSTM) and Deep Neural Network (DNN), in addressing this challenge. The methodology involves selecting nine additional factors and analyzing the time series data associated with energy consumption for modeling purposes. The key findings of this research are outlined as follows.

- The LSTM method demonstrates superior predictive performance compared to DNN, as evidenced by the high R-squared value of 0.941. This phenomenon is likely attributable to the LSTM model's larger number of cells or neurons. However, despite its higher R-squared value, other error metrics indicating accuracy display considerably larger values compared to those of the DNN method.
- Meanwhile, the DNN method outperforms in terms of error metrics used for accuracy assessment. The respective MAE, MSE, and RMSE values are 0.277, 0.236, and 0.486.

In addition, both methods are suitable for predicting fluctuating energy consumption, primarily because their R-squared values meet the standard requirements, namely R-squared greater than >0.75. Furthermore, when predicting electrical energy consumption in other machine learning techniques, particularly for systems like HVAC, where values tend to fluctuate, it is advisable to incorporate additional features such as holidays, weekdays, and weekends. This inclusion helps provide a more comprehensive understanding of the training data model.

Acknowledgments

The first authors acknowledge the financial support by LPDP Scholarship from KEMENKEU through Indonesian Education Scholarship program.

REFERENCES

[1] W. Zhang, H. Zhou, X. Bao, and H. Cui, “Outlet water temperature prediction of energy pile based on spatial-temporal feature extraction through CNN–LSTM hybrid model,” *Energy*, vol. 264, no. October 2022, p. 126190, 2023, doi: 10.1016/j.energy.2022.126190.

[2] J. Q. Wang, Y. Du, and J. Wang, “LSTM based long-term energy consumption prediction with periodicity,” *Energy*, vol. 197, 2020, doi: 10.1016/j.energy.2020.117197.

[3] Global, A. B. C. 2020 Global Status Report for Buildings and Construction. Global Alliance for Buildings and Construction. Paris, France, 2020.

[4] H. Liu, Y. Liu, X. Guo, H. Wu, H. Wang, and Y. Liu, “An energy consumption prediction method for HVAC systems using energy storage based on time series shifting and deep learning,” *Energy Build.*, vol. 298, no. August, p. 113508, 2023, doi: 10.1016/j.enbuild.2023.113508.

[5] S. L. Zhou, A. A. Shah, P. K. Leung, X. Zhu, and Q. Liao, “A comprehensive review of the applications of machine learning for HVAC,” *DeCarbon*, vol. 2, no. July, p. 100023, 2023, doi: 10.1016/j.decarb.2023.100023.

[6] K. Friansa, J. Pradipta, I. N. Haq, P. H. K. Utama, M. Wasesa, and E. Leksono, “Enhancing HVAC Electricity Load Prediction Accuracy using Bi-LSTM Method based on Daily Dataset,” *Proc. 2023 Int. Conf. Instrumentation, Control. Autom. ICA 2023*, pp. 92–96, 2023, doi: 10.1109/ICA58538.2023.10273121.

[7] A. Abida and P. Richter, “HVAC control in buildings using neural network,” *J. Build. Eng.*, vol. 65, no. July 2022, p. 105558, 2023, doi: 10.1016/j.jobe.2022.105558.

[8] M. Ala’raj, M. Radi, M. F. Abbod, M. Majdalawieh, and M. Parodi, “Data-driven based HVAC optimisation approaches: A Systematic Literature Review,” *J. Build. Eng.*, vol. 46, no. August 2021, p. 103678, 2022, doi: 10.1016/j.jobe.2021.103678

[9] D. Zhao *et al.*, “Data-driven online energy management framework for HVAC systems: An experimental study,” *Appl. Energy*, vol. 352, no. August, p. 121921, 2023, doi: 10.1016/j.apenergy.2023.121921.

[10] H. Zhong, J. Wang, H. Jia, Y. Mu, S. Lv, Vector field-based support vector regression for building energy consumption prediction, Appl. Energy 242 (2019) 403–414.

[11] A.T. Eseye, M. Lehtonen, Short-term forecasting of heat demand of buildings for efficient and optimal energy management based on integrated machine learning models, IEEE Trans. Ind. Inf. 16 (12) (2020) 7743–7755.

[12] Y. Wei, X. Zhang, Y. Shi, L. Xia, S. Pan, J. Wu, X. Zhao, A review of data-driven approaches for prediction and classification of building energy consumption, Renew. Sustain. Energy Rev. 82 (2018) 1027–1047.

[13] A. Afram, F. Janabi-Sharifi, Review of modeling methods for HVAC systems, Appl. Therm. Eng. 67 (1–2) (2014) 507–519.

[14] R. Tang, C. Fan, F. Zeng, and W. Feng, “Data-driven model predictive control for power demand management and fast demand response of commercial buildings using support vector regression,” Build. Simul., vol. 15, no. 3, pp. 317–331, 2022, doi:10.1007/s12273-021-0811-x.

[15] Z. Wang, T. Hong, M.A. Piette, Building thermal load prediction through shallow machine learning and deep learning, Appl. Energy 263 (2020), 114683.

[16] A. Das, M.K. Annaqeeb, E. Azar, V. Novakovic, M.B. Kjærgaard, Occupant-centric miscellaneous electric loads prediction in buildings using state-of-the-art deep learning methods, Appl. Energy 269 (2020), 115135.

[17] Salam, A., & El Hibaoui, A. (2021). Energy consumption prediction model with deep inception residual network inspiration and LSTM. Mathematics and Computers in Simulation, 190, 97–109. https://doi.org/10.1016/j.matcom.2021.05.006.

[18] O. Laib, M. T. Khadir, and L. Mihaylova, “Toward efficient energy systems based on natural gas consumption prediction with LSTM Recurrent Neural Networks,” *Energy*, vol. 177, pp. 530–542, 2019, doi: 10.1016/j.energy.2019.04.075.

[19] Jiang, P., Wang, Z., Li, X., Wang, X. V., Yang, B., & Zheng, J. (2023). Energy consumption prediction and optimization of industrial robots based on LSTM. Journal of Manufacturing Systems, 70(June), 137–148. https://doi.org/10.1016/j.jmsy.2023.07.009

[20] Li, Y., Tong, Z., Tong, S., & Westerdahl, D. (2022). A data-driven interval forecasting model for building energy prediction using attention-based LSTM and fuzzy information granulation. Sustainable Cities and Society, 76(October 2021), 103481. https://doi.org/10.1016/j.scs.2021.103481

[21] Li, G., Li, F., Xu, C., & Fang, X. (2022). A spatial-temporal layer-wise relevance propagation method for improving interpretability and prediction accuracy of LSTM building energy prediction. Energy and Buildings, 271, 112317. https://doi.org/10.1016/j.enbuild.2022.112317

[22] Pandey, P. R., & Dong, B. (2023). Prediction of window opening behavior and its impact on HVAC energy consumption at a residential dormitory using Deep Neural Network. Energy and Buildings, 296(May), 113355. https://doi.org/10.1016/j.enbuild.2023.113355

[23] Alcántara, A., Galván, I. M., & Aler, R. (2022). Direct estimation of prediction intervals for solar and wind regional energy forecasting with deep neural networks. Engineering Applications of Artificial Intelligence, 114(October 2021), 105128. https://doi.org/10.1016/j.engappai.2022.105128

[24] Modeling and optimizing building hvac energy systems using deep neural networks, International Conference on Smart Grid and Clean Energy Technologies (ICSGCE) (2018), https://doi.org/10.1109/ICSGCE.2018.8556684 , 2018

[25] Vision-based individual factors acquisition for thermal comfort assessment in a built environment, 15th IEEE International Conference on Automatic Face and Gesture Recognition (2020), https://doi.org/10.1109/FG47880.2020.00057 , 2020

[26] Y. Chen, Y. Shi, B. Zhang, Modeling and Optimization of Complex Building Energy Systems with Deep Neural Networks, 2017, https://doi.org/10.1109/ ACSSC.2017.8335578.

[27] Y. P. Chandra and T. Matuska, “Intelligent data systems for building energy workflow: Data pipelines, LSTM efficiency prediction and more,” *Energy Build.*, vol. 267, p. 112135, 2022, doi: 10.1016/j.enbuild.2022.112135.

[28] S. Han, H. S. Choi, J. Choi, J. H. Choi, and J. G. Kim, “A DNN-based data-driven modeling employing coarse sample data for real-time flexible multibody dynamics simulations,” *Comput. Methods Appl. Mech. Eng.*, vol. 373, p. 113480, 2021, doi: 10.1016/j.cma.2020.113480.

JURNAL ECOTIPE
Electronic, Control, Telecommunication, Information, and Power Engineering
Volume 11, Issue 1, April 2024, pp. 88-96
ISSN 2355-5068 ; e-ISSN 2622-4852
DOI: 10.33019/jurnalecotipe.v11i1.4489

Forensic Investigation of Digital Evidence on Flash Disk with Forensic Process Method Based on NIST

Febriand Gysberth Pariela Zamsari[1], Teguh Wahyono[2]
[1,2] Program Studi Teknik Informatika, Universitas Kristen Satya Wacana, Salatiga, 50715, Indonesia

ARTICLE INFO

Article history :

Received : 07/03/2024
Revised : 24/03/2024
Accepted : 15/04/2024

Keywords:

Autopsy; Digital Forensics; Flash disk; FTK Imager

ABSTRACT

Flash disk is a tool that is inseparable from daily life. With flash disks, users can keep important data for personal or company. Apart from that, in lots of cases Indonesian law uses flash disks as evidence. ITE Law (Law Information and Transactions Electronics) regulates how the provision of digital evidence becomes strong evidence in court. This research investigates forensics to digital evidence on a flash disk with four scenario tests. Processing digital forensics uses a forensic process based on guide National Institute of Standards and Technology (NIST). This research produces an analysis where the evidence processed with scenarios 1 and 4 are valid digital evidence to be submitted to the court, while evidence 2 and 3 are invalid evidence.

Corresponding Author:

Febriand Gysberth Pariela Zamsari
Informatics Engineering, Universitas Kristen Satya Wacana, Salatiga, 50715, Indonesia
Email: febriandgysberth67@gmail.com

1. INTRODUCTION

In the current era, the use of storage media like disk free or flash disks. It's not what's new and inseparable in daily life. Flash disk are often used for keeping some perceived data important to its users, for example, personal data or important information for an individual or company. However, it cannot be denied that sometimes there is an individual or group that has the intention to be active in illegal activity like data theft, distribution of malware, and so on [1].

Cybercrime develops from time to time along with the development of technology, no one can deny that sometimes digital evidence is often contained in storage media like flash disks. This issue has been proven and written down in several cases in Indonesia, via the Directory website Judgment in 2023, which can be searched with the keyword "flash disk *digital forensik*". There were 6,701 cases and in between were 138 ITE (Information and Transactions Electronics) crime cases related to flash disks [2].

Decision results prove that in case-related crimes with ITE in Indonesia, the perpetrator crime keeps evidence on a flash disk memory. A temporary law regarding ITE that applies in Indonesia is contained in law Number 19 of 2016 concerning Information and Transactions Electronics [3]. Based on the Constitution, information electronic or document electronic is legally valid evidence in a way law in Indonesia. Document electronics stores information in a way electronics that can be accessed through computer or system electronics, which includes text, sound, images, and similar shapes, which convey possible meanings understood by capable individuals.

In addition to this article, it is contained in article 6 which explains that information electronic or document electronic is considered legitimate in a way applicable in Indonesia if digital evidence can be accessed, displayed, guaranteed its integrity, and can be accountable which explains some circumstances [4]. Therefore, that's important to understand and prove the method of storage, modification, and deployment of digital evidence so you can be accountable in the eyes of the law, especially for related parties with the law. This matter is necessary for moreover deeply related validity of digital evidence, such as cases where digital evidence was initially stored in the flash disk that has been deleted can be considered valid.

National Institute of Standards and Technology (NIST) published guidelines to help analyze digital forensics for digital evidence on published storage media with code publication NIST SP 800-86. There are four stages important from NIST publication SP 800-86 in do or carry out digital forensics stages : Collection, Examination, Analysis, and Reporting [5]. With hope after four stages, they can prove that they found existing digital evidence deleted on a flash disk that can be given information structured for describing, explaining, use and place forensic information is valid evidence at court [6].

There are several studies related to digital forensics, the journal article entitled "Forensic Investigation of Remnant Data on USB Storage Devices Sold in New Zealand" focuses on the investigation forensics of residual data on the device storage flash disk. The author evaluates three tools imaging forensics sources open, namely DC3DD, DCFLDD, and Guymager, based on established criteria by the National Institute of Standards and Technology (NIST) [7]. They make case testing, analyzing functionality, and usage of hard device and consume time from every tool and compare it’s performance. This research found that most parts of flash disk purchased in New Zealand contains sensitive personal and organizational data. A journal article entitled “Static Forensics on USB Mass Storage Use Forensics Toolkit Imager” discusses the use of digital forensics on USB mass storage was experimented to obtain digital evidence of USB mass storage. Furthermore, the evidence will be processed using the Static Forensics and Forensics Toolkit Imager. Discussion results shows that the method of Static Forensics can be used in a way that is safe and valid to take digital evidence of USB mass storage [8]. Forensics Toolkit Imager is also proven to help in the extraction and processing process of digital evidence with more effectiveness and efficiency [9].

See importance validity a digital evidence, this research will do willing case investigation forensics in flash disk, to see is digital evidence in flash disk valid or not. Investigation forensics done with the use of method Forensic Process based on NIST standards. This research also involves utilization and comparison results from various analysis tools, namely the use of Autopsy and Access Data FTK imager. Application from methods that will be researched can give strong clarify and accurate results to digital evidence. The research was conducted to investigate that digital evidence based on the findings of the investigation can be a valid tool or evidence and support the trial process. For example, in the investigation there are things that support digital evidence that can incriminate the results of the verdict in the eyes of the law.

2. RESEARCH METHODS

The writer will apply a method that has been published by the National Institute of Standards and Technology (NIST) in publication NIST SP 800-86. The research’s flow can be seen in Figure 1 below.

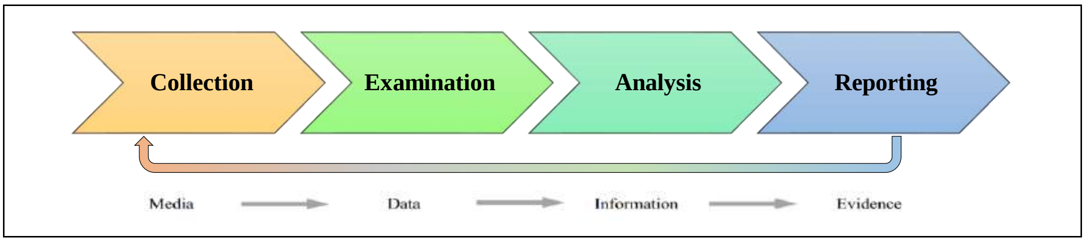

Figure 1. Forensic process

Based on Figure 1, there are 4 stages in the Forensic Process, namely Collection, Examination, Analysis, and Reporting. Following is an explanation of these stages.

2.1. Collection Stage (Data Collection)

This stage is the process of collecting related data with incidents or things you are looking for that will be identified, labeled, recorded, and collected, with guard integrity of the data [14]. So, it can be used as anevidence from flash disk and also stuff existing digital evidence inside. At this stage, the writer will create a scenario where someone provides a flash disk as evidence to be submitted to the court and the writer examines whether the flash disk is valid evidence or not in court, by creating four supporting examination scenario schemes.

First, flash disk saves 10 files considered original as digital evidence and there is no changes or deletions against 10 files. Second, the flash disk contains 10 original files however, there are 8 files on it. Third, the flash disk contains 10 original files and differences were found between files and the original file. Fourth, the flash disk with 10 original files, there is a modification name from files.

2.2. Examination Stage (Data Processing)

This stage explains tools and techniques appropriate for forensics with the type of data collected will be used for identifying and extracting information relevant from the data that has been collected and guarding the integrity of the data [15]. The tools and materials used in this research as follows:

Table 1. Tools used in research

Name Tools	Specification	Information
A laptop	ASUS TUF Gaming F15, i7-10870H 2.20GHz, 8GB, Windows 11 home single language, x64-based PC	Hardware and operating system
USB flash disk	SanDisk USB *Flash disk*, 16GB	Hardware test
Autopsy	Autopsy 4.20.0 (RELEASE)	Forensic software
AccessData FTK imager	AccessData ® FTK® Imager 4.7.1.2	Forensic software
HashCalc	Version 2.02	Hash validity software

2.3. Analysis Stage (Data Analysis)

This stages involves analysis from results inspection to get information and useful conclusions in answering questions or targets that become motivation for data collection and examination [16]. This stage is supported by analyzing the results investigation from FTK Imager and Autopsy applications, after that produced conclusion that answer the questions or targets where the conclusion is valid or not.

2.4. Reporting Stage

The final stage involves delivery results analysis, which covers explanations about actions that have been taken, determined action necessary additions done, as well as recommendation to repair the policies, guidelines, procedures, tools, and other aspects of the forensic process [17].

3. RESULTS AND DISCUSSION

3.1. Collection Stage

In the collection stage, evidence is collected in the flash disk which currently equipped with 10 pieces of digital evidence with file extensions such as, *.docx, .pdf, .mp3, .MOV, .jpg, .zip, .xlsx, .ppt, .exe and .txt* where each file own mark hashes the original will make as reference during this research.

Table 2. Reference values results hash from files original on the flash disk

File Name	MD5 Value
Document format	
[BBD]1.txt	72788458fbe6bf211a54ff730d2c1233
[BBD]2.pdf	a0323007b43cde8d6a097f06999458f1
[BBD]3.doc	25fedabace3c2022c8dacf3761f95d60
[BBD]4.pptx	ca71ae171d962d3e54880c595be9bb1e
[BBD]5.xlsx	bef9e6d9db570eafb928d7b379b49edb
Image Formats	
[BBD]6.jpg	1fe95ec5e459a88813447a4f01f89550
Audio Formats	
[BBD]7.mp3	fe01262c6e4be7e3100bb38a91853f47
Video Format	
[BBD]8.MOV	939f968f2dc99df6e69d828e7074bca6
Compression Format	
[BBD]9.zip	78cc17258dcfeacb4b306e39ad93204a
Executable Format	
[BBD]10.exe	0161434334901af384ab9453d61a13d2

3.2. Examination Stage

In this stage where the flash disk evidence is inserted into the USB port of the digital forensic evidence execution laptop, by activate the USB Write Protector followed by matching the hash value with the help of the HashCalc application and FTK imager. FTK imager is used to create data clones or data imaging as digital evidence from flash disks. Next, the results of FTK imager data imaging are matched with the results of the hash value using HashCalc and FTK imager so that the results obtained are as follows:

Table 3. Matching results imaging data with flash disk

Scheme	MD5 Flash Disk	MD5 Imaging	Status Verification
SCHEME 1	3d8a64b73ac85c6a722cd263452bf7d6	3d8a64b73ac85c6a722cd263452bf7d6	VALID
SCHEME 2	b72e142c73a46bf9f4986972bf16cc28	b72e142c73a46bf9f4986972bf16cc28	VALID
SCHEME 3	0ec8d660ad9e982c3f54793c863fe531	0ec8d660ad9e982c3f54793c863fe531	VALID
SCHEME 4	2dfc42fc0ec1dd0cbd6656659bfb25da	2dfc42fc0ec1dd0cbd6656659bfb25da	VALID

3.3. Analysis Stage

Based on results obtained after doing imaging data, such digital evidence is analyzed more and becomes digital evidence using FTK Imager and Autopsy to obtain more results maximum.

A. Scheme 1: flash disk saves 10 files considered original as a digital evidence and no change or deletion against 10 files. In scheme 1, FTK Imager and Autopsy software were successful in getting 10 files digital evidence with the hash value, after matched with the hash value reference in table 4.1 is obtained the result as follows :

Table 4. Validation results Scheme 1 uses FTK Imager and Autopsy

File Name	MD5	Original	Results Status
Document format			
[BBD]1.txt	72788458fbe6bf211a54ff730d2c1233	72788458fbe6bf211a54ff730d2c1233	VALID
[BBD]2.pdf	a0323007b43cde8d6a097f06999458f1	a0323007b43cde8d6a097f06999458f1	VALID
[BBD]3.doc	25fedabace3c2022c8dacf3761f95d60	25fedabace3c2022c8dacf3761f95d60	VALID
[BBD]4.pptx	ca71ae171d962d3e54880c595be9bb1e	ca71ae171d962d3e54880c595be9bb1e	VALID
[BBD]5.xlsx	bef9e6d9db570eafb928d7b379b49edb	bef9e6d9db570eafb928d7b379b49edb	VALID
Image formats			
[BBD]6.jpg	1fe95ec5e459a88813447a4f01f89550	1fe95ec5e459a88813447a4f01f89550	VALID
Audio formats			
[BBD]7.mp3	fe01262c6e4be7e3100bb38a91853f47	fe01262c6e4be7e3100bb38a91853f47	VALID
Video format			
[BBD]8.MOV	939f968f2dc99df6e69d828e7074bca6	939f968f2dc99df6e69d828e7074bca6	VALID
Compression format			
[BBD]9.zip	78cc17258dcfeacb4b306e39ad93204a	78cc17258dcfeacb4b306e39ad93204a	VALID
Executable format			
[BBD]10.exe	0161434334901af384ab9453d61a13d2	0161434334901af384ab9453d61a13d2	VALID

Table 4 produce 10 imaging files from the original flash disk and there is no difference value with the result hash both FTK Imager and Autopsy software, so digital evidence in scheme 1 is considered valid and can be submitted as valid digital evidence.

B. Scheme 2: the flash disk contains 10 original files, but there are only 8 files on the flash disk. In scheme 2, FTK Imager and Autopsy software were manage to get 8 original files of evidence and there were 2 original files of evidence. The evidence was erased on the flash disk along with its hash value. After being matched with the hash value reference in Table 4.1, the results were as follows:

Table 5. Validation results Scheme 2 uses FTK Imager and Autopsy

File Name	MD5	Original	Results Status
Document format			
[BBD]1.txt	72788458fbe6bf211a54ff730d2c1233	72788458fbe6bf211a54ff730d2c1233	VALID
[BBD]2.pdf	a0323007b43cde8d6a097f06999458f1	a0323007b43cde8d6a097f06999458f1	VALID
[BBD]3.doc	25fedabace3c2022c8dacf3761f95d60	25fedabace3c2022c8dacf3761f95d60	VALID
[BBD]4.pptx	ca71ae171d962d3e54880c595be9bb1e	ca71ae171d962d3e54880c595be9bb1e	VALID
[BBD]5.xlsx	bef9e6d9db570eafb928d7b379b49edb	bef9e6d9db570eafb928d7b379b49edb	VALID
Image formats			
[BBD]6.jpg	1fe95ec5e459a88813447a4f01f89550	1fe95ec5e459a88813447a4f01f89550	VALID
Audio formats			
[BBD]7.mp3	fe01262c6e4be7e3100bb38a91853f47	fe01262c6e4be7e3100bb38a91853f47	VALID
Video format			
[BBD]8.MOV	939f968f2dc99df6e69d828e7074bca6	939f968f2dc99df6e69d828e7074bca6	VALID
Compression format			
[BBD]9.zip	78cc17258dcfeacb4b306e39ad93204a	78cc17258dcfeacb4b306e39ad93204a	VALID
Executable format			
[BBD]10.exe	0161434334901af384ab9453d61a13d2	0161434334901af384ab9453d61a13d2	VALID

The results from Table 5 still same to produce 10 files equipped with a hash value of 10 files. However, both software also detects deletion of evidence files.

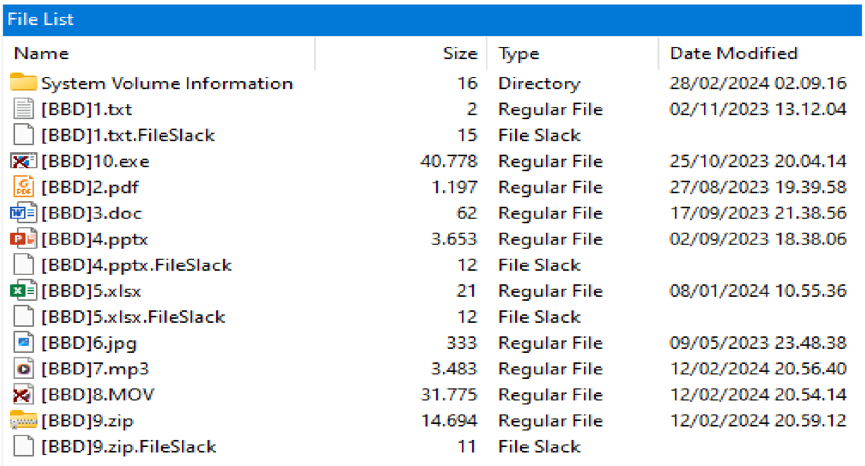
File List

Name	Size	Type	Date Modified
System Volume Information	16	Directory	28/02/2024 02.09.16
[BBD]1.txt	2	Regular File	02/11/2023 13.12.04
[BBD]1.txt.FileSlack	15	File Slack	
[BBD]10.exe	40.778	Regular File	25/10/2023 20.04.14
[BBD]2.pdf	1.197	Regular File	27/08/2023 19.39.58
[BBD]3.doc	62	Regular File	17/09/2023 21.38.56
[BBD]4.pptx	3.653	Regular File	02/09/2023 18.38.06
[BBD]4.pptx.FileSlack	12	File Slack	
[BBD]5.xlsx	21	Regular File	08/01/2024 10.55.36
[BBD]5.xlsx.FileSlack	12	File Slack	
[BBD]6.jpg	333	Regular File	09/05/2023 23.48.38
[BBD]7.mp3	3.483	Regular File	12/02/2024 20.56.40
[BBD]8.MOV	31.775	Regular File	12/02/2024 20.54.14
[BBD]9.zip	14.694	Regular File	12/02/2024 20.59.12
[BBD]9.zip.FileSlack	11	File Slack	

Figure 2. Results of imaging scheme 2 FTK Imager

The output results from Scheme 2 use FTK Imager to detect and find there are two items of deleted digital evidence with Name files [BBD]8.MOV and [BBD]10.exe. This deletion is evidenced by the icon image of existing files cross-red.

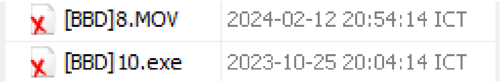

[BBD]8.MOV	2024-02-12 20:54:14 ICT
[BBD]10.exe	2023-10-25 20:04:14 ICT

Figure 3. Imaging results of Autopsy Scheme 2

The output results from Scheme 2 use Autopsy also detect and find there are two items of deleted digital evidence with Name files [BBD]8.MOV and [BBD]10.exe and verified with the file icon containing sign cross-red.

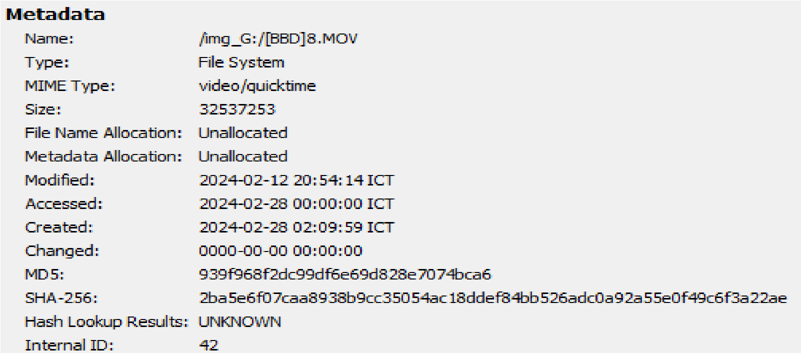

```
Metadata
  Name:                    /img_G:/[BBD]8.MOV
  Type:                    File System
  MIME Type:               video/quicktime
  Size:                    32537253
  File Name Allocation:    Unallocated
  Metadata Allocation:     Unallocated
  Modified:                2024-02-12 20:54:14 ICT
  Accessed:                2024-02-28 00:00:00 ICT
  Created:                 2024-02-28 02:09:59 ICT
  Changed:                 0000-00-00 00:00:00
  MD5:                     939f968f2dc99df6e69d828e7074bca6
  SHA-256:                 2ba5e6f07caa8938b9cc35054ac18ddef84bb526adc0a92a55e0f49c6f3a22ae
  Hash Lookup Results:     UNKNOWN
  Internal ID:             42
```

Figure 4. Item metadata digital proof [BBD]8.MOV

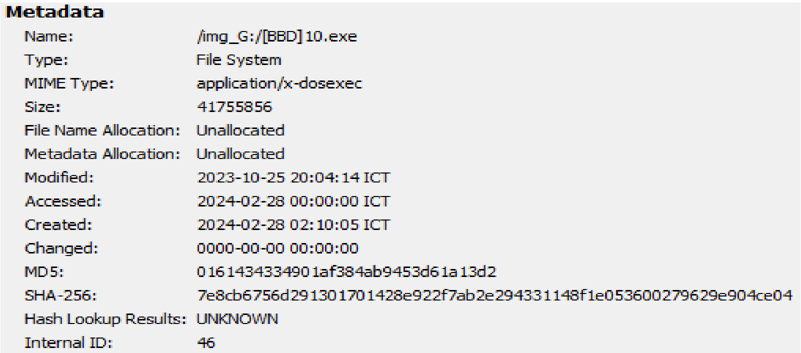

```
Metadata
  Name:                    /img_G:/[BBD]10.exe
  Type:                    File System
  MIME Type:               application/x-dosexec
  Size:                    41755856
  File Name Allocation:    Unallocated
  Metadata Allocation:     Unallocated
  Modified:                2023-10-25 20:04:14 ICT
  Accessed:                2024-02-28 00:00:00 ICT
  Created:                 2024-02-28 02:10:05 ICT
  Changed:                 0000-00-00 00:00:00
  MD5:                     0161434334901af384ab9453d61a13d2
  SHA-256:                 7e8cb6756d291301701428e922f7ab2e294331148f1e053600279629e904ce04
  Hash Lookup Results:     UNKNOWN
  Internal ID:             46
```

Figure 5. Item metadata digital proof [BBD]10.exe

This deletion is evidence with metadata from second files where allocation name files produce unallocated (no allocated) and file metadata allocation produces unallocated. Validation results scheme 2 in table 6 and table 7 as well as evidence deletion on the flash disk, in image 4 and image 5 can be concluded that evidence with scheme 2 is invalid because there are two files already deleted, files with names [BBD]8.MOV and [BBD]10.exe.

C. Scheme 3: Where the flash disk hash value 10 files original and found difference content from files with the original files. In scenario 3, both FTK Imager and Autopsy software were successful in getting 10 files digital evidence with hash value, after matched with the hash value reference in table 4.1 is obtained the result as follows :

Table 6. Validation results Scheme 3 uses FTK Imager and Autopsy

File Name	**MD5**	**Original**	**Results Status**
Document format			
[BBD]1.txt	72788458fbe6bf211a54ff730d2c1233	72788458fbe6bf211a54ff730d2c1233	VALID
[BBD]2.pdf	a0323007b43cde8d6a097f06999458f1	a0323007b43cde8d6a097f06999458f1	VALID
[BBD]3.doc	e6acb86d922ddef7f52f925ebafc8870	25fedabace3c2022c8dacf3761f95d60	**INVALID**
[BBD]4.pptx	d9a2465f75f61330d77d3e48576aea79	ca71ae171d962d3e54880c595be9bb1e	**INVALID**
[BBD]5.xlsx	bef9e6d9db570eafb928d7b379b49edB	bef9e6d9db570eafb928d7b379b49edb	VALID
Image formats			
[BBD]6.jpg	1fe95ec5e459a88813447a4f01f89550	1fe95ec5e459a88813447a4f01f89550	VALID
Audio formats			
[BBD]7.mp3	fe01262c6e4be7e3100bb38a91853f47	fe01262c6e4be7e3100bb38a91853f47	VALID
Video format			
[BBD]8.MOV	939f968f2dc99df6e69d828e7074bca6	939f968f2dc99df6e69d828e7074bca6	VALID
Compression format			
[BBD]9.zip	78cc17258dcfeacb4b306e39ad93204a	78cc17258dcfeacb4b306e39ad93204a	VALID
Executable format			
[BBD]10.exe	0161434334901af384ab9453d61a13d	0161434334901af384ab9453d61a13d2	VALID

Volume 11, Issue 1, April 2024, pp. 88-96
ISSN 2355-5068 ; e-ISSN 2622-4852
DOI: 10.33019/jurnalecotipe.v11i1.4489

Analysis results from Scheme 3 are proven with Table 6, both software can analyze and find 10 files on the flash disk but there is a change value on digital evidence with Name files [BBD]3.doc and [BBD]4.pptx.

Table 7. Artifact data from digital evidence [BBD]3.doc

Type	Value	Source
Date Modified	2024-02-28 03:54:00 ICT	org.sleuthkit.autopsy.keywordsearch.KeywordSearch IngestModule
Program Name	Microsoft Office Word	org.sleuthkit.autopsy.keywordsearch.KeywordSearch IngestModule
Last Printed Date	2021-07-03 07:35:00 ICT	org.sleuthkit.autopsy.keywordsearch.KeywordSearch IngestModule
Date Created	2023-09-15 16:37:00 ICT	org.sleuthkit.autopsy.keywordsearch.KeywordSearch IngestModule
User ID	-A- 3373 2020	org.sleuthkit.autopsy.keywordsearch.KeywordSearch IngestModule
Owner	Adhi	org.sleuthkit.autopsy.keywordsearch.KeywordSearch IngestModule
Source File Path	/img_G:/[BBD]3.doc	
Artifact ID	-9223372036854775806	

Table 7 is output from results scheme 3, where Autopsy software displays when digital evidence file [BBD]3.doc created and when the last time the file was changed and by whom. From the table can be known that file [BBD]3.doc was first created by Adhi on September 15 2023 at 16:37:00 ICT (Indochina Time) and carried out modification fill file by -A- 3373 2020 on February 28, 2024 at 03:54:00 ICT (Indochina Time).

Table 8. Artifact data from digital evidence [BBD]4.pptx

Type	Value	Source
Date Modified	2024-02-28 03:51:19 ICT	org.sleuthkit.autopsy.keywordsearch.KeywordSearch IngestModule
Program Name	Microsoft Office PowerPoint	org.sleuthkit.autopsy.keywordsearch.KeywordSearch IngestModule
Date Created	2006-08-16 00:00:00 ICT	org.sleuthkit.autopsy.keywordsearch.KeywordSearch IngestModule
User ID	-A- 3373 2020	org.sleuthkit.autopsy.keywordsearch.KeywordSearch IngestModule
Source File Path	/img_G:/[BBD]4.pptx	
Artifact ID	-9223372036854775800	

Table 8 is output from results scheme 3, where Autopsy software displays when digital evidence file [BBD]4.pptx created and when the last time the file was changed and by whom. From the table can be known that the [BBD]4.pptx file was first created on August 16, 2006 at 00:00:00 ICT (Indochina Time) and carried out modification content file by -A- 3373 2020 on February 28, 2024 at 03:51:19 ICT (Indochina Time).

The results of scheme 3, as evidenced by table 6 supplemented by table 7 and table 8, prove that there are changes in the contents of the files of digital evidence [BBD]3.doc and [BBD]4.pptx, it can be concluded that the digital evidence is invalid and cannot be used as digital evidence to support the court.

D. Scheme 4 : flash disk saves 10 considered original files as digital evidence and there is modification name or date on the digital file. In scheme 4, both FTK Imager and Autopsy software were successful in getting 10 files digital evidence with the mark the hash, after matched with hash value reference in table 4.1 is obtained the result as follows :

Table 9. Validation results Scheme 4 uses FTK Imager and Autopsy

File Name	MD5	Original	Results Status
Document format			
[BBD]1.txt	72788458fbe6bf211a54ff730d2c1233	72788458fbe6bf211a54ff730d2c1233	VALID
[BBD]2.pdf	a0323007b43cde8d6a097f06999458f1	a0323007b43cde8d6a097f06999458f1	VALID
[BBD]3.doc	25fedabace3c2022c8dacf3761f95d60	25fedabace3c2022c8dacf3761f95d60	VALID
[BBD]4.pptx	ca71ae171d962d3e54880c595be9bb1e	ca71ae171d962d3e54880c595be9bb1e	VALID
[BBD]5.xlsx	bef9e6d9db570eafb928d7b379b49edb	bef9e6d9db570eafb928d7b379b49edb	VALID
Image formats			
[BBD]6.jpg	1fe95ec5e459a88813447a4f01f89550	1fe95ec5e459a88813447a4f01f89550	VALID
Audio formats			
[BBD]7.mp3	fe01262c6e4be7e3100bb38a91853f47	fe01262c6e4be7e3100bb38a91853f47	VALID
Video format			
[BBD]8.MOV	939f968f2dc99df6e69d828e7074bca6	939f968f2dc99df6e69d828e7074bca6	VALID
Compression format			
[BBD]9.zip	78cc17258dcfeacb4b306e39ad93204a	78cc17258dcfeacb4b306e39ad93204a	VALID
Executable format			
[BBD]10.exe	0161434334901af384ab9453d61a13d2	0161434334901af384ab9453d61a13d2	VALID

The final result obtained after operating scheme 4, both FTK Imager and Autopsy software can find and analyze 10 files of digital evidence. There is no difference hash value of the 10 files tested, this signifies that scheme 4 with no change with hash value even though the file name is changed but it still can be qualified to be submitted as digital evidence.

3.4. Reporting Stage

Based on the results of the result analysis stage, it can be concluded that the digital evidence contained in the flash disk and executed according to Scheme 1 and Scheme 4 are valid. It can be seen from the display of the two processes in the software that there is no replacement or change in the hash value results. Thus, there is no defect in the authenticity of the evidence and can support material evidence to the judge in accordance with the provisions contained in ITE Law Number 19 of 2016. Meanwhile, digital evidence with scheme 2 cannot be used as digital evidence because there are deletions from the original file. Therefore, the flash disk does not qualify as digital evidence and is submitted to the court, scheme 3 also cannot be used as valid evidence due to changes in the contents of the original files [BBD] 3.doc and [BBD] 4.pptx.

The results stage report is also supported by expert lecturer, Dr. Jeferson Kameo, S.H., LLM at the Faculty of Law, Satya Wacana Christian University. He supports and agrees that the results of schemes 1 and 4 can be considered as valid evidence, because there is no change in the hash value which states that the deleted digital evidence has not been edited and qualifies as evidence according to the Electronic Information and Transaction Law (UU ITE) in Indonesia. Meanwhile, digital evidence schemes 2 and 3, cannot fulfill the elements to be submitted as digital evidence. The results of scheme validation and evidence analysis show the deletion of files and changes in the hash value of files that affect the authenticity of a file.

4. CONCLUSION

Thus, based on the test results in scheme 1 and scheme 4, it is valid evidence because there is no change in the hash value, which states that digital evidence that has been erased has not undergone editing and meets the requirements as evidence according to the ITE Law Number 19 of 2016. Meanwhile, the results of scheme 2 and 3 where digital evidence is deleted or edited from flash disk are considered invalid and do not qualify to be submitted as digital evidence. FTK Imager and Autopsy applications are capable of executing, producing, as well as finishing what to expect from the writer by the scheme that has been made. FTK Imager can analyze in a relative short time, Autopsy can do more analysis complex and deeper. With the use these two tools, the writer can finish a scheme with faster and also obtainable maximum results. Future researcher is expected to implement different scenarios and schemes as well as supported by the latest hardware and software can produce updates in different cases.

REFERENCE

[1] Barkem W, Sidabutar J. Digital Forensic Analysis of WhatsApp Business Applications on Android-Based Smartphones Using NIST. MATRIX J Management, Inform Tech and Comput Engineering 2023;22:615–26. https://doi.org/10.30812/matrik.v22i3.3033.

[2] Clerk of the Court. Directory of Decisions nd https://bangunan3.mahkamahagung.go.id/.

[3] RI UN 19 T 2016. Law of the Republic of Indonesia Number 19 of 2016 concerning Amendments to Law Number 11 of 2008 concerning Information and Electronic Transactions. Law No. 19 of 2016 2016:1–31.

[4] Sunarmi, Mahmud Mulyadi IMDKMA. Juridical Analysis of Digital Evidence in Proving Hate Speech Crime Cases in Medan District Court Decision No. 3168/Pid.Sus/2018/Pn.Mdn. Res Nullius Law J 2021;3:98–117. https://doi.org/10.34010/rnlj.v3i2.3862.

[5] Kent K, Chevalier S, Grance T, Dang H. Guide to Integrating Forensic Techniques into Incident Response. Natl Inst Stand Technol 2006.

[6] Vishnu Budi, Aan Widayat Kusban, Muhammad SM. Computer Forensic Analysis to Support the Investigation Process in Crime Cases 2015:12.

[7] Shah Z, Kyaw A, Truong HP, Ullah I, Levula A. Forensic Investigation of Remnant Data on USB Storage Devices Sold in New Zealand. Appl Sci 2022;12. https://doi.org/10.3390/app12125928.

[8] Mahardika Sulaksono P, Santoso B. Static Forensics on USB Mass Storage Using Forensics Toolkit Imager. J Comput Ther 2022;8:132–42. https://doi.org/10.35143/jkt.v8i1.5334.

[9] Muhammad Nur Al-Azhar. Series 1 Digital Forensics: General Guide to Digital Forensics on Windows, Linux, Mac & Mobile Platforms. Salemba Infotek Publisher; 2021.

[10] Hassan NA. Digital Forensics Basics. Digit Forensics Basics 2019. https://doi.org/10.1007/978-1-4842-3838-7.

[11] Hassan NA. Introduction: Understanding Digital Forensics. Digit Forensics Basics 2019:1–33. https://doi.org/10.1007/978-1-4842-3838-7_1.

[12] Mega Rosita. Comparative Analysis of the Performance of FTK IMAGER and AUTOPSY in Digital Forensics on *Flash disks* . Crypto Info 2023;17. https://doi.org/10.56706/ik.v17i3.83.

[13] Jr MP, Arnaldy D, TP S, Si M. Digital Document Integrity Analysis in the Digisign UTD PNJ Application Using Digital Signatures. RepositoryPnjAcId nd

[14] Yuliana D, Yuniati T, Zen BP. Analysis of Digital Evidence of Cyberbullying on Social Media Using the National Institute of Standards and Technology (Nist) 800-101 Method. LEDGER J Inform Inf Technol 2022;1:113–23. https://doi.org/10.20895/ledger.v1i3.812.

[15] Abdillah MF, Prayudi Y. Data Recovery Comparative Analysis using Open-based Forensic Tools Source on Linux. Int J Adv Comput Sci Appl 2022;13:633–9. https://doi.org/10.14569/IJACSA.2022.0130975.

[16] Aditya Gunawan CT, Suryanto Y. Maturity Level Analysis of Digital Evidence Handling on Integrated Criminal Justice System based on NIST SP800-53 Revision 5 Using NIST Maturity. Budapest Int Res Critics Inst 2022:10481–97. https://doi.org/10.33258/birci.v5i2.4861.

[17] Aushaf RF, Ismail SJI, ... Implementation of Digital Forensics in Telegram on the Operating System. eProceedings … 2021;7:2767–78.

JURNAL ECOTIPE
Electronic, Control, Telecommunication, Information, and Power Engineering
Volume 11, Issue 1, April 2024, pp. 97-106
ISSN 2355-5068 ; e-ISSN 2622-4852
DOI: 10.33019/jurnalecotipe.v11i1.4494

Monitoring System for Electrical Energy Use and Charging Electricity Tokens Based on Website and Whatsapp Application

Novri Amsyah[1], Asmar[2], Rudy Kurniawan[3]
[1,2,3] Electrical Engineering Department, Bangka Belitung University, Indonesia

ARTICLE INFO

Article history :

Received : 01/04/2024
Revised : 10/04/2024
Accepted : 15/04/2024

Keywords:

Electrical Energy; ESP32 microcontroller; Electricity Token Website; Whatsapp

ABSTRACT

The large number of equipment or electrical loads used causes large amounts of electrical energy usage. To determine the amount of electrical energy used, you can install an electrical energy meter whose results can be monitored via an LCD display. In this research, a website-based application was designed that can monitor electrical energy usage, by providing information in the form of voltage, current, power, and active power usage over time. Apart from that, this website can also top up electricity tokens as a feature to limit the use of electrical energy that will be used by users and is equipped with a notification message for remaining electricity tokens to the Whatsapp application. This system was developed using an ESP32 microcontroller which will provide data, process data, and present data from instrument measurements, then send the measurement results data every 15 seconds to the monitoring website. From the test results, the tool can measure electrical quantities such as current and voltage. The tool can also send measurement results to the website and store measurement data in a database. Test results for sending notification messages, the message was successfully sent to WhatsApp media if the electricity token met the specified conditions.

Corresponding Author:

Asmar
Electrical Engineering Dept., Bangka Belitung University, Indonesia
Email: asmarubb2@gmail.com

1. INTRODUCTION

The use of electrical energy is very large in today's modern life. The large amount of electrical energy used is caused by the large number of equipment or electrical loads used. There are three types of loads in an electrical system, namely: resistive, inductive, and capacitive. The electrical loads commonly used are resistive and inductive loads, where the inductive load absorbs reactive power while the resistive load absorbs active power.

Saving electrical energy can be done in various ways, such as turning off electricity when not in use and using energy-saving items. Apart from that, there are also ways to maximize electricity savings, namely by directly monitoring the use of electrical energy.

To determine the amount of electrical energy used, especially for one phase, you can do this by installing an electrical energy meter and then displaying it via an LCD display. This means that to monitor the electrical energy used you must directly look at the location where the measuring instrument is installed. By utilizing current technological advances, monitoring can actually be carried out remotely, one of which can be using a website-based application that can be accessed anytime and anywhere.

From the description above, a system is needed that is able to monitor electrical energy use in real time on a website basis so that it can be monitored anywhere and at any time. This website application is also designed to be able to control relays to turn on or turn off the electricity source and can regulate the amount of electrical energy used or electrical tokens on the prototype device created, so as to limit the use of electrical energy that will be used by the user. To be able to realize this monitoring system, it is necessary to create a prototype tool that can measure voltage, current and electrical power.

It is hoped that the creation of this website-based monitoring application will make it easier for electrical energy users to find out how much electrical energy they use by displaying it in graphical form and equipped with historical data reporting on the use of electrical energy that has been used. This website application can also control the use of electrical energy by setting electricity tokens or limits on the amount of electrical energy to be used.

2. RESEARCH METHODS

The research begins with preparing the tools and materials that will be used, then continues with designing the tools and designing the website. The tool is used to measure current, voltage and electrical power which is made using a current sensor, voltage sensor and zero crossing detector circuit and programmed using an ESP32 microcontroller. After the tool has been successfully created, the next step is to design the website interface that will be used to display information related to electrical energy usage data.

The flow diagram of this research can be seen in Figure 1.

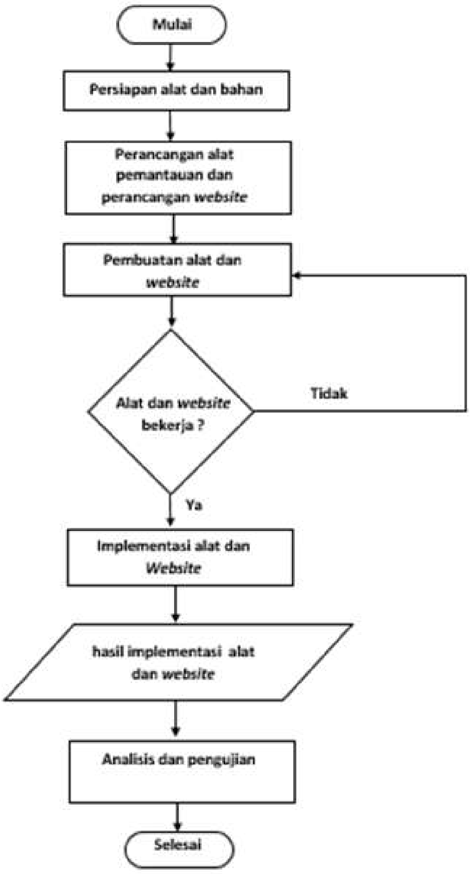

Figure 1. Research flow diagram

2.1. System Functional Blocks

The load current is measured using a current sensor and the load voltage is measured using a voltage sensor (voltage divider). After the current and voltage at the load are obtained, the current and voltage data are entered into the zero crossing detector circuit. The Zero crossing detector circuit is useful for detecting or obtaining the difference in voltage and current pulse waves. ESP32 is a microcontroller to process the output from the zero crossing detector circuit to calculate the power factor value. The output from the current and voltage sensors is also connected directly to the ESP32 analog pin to obtain the voltage and current values for the load. So you can calculate electrical power.

In carrying out power factor improvements, the ESP32 microcontroller will regulate the work of the relay according to the conditions specified in the program, the relay will work when the power factor in the system is low. A relay that is in HIGH (working) condition will connect the capacitor to the load as a reactive power compensator, so that the reactive power requirements of the load can be met as a result of which the previously low power factor can be improved.

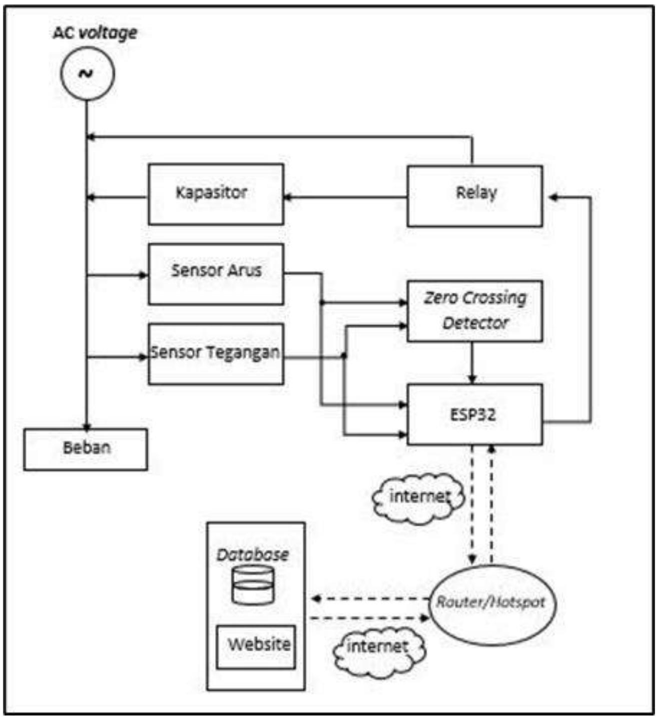

Figure 2. System functional diagram

Data on power factor values and measured electrical energy usage are then sent to the website for display. This data is sent via the internet network using the TCP/IP protocol. The ESP32 microcontroller equipped with a WiFi module makes it possible to carry out this communication. ESP32 will request a connection to the router/modem. If the request is successful, ESP32 will get an IP address. By getting this IP address, TCP/IP data communications can be carried out between ESP32 and the website. Data that is successfully sent from the ESP32 will then be saved into the MySQL database.

2.2. ESP32 Communication Architecture with Websites

In this research, the ESP32 will send measurement data such as voltage, current, power factor, active power, reactive power and apparent power values. Data is sent using the TCP/IP protocol every 15 seconds to the web server, then the web server will forward it to the backend of the website to display it to the user and store the data in the database.

The electricity token entered via the website will be saved into the database, then Laravel as the backend of the website will return the electricity token database in JSON format, so that the value of the electricity token data stored in the database can be retrieved by ESP32 via the HTTP GET protocol. Notification of the remaining electricity tokens that have been used will be sent to WhatsApp using the WhatsApp bot API. The data communication process between the ESP32 and the WhatsApp bot API is carried out using the HTTP POST protocol.

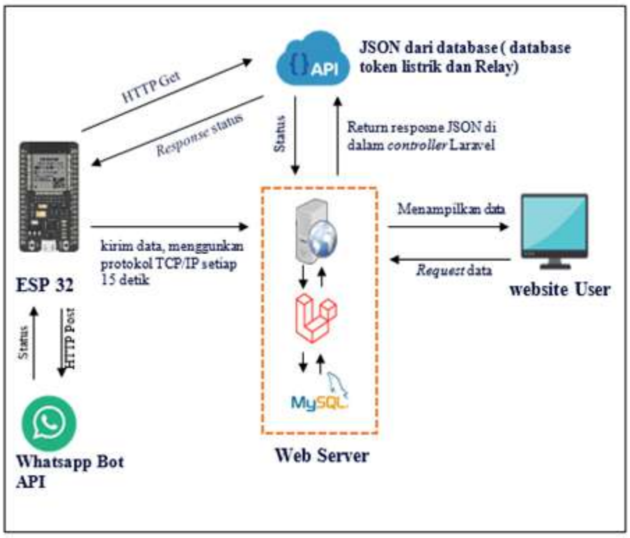

Figure 3. Data communication architecture

2.3. Designing Use Case Diagrams

A use case diagram is a description or representation of the interactions that occur between the system and its environment. A use case describes an interaction between one or more actors and the system to be created. In simple terms, use case diagrams are used to understand what functions are in a system and who can use these functions. The following is a use case diagram for a website monitoring electrical energy usage, which can be seen in Figure 4.

Seen in Figure 4, there are two actors on this monitoring website, namely super admin and admin. Both have the same task except the admin cannot add new data for users.

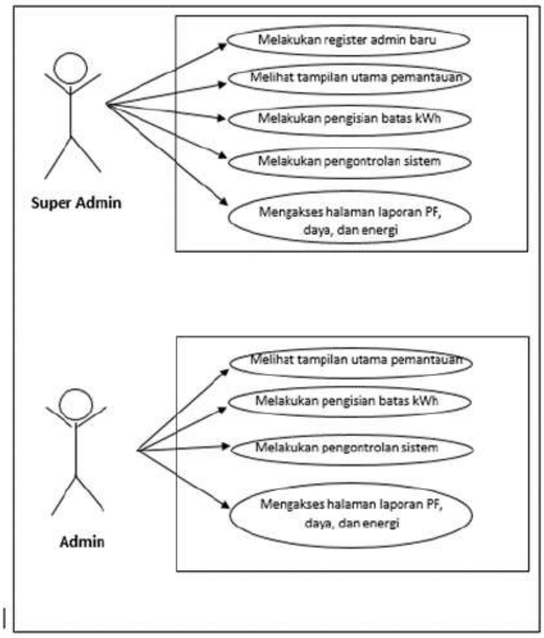

Figure 4. Website use case diagram

2.4. Test Method

The testing method in this research was carried out by testing notification messages, knowing that the system was successful in sending notification messages to WhatsApp in the form of text messages. A notification message will be sent when the regulated electricity token value limit is less than 5 kWh and less than 0 kWh. When it is less than 5 kWh the system will send the message "Refill Credit Immediately", whereas when the electricity token is less than 0 kWh the system will send the message

"Electricity is Turned Off", and immediately turn off the relay on the device to disconnect the electricity source to the load.

3. RESULTS AND DISCUSSION

3.1. Results of Tool Design

Tools are made based on designs that have been carried out and can function as desired. This tool can measure electrical quantities such as current and voltage and improve power factor. The tool can send measurement results to the website and store measurement data in a database. The relay as a switch to turn the electricity source on or off can be controlled via the control panel on the website. The tool created can also run an electricity token feature to limit the use of electrical energy which is controlled via the website. The designed tool also has the advantage of storing calculation data on electrical energy usage, so that in the event of a power outage the value of the last electrical energy used is still stored. Figure 5 below is a display of the tool that has been created.

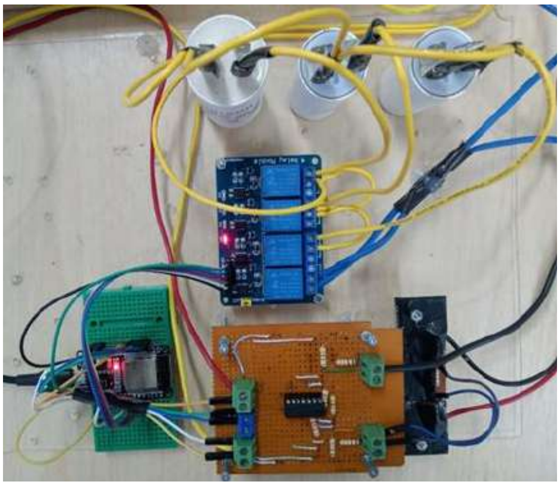

Figure 5. Instrument results

3.2. Results of Website Design

The interface of the software is created based on the design that has been carried out. Website applications can be run in a web browser. The interface results are displayed from a screenshot of the monitoring website page.

Figure 6. The results of the main page design

Figure 6 above is the result of the main monitoring page containing information starting from voltage values, current values, energy usage data graphs, power factor data graphs before and after repairs as well as power value graphs (active power, reactive power and apparent power). The data is displayed in real time with data updates every 15 seconds. This page also displays the remaining kWh

Volume 11, Issue 1, April 2024, pp. 97-106
ISSN 2355-5068 ; e-ISSN 2622-4852
DOI: 10.33019/jurnalecotipe.v11i1.4494

value as a feature for limiting energy use, the value of which is input by the user in the data management page menu.

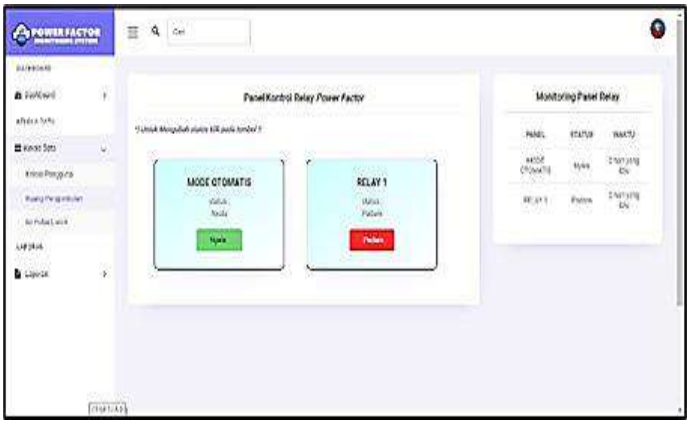

Figure 7. Results of control page design

Figure 7 above is a control menu page containing two system control panels, namely a panel for selecting automatic mode or manual mode for the system and a panel that is used to control relays. In automatic mode, the relay as a switch to disconnect the electricity source works based on the electricity token limit conditions given in the kWh limit content menu as in Figure 8 below. The relay will be in LOW condition (turning off the electricity source) when the remaining kWh pulse is less than 0 kWh. Meanwhile, in manual mode or when automatic mode is turned off, the relay can be controlled directly to turn the electricity source on or off according to needs without being influenced by the controlled kWh limit value. When relay 1 is in the "on" status, it will change the condition of the relay on the device to be on, indicated by the relay light being on, while when relay 1 is in the "off" status, it will change the condition of the relay on the device to be off, marked by the relay light being off.

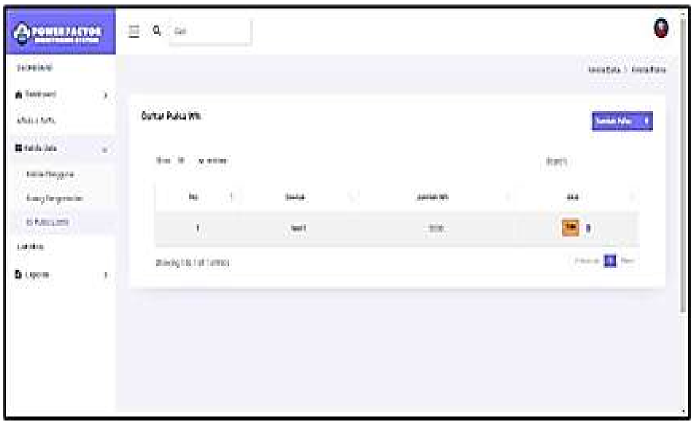

Figure 8. Results of the design of the electricity token charging page

Figure 8 above is the electricity token filling page. This page displays the history of previous kWh usage limit charging data or electricity tokens and there are action buttons to add, change and delete kWh limit data values. The kWh limit value or electricity token is input using Watt-hour (Wh), if you want to enter 5 kWh into the system you must input 5000 Wh. The value of electricity tokens that have been successfully input will be reduced by the amount of energy consumption used by the user and displayed on the main page.

Volume 11, Issue 1, April 2024, pp. 97-106
ISSN 2355-5068 ; e-ISSN 2622-4852
DOI: 10.33019/jurnalecotipe.v11i1.4494

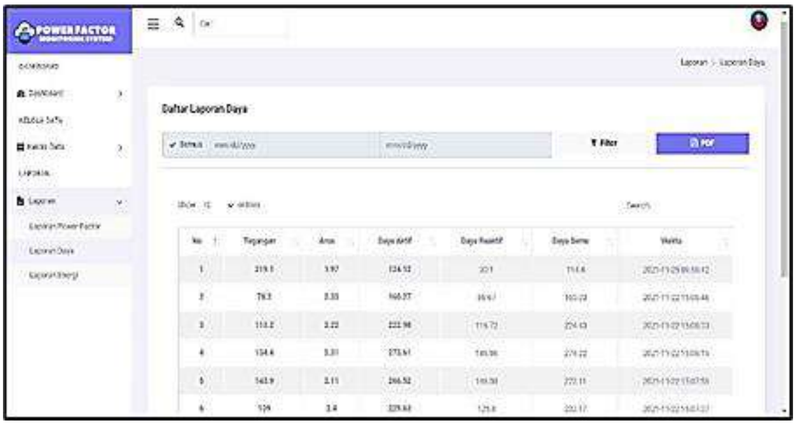

Figure 9. Results of the design of the power, voltage, and electric current report page

Figure 9. This is a report menu containing recap report information including voltage values, current values, active power values, reactive power and apparent power stored in the database. This menu also has a time filter feature to filter data based on a certain date and there is also a feature for downloading report recaps in PDF document form.

Table 1. Ten power data downloaded from websites based on time filters

NO	Tegangan (V)	Arus (A)	Daya Aktif (W)	Daya Reaktif (VAR)	Daya Semu (VA)	Waktu
1	213.75	1.31	243.27	138.46	243.65	2021-12-31 09:53:57
2	214.88	1.3	238.55	145.26	238.64	2021-12-31 09:54:13
3	217.25	1.3	243.17	145.57	243.25	2021-12-31 09:54:29
4	214	1.32	240.74	148.25	240.77	2021-12-31 09:54:45
5	215.62	1.29	240.86	137.68	241.28	2021-12-31 09:55:02
6	215.75	1.29	241.25	137.01	241.72	2021-12-31 09:55:17
7	213.62	1.29	233.74	144.15	233.87	2021-12-31 09:55:34
8	216	1.29	240.82	139.17	241.16	2021-12-31 09:55:49
9	214.75	1.29	235.91	143.55	236.06	2021-12-31 09:56:05
10	216	1.29	235.54	147.72	235.58	2021-12-31 09:56:21

In Table 1 are measurements of power, voltage and electric current values downloaded from the website application based on time filters.

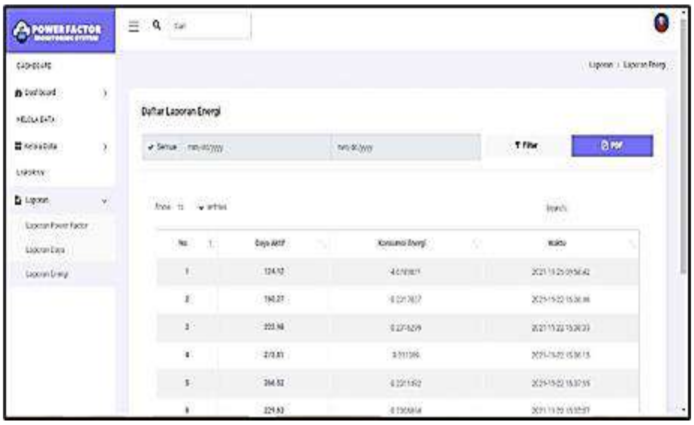

Figure 10. Results of energy report menu page design

The energy report menu contains summary report information on user energy consumption stored in the database. This menu also has a time filter feature to filter data based on a certain date and there is also a feature for downloading report recaps in PDF document form.

Table 2. Ten electrical energy data downloaded from websites based on time filters

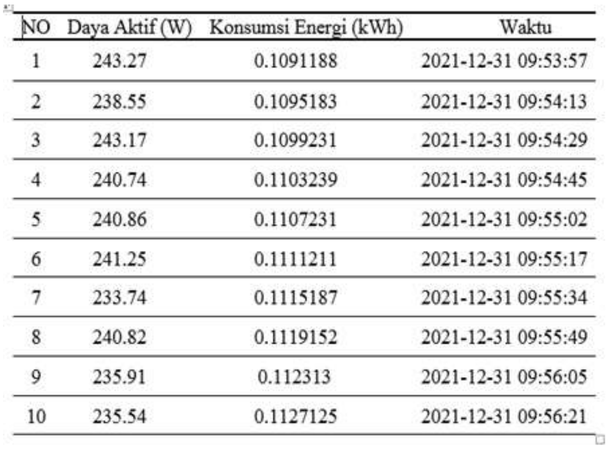

NO	Daya Aktif (W)	Konsumsi Energi (kWh)	Waktu
1	243.27	0.1091188	2021-12-31 09:53:57
2	238.55	0.1095183	2021-12-31 09:54:13
3	243.17	0.1099231	2021-12-31 09:54:29
4	240.74	0.1103239	2021-12-31 09:54:45
5	240.86	0.1107231	2021-12-31 09:55:02
6	241.25	0.1111211	2021-12-31 09:55:17
7	233.74	0.1115187	2021-12-31 09:55:34
8	240.82	0.1119152	2021-12-31 09:55:49
9	235.91	0.112313	2021-12-31 09:56:05
10	235.54	0.1127125	2021-12-31 09:56:21

In Table 2 are measurements of power, voltage and electric current values downloaded from the website application based on time filters.

3.3. Testing Notification Messaging

This monitoring system will send a notification if the remaining kWh limit value meets the specified conditions. The system will send a notification message with two conditions, namely first if the kWh limit used is less than 5 kWh and second if the kWh limit used is less than 0 kWh. Sending notifications via WhatsApp messaging media. The following is an example of sending a notification shown in Figure 11.

This+is+a+test&apikey=466618 18.22

Pesan Pertama Coba Berhasil 18.48

Pesan Pertama Coba Berhasil 19.54

18 November 2021

Segera Isi Ulang Pulsa 12.14

Listrik Dimatikan 12.14

Segera Isi Ulang Pulsa 14.56

Segera Isi Ulang Pulsa 14.58

22 November 2021

Segera Isi Ulang Pulsa 11.11

Listrik Dimatikan 11.12

Segera Isi Ulang Pulsa 11.13

Listrik Dimatikan 11.13

Segera Isi Ulang Pulsa 11.15

Listrik Dimatikan 11.16

Segera Isi Ulang Pulsa 14.24

Listrik Dimatikan 14.26

Figure 11. Display of notifications via WhatsApp messages

It can be seen in Figure 11 that the system has successfully sent notifications via WhatsApp messages. Notifications containing the message "Refill Credit Immediately" occur when the remaining kWh limit used is less than 5 kWh, while notifications containing the message "Electricity is Turned Off" occur when the remaining kWh limit used is less than 0 kWh. In this case, the success of sending notifications is 100% after testing.

4. CONCLUSION

The website-based application created can monitor and provide information on the power factor value before and after repairs, as well as the use of electrical energy. Monitoring can be done via a web browser, with a data update interval of 15 seconds. The application can be used to control relays to turn power sources on or off online and remotely. The application can also set electricity tokens or the amount of electrical energy (kWh) that can be used by users and send notification messages when minimum conditions are reached. The test results for sending notifications show that data will be sent to WhatsApp media if the specified conditions are met and notification delivery success is 100%.

REFERENCE

[1] Pian, P., I. Sulistiyowati, and A. Wisaksono. "Perancangan Alat Perbaikan Faktor Listrik Rumah Tangga Dengan Monitoring Telegram." *JEECOM Journal of Electrical Engineering and Computer* 5.1 (2023): 71-77. Aminudin. 2015. *Cara Efektif Belajar Framework LARAVEL*. CV. Lokomedia. Yogyakarta.

[2] Angga P. J., I. W. Arta Wijaya, dan C. G. Indra Partha. "Rancang Bangun Kapasitor Bank Otomatis Berbasis Mikrokontroler ATmega 328P Untuk Perbaikan Faktor Daya." *Jurnal SPEKTRUM* 5.1 (2018): 157-163.

[3] Ahmad Faisal F., Asep Suhendi, and Indra Wahyudin Fathonah. "Rancang Bangun Website Untuk Monitoring Penggunaan Daya Listrik Tiga Fasa Berbasis Power Meter Di Gedung Deli Universitas Telkom." *eProceedings of Engineering* 8.2 (2021). Handarly, Jefri Lianda. 2018. *Sistem Monitoring Daya Listrik Berbasis IoT (Internet of Things)*. Journal of Electrical Electronic Control and Automotive Engineering. Vol.3, No.2, November 2018.

[4] Fatoni Nur H., Sabar Setiawidayat, dan Moh Mukhsim. "Alat Monitoring Pemakaian Energi Listrik Berbasis Android Menggunakan Modul PZEM-004T." *Prosiding Seminar Nasional Teknologi Elektro Terapan*. Vol. 1. No. 01. 2017.

[5] Muhammad Irfan, Seno Darmawan Panjaitan, and Muhammad Saleh. "Sistem kendali dan monitoring faktor daya listrik berbasis mikrokontroler dan internet of things (IoT)." *Jurnal Teknik Elektro Universitas Tanjungpura* 1.1 (2014).

[6] Zakky Ramadhan, Sabriansyah Rizqika Akbar, and Gembong Edhi Setyawan. "Implementasi Sistem Monitoring Daya Listrik Berbasis Web dan Protokol Komunikasi Websocket." *Jurnal Pengembangan Teknologi Informasi dan Ilmu Komputer* 3.1 (2019): 205-211. Sari, J.I. 2020. *Rancang Bangun Sistem Informasi Monitoring dan Perhitungan Laporan Susut Transaksi Energi Berbasis Web Pada PT. PLN (Persero) Area Makassar Utara.* Skripsi. Jurusan Sistem Informasi Fakultas Sains danTeknologi UIN Alauddin Makassar.

[7] Julia Indah Sari, "Rancang Bangun Sistem Informasi Monitoring Dan Perhitungan Laporan Susut Transaksi Energi Berbasis Web Pada PT PLN (Persero) Area Makassar Utara.[Skripsi]." *Makassar: UIN Alauddin Makassar* (2018).

[8] Dani Sasmoko, Yanuar Arief Wicaksono. "Implementasi Penerapan Internet Of Things (Iot) Pada Monitoring Infus Menggunakan Esp 8266 dan Web Untuk Berbagi Data." *Jurnal Ilmiah Informatika* 2.1 (2017): 90-98.

[9] Venia Sifa Erlinda. Pengembangan Desain Sistem Monitoring Dan Pengisian Token Listrik Pada Two-Way Energy Meter Berbasis Iot (Internet Of Things). Diss. Universitas Pendidikan Indonesia, 2018.

[10] Hartono Budi Santoso, Sapto Prajogo, and Sri Paryanto Mursid. "Pengembangan Sistem Pemantauan Konsumsi Energi Rumah Tangga Berbasis Internet of Things (IoT)." *ELKOMIKA: Jurnal Teknik Energi Elektrik, Teknik Telekomunikasi, & Teknik Elektronika* 6.3 (2018): 357.

Volume 11, Issue 1, April 2024

ISSN 2355-5068
e-ISSN 2622-4852

Publisher Address :

Electrical Engineering Department
Faculty of Science and Engineering - Bangka Belitung University
Balunijuk, Kab. Bangka, Prov. Kep. Bangka Belitung
University Phone : (0717) 422145, 422965 Fax. (0717) 421303
Faculty Phone : (0717) 4260033 ext. 2122, 2124
Website : https://ecotipe.ubb.ac.id/index.php/ecotipe
E-mail : jurnalecotipe@ubb.ac.id / jurnal.ecotipe@yahoo.com